論文 / 著書情報
Article / Book Information

題目(和文)	
Title(English)	Numerical Study of Cavitation Bubble Collapse Impact Loading and Plastic Deformation Behavior in Metals and Polymers
著者(和文)	RubaniFirly
Author(English)	Firly Rubani
出典(和文)	学位:博士(工学), 学位授与機関:東京工業大学, 報告番号:甲第12522号, 授与年月日:2023年9月22日, 学位の種別:課程博士, 審査員:因幡 和晃,井上 裕嗣,伏信 一慶,阪口 基己,青野 祐子
Citation(English)	Degree:Doctor (Engineering), Conferring organization: Tokyo Institute of Technology, Report number:甲第12522号, Conferred date:2023/9/22, Degree Type:Course doctor, Examiner:,,,,
学位種別(和文)	博士論文
Type(English)	Doctoral Thesis

Doctoral Degree Dissertation

Numerical Study of Cavitation Bubble Collapse Impact Loading and Plastic Deformation Behavior in Metals and Polymers

Rubani Firly

Advisor: Associate Professor Kazuaki Inaba

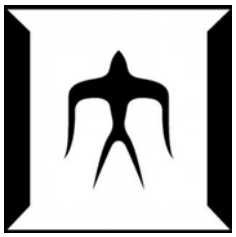

Tokyo Instititute of Technology
School of Engineering
Department of Mechanical Engineering

March 2023

Abstract

The prediction of cavitation damage is essential because it opens the opportunity to develop a phenomenological model that can be useful to improve the design process of hydraulic machinery components. Metals and polymers are the materials most frequently used in hydromachinery components that are prone to cavitation damage. This study examined the damage mechanism of metals (titanium, SUS304, Al2024, and magnesium) and polymers (nylon, Teflon, Adiprene, epoxy, and polyethylene) due to cavitation bubble collapse by utilizing a coupled fluid-solid hydrocodes solver. An air bubble was positioned adjacent to solid material within a long and narrow water-filled channel. A planar shockwave was utilized to create instability within the air bubble, causing a nonspherical collapse that is often observed in cavitation bubbles. Measured BCILs from solid material cases show good agreement with the cavitation erosion test result of A1050, SS400, Epoxy resin, PP, and HDPE. Wave propagation analysis representing BCIL on solid surface revealed that cavitation damage on metals can be defined by BCIL and acoustic impedance. On the other hand, the BCIL on polymers generates an excessive plastic deformation, so called cavitation pit. An image analysis on cavitation pit growth demonstrated a strong correlation between the pit's volume and depth with the polymer's yield strength.

Acknowledgement

First and foremost, I would wish to express my sincere gratitude to my supervisor, Prof. Kazuaki Inaba for his guidance, suggestions, and support throughout my Doctoral research. I also wish to extend my gratitude to Prof. Kikuo Kishimoto, Prof. Farid Triawan, and Dr. Hiroaki Nakamoto for their helpful advice and support. Without their guidance, I will be unable to finish this dissertation.

I also would wish to express my gratitude for the service of my dissertation committee members, Prof. Hirotsugu Inoue, Prof. Motoki Sakaguchi, Prof. Kazuyoshi Fushinobu, and Prof. Yuko Aono. I also would like to thank all of my laboratory members of Koubutsu Lab for their support, friendship and help. Also for Ms. Nobue Tsuchiya, the secretary of our lab, for her assistance throughout my Doctoral research.

I am also grateful for the strong community of Indonesian students in Tokyo Tech (PPI Tokodai), especially the Angklung team, for providing the emotional support and adventures of exploring Japan to enjoy my time here as a student. I also feel deeply grateful to my parents for their prayers, encouragement, and support throughout my life. I also would wish to say thanks for my siblings and nephews for their emotional support.

Finally, I want to say *alhamdulillah waa syukurillah* to Allah *Subhaanahuwata'ala* for everything that He has given me throughout this life. Without His guidance through The Holy Qur'an, I would not be able to find meaning and purpose of this journey called life.

Contents

List of Figures

List of Tables

Nomenclature

$\bar{\delta_d}$	pit depth
$\bar{\delta_r}$	pit radius
$\bar{w}$	channel's width
$\Delta\sigma$	Stress range
ϵ_u	Ultimate elongation
ϵ_y	Elongation at yield
Γ	Mie-Gruneisen coefficient
γ	stand-off distance
γ_{EOS}	polytropic constant
ρ_L	water density
ΣE_n	Impact energy ($\mathrm{J\,m^{-2}}$)
ΣF_i^2	Cumulative Impact Energy ($\mathrm{J\,m^{-2}}$).
σ_{11}	Principal stress
σ_a	Stress amplitude
σ_m	Mean stress
σ_u	Ultimate strength
σ_y	Yield strength.
σ_y	Yield strength
$\dot{V}$	pit volume growth rate
$\mathbf{V}$	pit volume

C_L linear artificial viscosity

c_L sound speed of water ($1483\,\mathrm{m\,s^{-1}}$)

c_p compressional wave speed

C_Q quadratic artificial viscosity

c_s shear wave speed

$d(\Sigma E_n)/dt$ Impact energy rate of change ($\mathrm{J\,m^{-2}\,s^{-1}}$)

e internal energy

E' Apparent Young's Modulus.

E_f Energy flux

E_n Impact energy from one gauge

E_t Tangent modulus

f_{PL} compression wave frequency in longitudinal direction

f_{PT} compression wave frequency in transverse direction

f_{SL} shear wave frequency in longitudinal direction

f_{ST} shear wave frequency in transverse direction

f_{WT} water frequency in transverse direction

h solid's thickness

s, S_1, S_2 empirical constant

$t0$ time when upward and downward boundary movement self-penetrate.

u_p particle velocity

u_s shock velocity

$v_{\pm}(t)$ jet velocity at time t.

W_p plastic work

z Acoustic impedance ($10^5\times\ \mathrm{N\,s\,m^{-3}}$).

z_1 Acoustic impedance of water.

z_2 Material acoustic impedance ($10^5 Ns.m^3$)

z_2' Material apparent acoustic impedance.

PE Polyethylene

Chapter 1

Introduction

1.1 Background

1.1.1 Cavitation Damage Problem

Cavitation is the formation of small vapor-filled cavities or bubbles owing to rapid changes in pressure; it often occurs in hydro machinery, such as pumps, impellers, and propellers. Approximately, 20% of electricity generated worldwide comes from hydropower and the components inside are highly susceptible to cavitation erosion [1.1] When the resulting bubbles collapse adjacent to the solid boundary, it can result in pitting or erosion of the component. Erosion on the solid material surface begins when plastic deformation occurred due to repeated loads of collapsing bubble clouds with pressure as high as 1000 MPa [1.2]. This erosion or material loss significantly reduces the component life and increases the operating costs; therefore, it is essential to include cavitation damage prediction in the component design process.

1.1.2 Cavitation Damage and Material Properties

Research on cavitation damage prediction has been conducted since the 1930s. One of the objectives of these investigations is to develop phenomenological models based on the correlation between erosion damage and material mechanical properties, such as tensile strength, yield strength, engineering strain energy, true strain energy, hardness, elongation, reduction in area, and elastic modulus [1.3]. Hammitt [1.4] found that the best-fit correlation between the material mechanical properties and cavitation resistance is reciprocal to the maximum mean depth erosion rate ($\frac{1}{MDER_{max}}$). Following this finding, Hattori and Ishikura [1.5] analyzed 990 data points of erosion data (exposure time, mass loss, volume loss, and MDER) of 143 materials (metals, alloys, polymers, and ceramics). Tests were conducted using a vibratory device with water as the liquid medium. The study established that the erosion resistance of

various stainless steels depends on the Vickers hardness of the material's surface before and after the test.

Comprehensive relationship between 5-hour cavitation volume loss and shore hardness of twenty-six different polymeric materials was founded by Barletta et al. [1.6] through cavitation erosion test. The relationship is described as U-shaped: it non-linearly decreases from 0 to 70 of Shore Hardness, stays constant from 70 to 80, then non-linearly increases from 80 Shore Hardness (Figure 1.1) This indicates that there are different material responses in certain ranges of solid surfaces' hardness. However, the underlying damage mechanism that caused this complex relationship still remains unsolved.

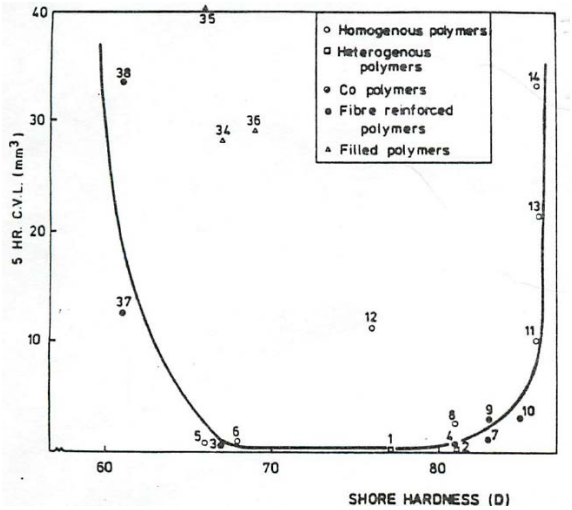

Figure 1.1: 5-hour Cavitation Volume Loss and Shore Hardness from [1.6].

The research of cavitation damage in polymers continue to progress as it can be utilized as coatings for cavitation-prone materials in hydromachinery. Takahashi et al. [1.7] conducted a cavitation erosion test using epoxy resin as a coating material on an aluminum base. The tensile load was included in the erosion test because of its operating conditions; turbomachinery components undergo cavitation along with several other loadings. The results showed that specimen failure occurred prematurely when tensile loading was included. Following this finding, Hibi et al. [1.8] evaluated the performance of epoxy resin with a tensile load in a cavitation erosion test. The results showed that when the tensile load was increased, the time of fracture shortened significantly, indicating the pronounced effect of tensile stress on damage formation.

The above-mentioned findings indicate that the existing phenomenological models do not provide clear insights into material selection in the turbomachinery component design process. This is because the one defining parameter that can clearly correlate material mechanical properties and failure due to cavitation damage remains to be found. Hattori et al. [1.9] considered that this parameter could be the

bubble collapse impact load (BCIL), and thus proposed a new prediction method by measuring individual BCIL under standard cavitation erosion tests. The relationship between the cumulative impact energy ΣF_i^2 (F_i: impact load from an individual bubble collapse) and incubation period (defined in ASTM G 32 as the initial stage of erosion rate-time pattern, in which the erosion rate is zero or negligible compared to later stages) was found to be roughly linear. A further study by Hattori and Itoh [1.10] proposed a broader correlation that not only involves metals and alloys, but also polymers. A similar linear trend was found between the maximum impact loads (Figure 1.2a) and impact energy (Figure 1.2b) the combination of liquid and material acoustic impedances.

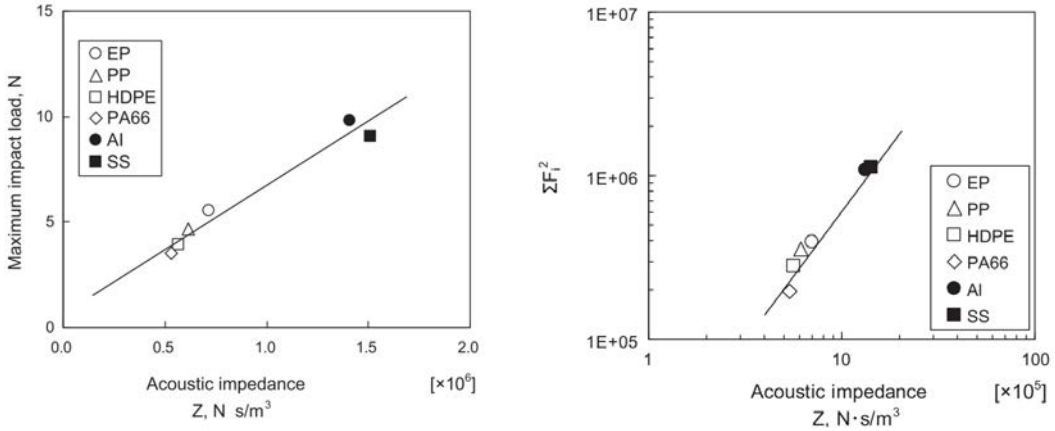

(a) (b)

Figure 1.2: Maximum impact load (a) and cumulative impact energy (b) to acoustic impedance z from [1.10].

This finding is very interesting as it reveals that the BCILs are changing according to solid surface's acoustic impedance. However, no phenomenological model can be made as it is a cumulative measurement as multiple bubbles in cavitation erosion test collapse in a random manner. One of the key to reveal the mechanism of bubble and material interaction is by quantifying the impact loads from single bubble collapse and correlates it directly with corresponding material properties. However, experimentally measuring impact loads from bubble collapse is very challenging because the bubble size in a cavitating flow is much smaller than the sensor size, and the frequency of bubble collapse itself is much higher than the sensor's frequency [1.11]. Therefore, another method is needed to quantify single BCIL to material properties, such as through numerical simulations.

1.1.3 Numerical Simulation of Single Bubble Collapse

Present understanding of cavitation bubble collapse is as follows: when a bubble collapses within a liquid volume, shockwave will emerge and spherical collapse oc-

curred. If the bubble collapses in adjacent to solid boundary, a non-spherical collapse occurred which will emit not only shockwave but also liquid jet that penetrates the solid boundary [1.12]. Due to its invasive nature, the quantification of impact pressure from single non-spherical collapse has been studied in extensive detail through numerical simulation. The non-spherical collapse can be achieved either by modeling vapor bubble collapse or shock-induced collapse.

Bubble collapse types can be divided into Rayleigh-type, where all parts of the bubble surface are exposed simultaneously to a local high pressure similar to vapor, and shock-induced, where a shockwave travels to the bubble, thus inducing it to collapse [1.13]. Despite differences in the driving mechanism, the dynamics of collapse are qualitatively similar in terms of toroidal bubble and high-speed jet formation [1.14]. However, with respect to numerical modeling, shock-induced collapse is more favorable because it can be easily modeled using the numerical tools available.

Recent studies of cavitation bubble collapse numerical simulation are focused on the utilization of coupled solid and fluid solver to incorporate the interaction between bubble collapse and solid material. Hsiao et al. [1.15] developed a numerical model that successfully captured pit formation on a solid surface owing to a single BCIL. The numerical simulation incorporates direct coupling on fluid–structure interaction (FSI), between the incompressible boundary element method (BEM) and compressible finite difference flow solver, to capture bubble dynamics phenomena. Another study by Turangan et al. [1.16] which incorporates the compressibility and coupling of multiple phases (FSI effect) on their Free-Lagrange method, also captured pitting formation on the aluminum wall due to single bubble shock-induced collapse. A meshless SPH solver developed by Joshi et al. [1.17] successfully captured plastic strain on the aluminum wall due to shock-induced collapse of a single bubble.

The standoff distance effect has been extensively researched previously. A cinematographic observation of laser-induced single bubble collapse near rigid wall [1.18] shows that a combination of shockwave and jet, called counterjet phenomena, gives severe impact load to the wall. This counterjet get stronger as the standoff distance γ approaching the value of 1. Conversely, the counterjet starts to get weaker as γ increases and completely disappear when the value is 3. From numerical simulation perspective, all of the study mentioned in previous paragraph agrees that the impact pressure of single bubble collapse become critical when the standoff distance γ are around 1 to 1.2.

In the material domain, elasto-plastic is the most common constitutive model that has been incorporated in the numerical simulation of a single bubble collapse near a solid surface. Choi and Chahine [1.19] used a similar numerical simulation developed by Hsiao et al. [1.15] to deduce peak pressures by using Tabor's formula

from pit geometry. Four metals consisting of aluminum alloys and stainless steel were investigated within elasto-plastic with two linear slopes, one for the elastic regime and the tangent modulus for the plastic regime. Another study by Turangan et al. [1.16] also incorporated an elasto-plastic model on aluminum material, with a constant modulus for the plastic regime. An inference to strain hardening was found by Joshi et al. [1.20] from the 60% over-prediction of plastic strain in the numerical results of to single bubble shock-induced collapse near Aluminum alloy. Therefore, the plasticity effect on the material boundary would be a great starting parameter to explore material's mechanical properties to BCILs.

Other than plasticity, elastic modulus in the form of acoustic impedance is also an important parameter to be analyzed. Recent numerical study by Wang *et al.* [1.21] evaluated the effect of single shock-induced bubble collapse to material acoustic impedance in an extensive detail. The parametric study of the ratio between solid material and water acoustic impedance Z/Z_0 clarified that the impact pressure is defined by the reflection of shockwave from bubble collapse to the solid surface. Higher value of Z/Z_0 indicates 'harder' material, which leads to stronger reflection of shockwave emitted from bubble collapse that can accelerates liquid jet which leads to higher impact pressure. Conversely, lower impact pressure emitted from slower liquid jet for lower value Z/Z_0 due to weaker shockwave reflection. Correlating with results from Hattori and Itoh [1.10], this means that the impact load measured at the solid surface only represents the reflected wave from loads. Hence, it can be deduced that cavitation bubble collapse is essentially wave transfer phenomena.

1.2 Objectives

As mentioned in the preceding section, the relationship between cavitation damage and material properties is an important matter to be solved as it guides material selection to increase the cost performance of hydromachinery. From fluid perspective, bubble collapse impact load (BCIL) and impact energy is an important parameter to quantify the intensity of damage. From solid perspective, acoustic impedance and plasticity are important parameters to unlock the cavitation damage mechanism on solid materials, particularly metals and polymers that are commonly used as main material and coatings for hydromachinery components. Numerical simulation incorporated with coupled fluid-solid solver has proven to be capable of analyzing the interaction between both perspectives in detail within the quantification of single bubble collapse.

In this thesis, I employed a commercially available software incorporated with coupled fluid-solid solver to model a single bubble shock-induced collapse near a solid surface, specifically metals and polymers. The specific objectives of this thesis

are as follows:

1. Validate and verify the capability of the intended numerical software against experimental results of single bubble shock-induced collapse near solid materials.

2. Build a numerical model contains of single bubble near solid material that can represent the cavitation bubble collapse, by comparing the plot of maximum BCIL to acoustic impedance with cavitation erosion test results by [1.10].

3. Explore the effect of plasticity to cavitation damage by varying the material constitutive models of metals and polymers.

4. Analyze the wave propagation behavior of BCIL and cavitation pit formation on the surface to further discuss the underlying damage mechanism due to cavitation bubble collapse on metals and polymers.

1.3 Outline of Thesis

This thesis consists of five chapters. Except for the introduction and conclusion, the outline of this thesis is described as follows:

In chapter 2, we conducted grid verification of a shock-induced collapse air bubble placed inside long and narrow water-filled channel. ANSYS Autodyn R2021 is used as numerical solver. For determining the grid size that will be used in fluid domain, rigid wall was used as boundary near the bubble. For determining the grid size in material domain, Titanium with thickness 5 mm and purely elastic constitutive model was used as boundary wall. After deciding which grid size gives consistent results, validation with several cases of bubble collapse in experimental results is conducted. The first case is laser-induced vapor bubble inside gelatin conducted by Oguri and Ando [1.22]. The shock-front and bubble-wall evolution over time are compared with present numerical simulation. The second case is shock-induced single air bubble collapse near Lucite wall by Shima et al. [1.23]. The averaged wall pressure and collapse distance to wall are compared with present simulations, along with numerical results conducted by Johnsen and Colonius [1.24].

In chapter 3, the effect of plasticity on damage due to shock-induced bubble collapse is explored. Similar numerical model in grid verification is used. The solid boundary consists of three metals (titanium, SS304, Al2024) and three polymers (adiprene, epoxy, and polyethylene). Three different material constitutive models– purely elastic, plastic, and strain-hardening–are employed. The maximum BCIL acting on the surface is compared with maximum impact load in cavitation test results by Hattori and Itoh [1.10] for all cases. The impact energy analogous to

ΣF_i^2 from [1.10] are estimated. The effect of plasticity is discussed by analyzing the relationship of those parameters with acoustic impedance, over different cases of material constitutive models.

In chapter 4, the wave propagation and plastic deformation behavior on metals and polymers due to shock-induced air bubble collapse are explored. Similar numerical model in grid verification is used, with only elasto-plastic constitutive model is used. Other than solid materials used in chapter 3, magnesium, Teflon, and nylon are added in this chapter. The solid thicknesses of the metals were 5 mm, 3 mm, 1 mm and 0.5 mm while those of the polymers were 5 mm, 3 mm and 1 mm. First, the effect of bubble deformation that leads to nonspherical collapse with solid material thickness is explored to ensure how much the contribution of fluid input to the variation of materials and thickness. Then, the results of maximum BCIL acting on the surface for all cases is plotted against acoustic impedance. Wave propagation analysis through Continuous Wavelet Transform is done to analyze which elastic wave parameters dominates the transmission of BCIL inside solid material. On the other hand, an image analysis through MATLAB is used to analyze the apparent plastic deformation in polymers. Cavitation pit volume and depth are estimated and the correlation with yield strength is analyzed. The findings will be used to reveal the damage mechanism behind U-shaped relationship of cavitation volume loss of 27 polymers and Shore hardness in cavitation test results conducted by Barletta et al. [1.6].

In chapter 5, conclusion and future works are described.

References

[1.1] Raghuvir Singh, S. K. Tiwari, and Suman K. Mishra. Cavitation erosion in hydraulic turbine components and mitigation by coatings: Current status and future needs. *Journal of Materials Engineering and Performance*, 21(7):1539–1551, 2012.

[1.2] B. Vyas and C. M. Preece. Stress produced in a solid by cavitation. *Journal of Applied Physics*, 47(12):5133–5138, 1976.

[1.3] B. K. Sreedhar, S. K. Albert, and A. B. Pandit. Cavitation damage: Theory and measurements – A review. *Wear*, 372-373:177–196, 2017.

[1.4] Frederick G. Hammitt. Cavitation Erosion: the State of the Art and Predicting Capability., 1979.

[1.5] Shuji Hattori, Takuya Hirose, and Kenichi Sugiyama. Prediction method for cavitation erosion based on measurement of bubble collapse impact loads. *Wear*, 269(7-8):507–514, 2010.

[1.6] Antonio Barletta. An assessment of polymeric materials and surface treated steels as cavitation erosion resistant materials. *Applied Science thesis, University of Cape Town,*, (March), 1983.

[1.7] Kosuke Takahashi, Daisuke Arai, Kazuaki Inaba, Kikuo Kishimoto, Hiroaki Nakamoto, and Keisuke Hayabusa. Evaluation of Anti-Cavitation Property of Coating Materials for Structural Repair, 2104.

[1.8] Masaharu Hibi, Farid Triawan, Kazuaki Inaba, Kosuke Takahashi, Kikuo Kishimoto, Keisuke Hayabusa, and Hiroaki Nakamoto. Cavitation damage of epoxy resin subjected to uniaxial tensile loading. *Mechanical Engineering Journal*, 5(1):17–00151–17–00151, 2018.

[1.9] Shuji Hattori, Hiroyuki Mori, and Tsunenori Okada. Quantitative evaluation of cavitation erosion. *Journal of Fluids Engineering, Transactions of the ASME*, 120(1):179–185, 1998.

[1.10] Shuji Hattori and Takamoto Itoh. Cavitation erosion resistance of plastics. *Wear*, 271(7-8):1103–1108, 2011.

[1.11] Davide Carnelli, Ayat Karimi, and Jean Pierre Franc. Application of spherical nanoindentation to determine the pressure of cavitation impacts from pitting tests. *Journal of Materials Research*, 27(1):91–99, 2012.

[1.12] Robert T Knapp. Cavitation. *McGraw-Hill, Inc.*, 6, 1970.

[1.13] Anil Kapahi, Chao Tsung Hsiao, and Georges L. Chahine. Shock-Induced Bubble Collapse versus Rayleigh Collapse. *Journal of Physics: Conference Series*, 656(1), 2015.

[1.14] Charles L. Mader. Initiation of detonation by the interaction of shocks with density discontinuities. *Physics of Fluids*, 8(10):1811–1816, 1965.

[1.15] Chao Tsung Hsiao, A. Jayaprakash, A. Kapahi, J. K. Choi, and Georges L. Chahine. Modelling of material pitting from cavitation bubble collapse. *Journal of Fluid Mechanics*, 755(September):142–175, 2014.

[1.16] C. K. Turangan, G. J. Ball, A. R. Jamaluddin, and T. G. Leighton. Numerical studies of cavitation erosion on an elastic–plastic material caused by shock-induced bubble collapse. *Proceedings of the Royal Society A: Mathematical, Physical and Engineering Sciences*, 473(2205):20170315, 2017.

[1.17] Shrey Joshi, Jean Pierre Franc, Giovanni Ghigliotti, and Marc Fivel. Bubble collapse induced cavitation erosion: Plastic strain and energy dissipation investigations. *Journal of the Mechanics and Physics of Solids*, 134, 2020.

[1.18] Olgert Lindau and Werner Lauterborn. Cinematographic observation of the collapse and rebound of a laser-produced cavitation bubble near a wall. *Journal of Fluid Mechanics*, 479(479):327–348, 2003.

[1.19] Jin Keun Choi and Georges L. Chahine. Relationship between material pitting and cavitation field impulsive pressures. *Wear*, 352-353:42–53, 2016.

[1.20] Shrey Joshi, Jean Pierre Franc, Giovanni Ghigliotti, and Marc Fivel. An axisymmetric solid SPH solver with consistent treatment of particles close to the symmetry axis. *Computational Particle Mechanics*, 8(1):35–49, 2021.

[1.21] Yuntian Wang, Xiangguo Zeng, Huayan Chen, Xin Yang, Fang Wang, and Jun Ding. Hugoniot states and mie–grüneisen equation of state of iron estimated using molecular dynamics. *Crystals*, 11(6), 2021.

[1.22] Ryota Oguri and Keita Ando. Cavitation bubble nucleation induced by shock-bubble interaction in a gelatin gel. *Physics of Fluids*, 30(5), 2018.

[1.23] A. Shima, Y. Tomita, D. C. Gibson, and J. R. Blake. The Growth and Collapse of Cavitation Bubbles Near Composite Surfaces. *Journal of Fluid Mechanics*, 203(199):199–214, 1989.

[1.24] Eric Johnsen and Tim Colonius. Shock-induced collapse of a gas bubble in shockwave lithotripsy. *The Journal of the Acoustical Society of America*, 124(4):2011–2020, 2008.

Chapter 2

Grid Verifications and Validation by Experimental Results

2.1 Introduction

To ensure the physical reliability of numerical scheme employed in this study, comparisons with the experimental results will be done. Furthermore, grid verification will be done to evaluate the consistency of solutions obtained. Before discussing such matter, the numerical technique of the intended software of use, ANSYS Autodyn 2021 R1 will be explained first to highlight its capability and limitation.

2.2 Numerical Simulation Technique

The fluid domain used an Eulerian reference frame, which in ANSYS Autodyn 2D axial symmetric solver, works based on first-order accurate multi-material Godunov numerical scheme [2.1, 2]. The governing equation of the fluid domain is based on conservative Euler equations, where compressibility was considered. Surface tension and phase change are ignored, resulting in an adiabatic and inviscid flow. The conservative form can be expressed as:

$$\frac{\partial \mathbf{U}}{\partial t} + \nabla \cdot \mathbf{F} = \mathbf{0}; \quad \mathbf{U} = \begin{bmatrix} \rho \\ \rho \mathbf{u} \\ E \end{bmatrix}; \quad \mathbf{F} = \begin{bmatrix} \rho \mathbf{u} \\ \rho \mathbf{u}^2 + p \\ \mathbf{u}(E + p) \end{bmatrix} \tag{2.1}$$

With ρ as density, u as velocity, p as pressure, and E as the total energy. The conserved variables are expressed as $\mathbf{U}$ and fluxes are $\mathbf{F}$. The first-order Godunov's Scheme works in the time evolution part, where it explicitly incorporates the physics of waves in the approximation of fluxes at grid interfaces. The relation between grid size and solution's stability are defined by Courant condition [2.3]. The appropri-

ate Courant number is related to the convergence of results concerning grid size. Therefore, the selection process will be explored in Section 2.3.

The conserved variables in Equation 2.1 are determined by the equation of states (EOS) for each material. For water and air, this is the primary response of dynamic loading, as it cannot sustain shear thus the condition is assumed to be fully hydrodynamic. For solid materials, the EOS becomes the primary response at high deformation rates, where hydrodynamic pressure is greater than the yield stress limit. However, the stress and deformation response are determined by constitutive models which will be explained more in Chapter 3.

The Equation of States for air is based on ideal polytropic gas, where the adiabatic exponent γ_{EOS} value is 1.3. This EOS has been widely used to model gas bubble shock-induced collapse [2.4–6]. At the initial state, pressure is assumed to be equal to atmospheric pressure (101.325 kPa), hence the internal energy e was calculated accordingly:

$$p = (\gamma_{EOS} - 1)\rho e \tag{2.2}$$

The Equation of States for water and solid materials is based on Rankine-Hugoniot for shock jump conditions. This EOS type was chosen because it has been proven against experimental results that it is suitable to handle the shock propagation inside and across fluid and solid domain of a water-filled tube [2.7]. From many dynamic experiments of each material, an empirical relationship between shock velocity u_s and particle velocity u_p can be stated as:

$$u_s = c_0 + su_p \tag{2.3}$$

With c_0 is sound velocity in the initial state and s is empirical constant. Mie-Gruneisen coefficient Γ determined the pressure and energy, with H subscript denotes pressure and internal energy in the Hugoniot or shock state:

$$p = p_H + \Gamma\rho(e - e_H) \tag{2.4}$$

The Hugoniot pressure state p_H and internal energy e_H are obtained from its initial state, denoted by 0 subscripts. There is an element of compression μ introduced. The relation can be expressed as:

$$p_H = \frac{p_0 p_0^2 \mu(1+\mu)}{[1-(s-1)\mu]^2}; \qquad e_H = \frac{1}{2}\frac{p_H}{p_0}\left(\frac{\mu}{1+\mu}\right) \tag{2.5}$$

The Shock EOS Linear in ANSYS Autodyn includes quadratic velocity equation that can be expressed as:

$$u_s = c_0 + S_1 u_p + S_2 u_p^2 \tag{2.6}$$

With sound velocity at the initial state c_0, Gruneisen coefficient Γ, coefficient S_1 and S_2 obtained from Autodyn Material Database.

The multi-material definition inside the fluid domain is based on the volume of fluid (VOF) method which actively tracks the amount of material in each time step. To allow the calculation of the resultant stress tensor which is then used to calculate cell impulses, momentum, and mass transport, there are two algorithms available in ANSYS Autodyn. First, if a grid containing only two different gases, an iterative procedure will be used to establish an equilibrium state. Second, if a grid contains two or more non-gaseous materials, a stiffness weighted averaging technique is used. The choice of algorithm is automatic and local for each grid.

An air bubble induced by a shockwave undergoes rapid pressure change which then leads to collapse and produce jet impact to wall boundary. In that process, there are two important numerical technique which affects the degree of physical reliability of the results. First, is multi-material transportation technique. As the solution goes through from one time step to the next, an algorithm must be employed to decide which and how much material is needed to be transported across the grid. ANSYS Autodyn incorporates SLIC (Single Line Interface Construction) technique to calculate the order and quantity of material transport. This method affects the deformation of the air bubble after it was induced by the planar shockwave.

The last and upmost important aspect is the treatment of shock discontinuities which occurred due to strong impacts and the non-linearity of equations being solved. To ensure smooth computational solution, ANSYS Autodyn incorporates artificial viscous terms which is based on the work of Von Neumann and Richtmeyer and Wilkins [2.1]:

$$q = \begin{cases} \rho \left[\left(C_Q d \left(\frac{\dot{V}}{V} \right) \right)^2 - C_L c \left(\frac{\dot{V}}{V} \right) \right], & \text{for} \quad \frac{\dot{V}}{V} < 0 \\ 0, & \text{for} \quad \frac{\dot{V}}{V} > 0 \end{cases} \tag{2.7}$$

With C_Q as quadratic artificial viscosity coefficient, C_L is linear artificial viscosity coefficient, d is typical element length scale, c is the local sound speed and $\frac{\dot{V}}{V}$ is the rate of change in volume. The C_Q role is to smooth out shock discontinuities while the C_L damps out oscillations. The selected value of C_Q and C_L is 1 and 0.2, which is based on Autodyn's default value.

The solid domain is based on Arbitrary Lagrangian-Eulerian (ALE) reference frame. This reference frame operates similar to Lagrangian coordinates, where nodes move along with the material motion. However, one of its distinctive advantages is that it allows automatic rezoning, which was found to be useful in handling excessive deformation such as in polymers' coated surface case. This technique is particularly

suited for a variety of fluid-structure interaction problems[2.8]. The conservation of mass, momentum, and energy can be expressed using these equations:

$$\begin{aligned} \rho\ddot{x} &= b_x + \frac{\partial \sigma_{xx}}{\partial x} + \frac{\partial \sigma_{xy}}{\partial y} \\ \rho\ddot{y} &= b_y + \frac{\partial \sigma_{yx}}{\partial y} + \frac{\partial \sigma_{yy}}{\partial y} \\ \dot{e} &= \frac{1}{\rho}(\sigma_{xx}\dot{\epsilon_{xx}} + \sigma_{yy}\dot{\epsilon_{yy}} + 2\sigma_{xy}\dot{\epsilon_{xy}}) \end{aligned} \tag{2.8}$$

With σ and ϵ represents stress and strains of the solid material. The governing equations above when combined with material constitutive models and boundary conditions, define the complete solution for the solid domain. The explanation of materials constitutive models will be carried out in the Chapter 3.

The coupling method of fluid and solid domain is based on two-way fluid structure interaction [2.1]. The interaction automatically starts when two domains with different reference frame (e.g., Eulerian and ALE) come into contact. The main principle is ALE domain covers the regions of Eulerian domain. At the beginning of the simulation, the Eulerian domain was made to overlap with ALE domain which was then positioned to achieve desired stand-off distance (Figure 2.1). This makes both bodies come into contact from the beginning, thus ensuring a realistic condition of an air bubble placed in a nearby solid wall. The remains of overlapped Eulerian domains will be automatically converted into void, while the interface region will be changed into an updated control volume on which the conservation equation of mass, momentum, and energy are solved.

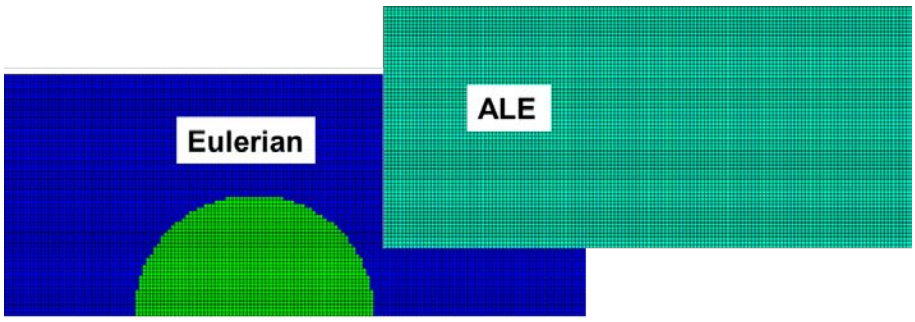

Figure 2.1: Overlapped fluid domain (Eulerian) placed behind solid material domain (ALE).

Kojima and Inaba [2.7] employed this coupling method to simulate wave propagation across a water-filled circular tube with solid buffer using ANSYS Autodyn. An overlapped Eulerian domain was applied behind the Lagrangian domain, so that the contact occurred from the beginning of the simulation. The pressure, velocity, and strain at the interface are shown to be close with experimental results, implying that this coupling method is capable of handling shock propagation between fluid

and solid domain. However, to attain more confidence in the physical reliability of not only in the coupling method, but also the material transport and the artificial viscosity coefficient to handle shock discontinuities, two validations against experimental study will be carried out in Section 2.4.

2.3 Grid Verifications

According to the ASME Guide for V&V in computational solid mechanics [2.9] there are two types of verification: code verification and calculation verification. Autodyn is an explicit hydrocode that is available in worldwide usage to model impact, penetration, blast, and explosion events [2.10]. It has been extensively used and validated with experiment to demonstrates damage to the structure owing to the high-speed impact from the explosive charge [2.11], as well as impact in underwater explosions [2.12–14]. Hence, code verification is considered to be unnecessary.

2.3.1 Problem Description

In this present work, a spherical bubble filled with atmospheric pressure air was placed at the closed end of a slender water-filled channel with 55 mm length and 1 mm width (Figure 1). The region marked with red color depicts water with properties of internal energy of 3.75 GJ/kg. This high-energy region produces a planar shockwave with 913 MPa shock-front pressure that propagates into two directions: the open end where the non-reflective or transmit boundary was applied and to the closed end where an air bubble with 0.5 mm radius resides. This planar shockwave increases surrounding pressure around the bubble, thus inducing it to collapse.

As the bubble collapse, shock which emitted from jet impact was captured first to the boundary's surface. Two types of boundaries were analyzed: a rigid wall (Figure 2.2a) and coated surfaces with 5 mm thickness (Figure 2.2b). The distance from the center radius to the boundary wall is 0.53 mm (stand-off distance γ=1.06), fixed for all cases. To distinguish the effect of the planar shockwave on the bubble collapse impact, a model similar to a rigid wall type but without a bubble (shock-only case) was also analyzed (Figure 2.2c).

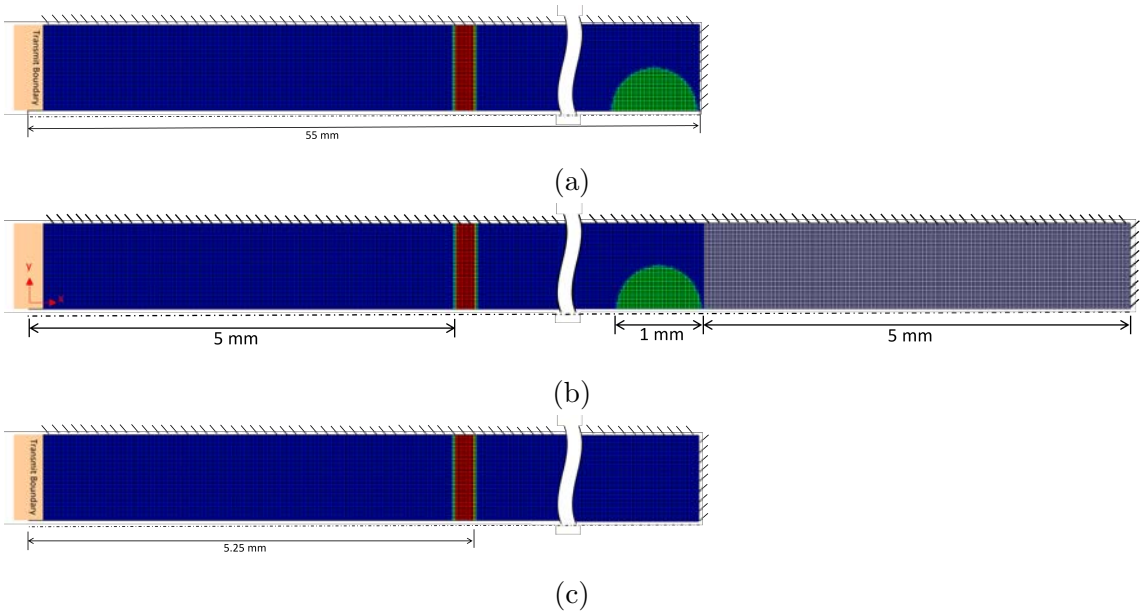

Figure 2.2: Simulation model for (a) rigid wall (b) coated surface and (c) rigid wall without bubble.

From Figure 2.2, two domains are visible: fluid and solid side. The material properties used for air, water, and solid material which is Titanium with elastic perfectly-plastic model are describe in Table 2.1.

Table 2.1: Material Properties for Grid Verification.

Property	Air	Water	Titanium
Equation of State			
Density ρ [kg m^{-3}]	1.225	1000	4510
Tensile Limit [MPa]	-	-100	-
γ_{EOS}	1.4	-	-
e [kJ/kg]	2.068×10^5	-	-
Elastic Modulus [GPa]	-	-	120
Yield strength σ_y [MPa]	-	-	850

Grid verification was done to both Eulerian and ALE solver. To ensure the consistency of calculation verification, the time step in this simulation was carefully controlled to fulfill the Courant condition [2.3] which can be stated with:

$$\Delta t \leq f \, \frac{\Delta h}{c} \tag{2.9}$$

Where Δt is time increment, f is stability time step factor, Δh as characteristic dimension of element and c is the local sound speed. The time step is determined

by the smallest grid size in the whole model. The calculation verification method was performed using mesh with the sizes described in Table 2.2.

Table 2.2: Mesh size conditions for calculation verification test.

Mesh Size	Grid Number ($i \times j$)	
	Fluid Region	Solid Region
0.0250 mm × 0.0250 mm	2200 × 40	200 × 40
0.0200 mm × 0.0200 mm	2750 × 50	2750 × 50
0.015 mm × 0.0150 mm	3667 × 67	334 × 67
0.0125 mm × 0.0125 mm	4400 × 80	400 × 80

2.3.2 Grid Verification on Solid and Fluid Domain

First, the calculation verification step was performed for the fluid area on the rigid wall using bubble simulation (Figure 2.2a). Gauges were installed every 0.5 mm, from 5 mm to 55 mm, where a rigid wall was located. The maximum pressure from 0–0.0375 ms simulation time is mapped in Figure 2.3a. Good agreement was achieved along x coordinates, although some fluctuations occurred at 20–35 mm. Fluctuation also occurred at 47–55 mm, near the area where the air bubble was placed. A similar calculation verification step was performed on the shock-only model shown in Figure 2.2c. The results shown in Figure 2.3b validate that, without air bubbles near the rigid wall, fluctuations did not occur between the maximum pressures values on various meshes.

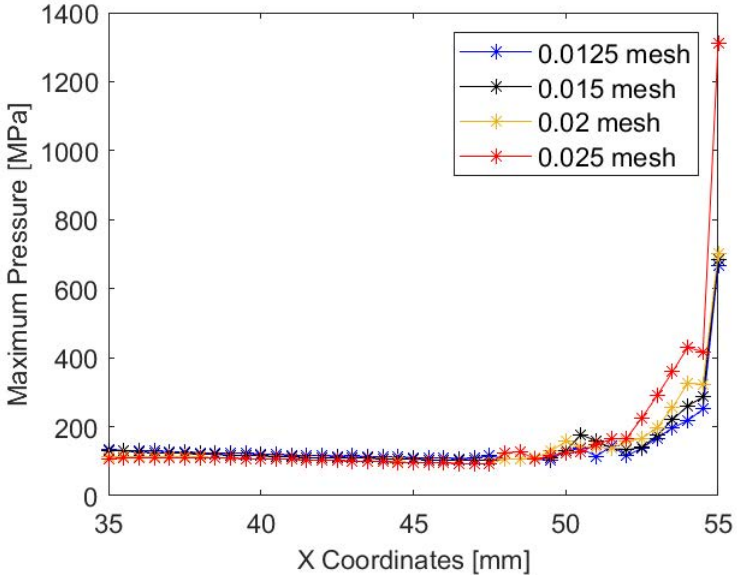

(a)

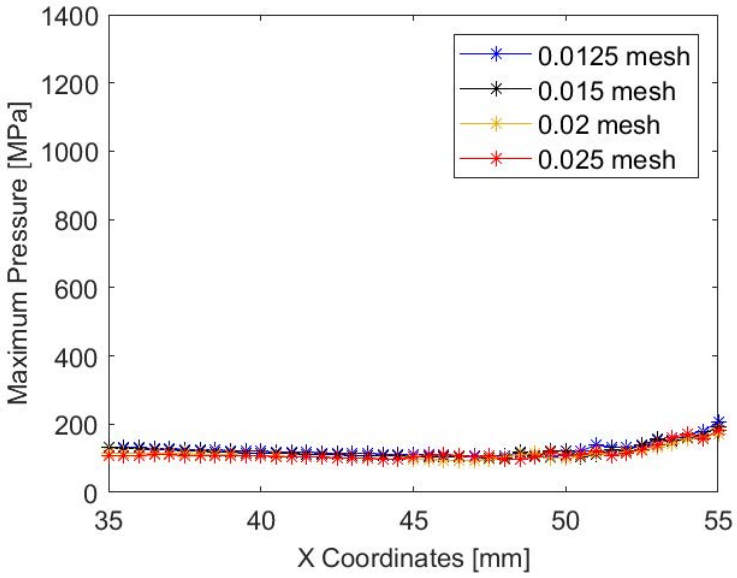

(b)

Figure 2.3: Maximum pressure along x coordinates for (a) rigid wall model with bubble, (b) shock-only model.

Further analysis on cavitation damage prediction will be performed focusing only on pressure values emerging from bubble collapse at the boundary wall. Figure 2.4a shows the maximum pressure value at the rigid wall model with bubbles, with various mesh sizes. Result shows that from 0.02–0.0125 mm mesh length, the difference between maximum pressure values is less than 10%. Similar trends were also observed in the shock-only case (Figure 2.4b). However, for the shock-only case, a difference of less than 10% was achieved at 0.015 mm. Therefore, for the fluid area, a 0.015 mm mesh length was chosen for further simulation with the coated surface

case.

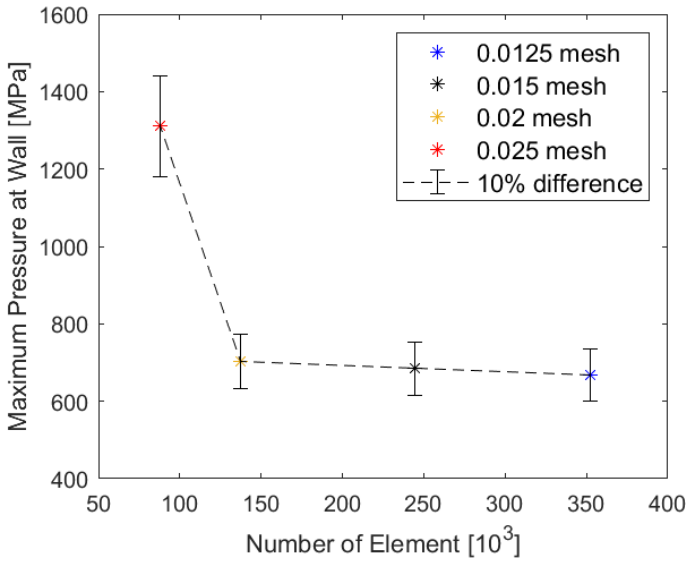

(a)

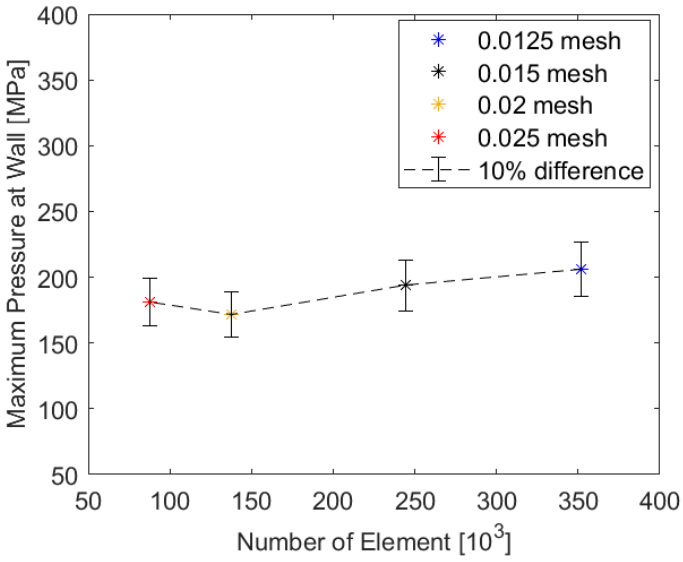

(b)

Figure 2.4: Maximum Pressure at wall for (a) rigid wall model with bubble, (b) shock-only model.

The calculation verification for the coated surface case (Figure 2.2b) was performed with a 0.015 mm mesh length in the fluid area. To ensure similar time-step was used in all cases, for the solid domain, no other grid size smaller than 0.015 mm is analyzed. Gauges were installed at the center of the axial symmetry axis every 0.1 mm from the coated material surface up to a thickness of 5 mm. The maximum pressure from 0–0.0375 ms simulation time is shown in Figure 2.5a. The high pressure emitted from a bubble collapse in a short time, as well as the narrow computational model, made the pressure wave reflection complex. Therefore,

good agreement was achieved only around the middle part of the thickness. Further analysis will focus more on the pressure value at the material's surface. Figure 2.5b shows the maximum pressure value at the surface of the coated material with various mesh sizes. The results show that starting from a 0.015 mm mesh size, the difference in the maximum pressure value is less than 10%. Therefore, a mesh size of 0.015 mm was chosen for the coated surface area case. This 0.015 mm mesh size gives 34 nodes for 0.5 mm bubble radius, which will be used for validation process in the next section.

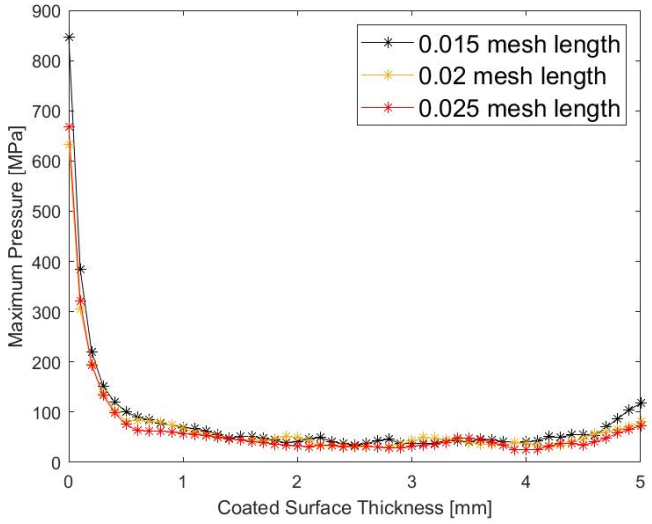

(a)

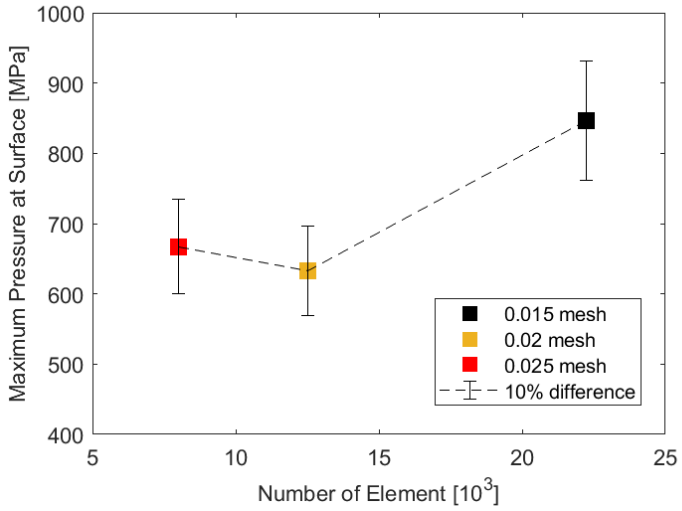

(b)

Figure 2.5: Maximum pressure (a) along coated surface thickness and (b) at coated material's surface.

2.4 Validation With Experimental Results

The 2D axial symmetric numerical technique used in this study is validated against two experiments: laser-induced bubble inside gelatin gel by Oguri and Ando [2.4] and shock-induced gas bubble by Shima et al. [2.15]. To attain similar consistency in the CFL number, similar nodes for bubble radius (34 nodes for 0.5 mm bubble radius) as obtained from grid verification process is used.

2.4.1 Laser-Induced Single Bubble Collapse

The experimental settings conducted by Oguri and Ando [2.4] involves Q-switched Nd:YAG laser to create a nucleation inside gelatin gel, which emits spherical shock-wave. The evolution of bubble wall and shock-front were observed. They also conducted a 2D axial symmetric numerical simulation using similar shock-interface capturing scheme developed by Johnsen and Colonius [2.16]. The results were compared with the evolution of laser induced phenomena in the experiment.

The EOS used for all materials in the numerical simulation of [2.4] was Stiffened Gas EOS. The laser bubble nucleation was assumed as vapor with two initial plasma conditions: 6 μm and 1.9 GPa internal pressure. This internal pressure was adapted as pressure p in the Ideal Gas EOS used in this study (Equation 2.2). Hence, with known γ and density ρ, the internal energy e can be calculated and inputted as initial condition. For the 10% wt gelatin gel, the parameters provided from Stiffened Gas EOS was adapted to Shock Linear EOS. However, for Gruneisen coefficient Γ, because it is not provided in the study, the value of 0.17 was used [2.17]. The detailed material properties can be seen in Table 2.3.

Table 2.3: Material Properties for validation with [2.4]

Property	Vapor	Gelatin 10% wt
Equation of State	Ideal Gas	Shock EOS Linear
Polytropic Const. γ_{EOS}	1.3	-
Mie Gruneisen Coeff. Γ	-	0.17
Density ρ (kg/m^3)	0.75	1030
Sound Speed c (m/s)	419	1553
Young's Modulus E (kPa)	-	60
Internal Energy e (kJ/kg)	8.44×10^9	-

For the numerical domain, similar initial vapor radius $R_0 = 6\,\mu$m was used. Non-reflective boundary was used on each free edges. The width and height of gelatin domain were adjusted so that the shock-front can be observed within desired time.

The nodes to bubble radius obtained from the verification process in Section 2.3 was used, which resulting in 0.015 µm × 0.015 µm grid size. The schematic of simulation model can be seen in Figure 2.6.

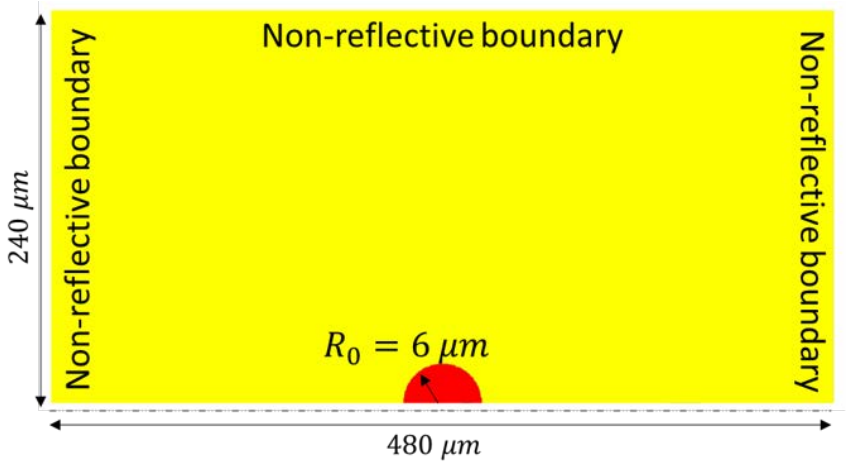

Figure 2.6: Simulation model of laser induced bubble (red) inside 10% wt gelatin gel (yellow).

The evolution of bubble wall and shock-front until 80 ns can be seen in Figure 2.7. It is shown that the results of numerical simulation from this study agrees well with both experimental and numerical results of [2.4]. This also indicates that the default values of artificial viscosity coefficient (C_Q and C_L in Equation 2.6) provided from ANSYS Autodyn to minimize shock discontinuities are sufficient.

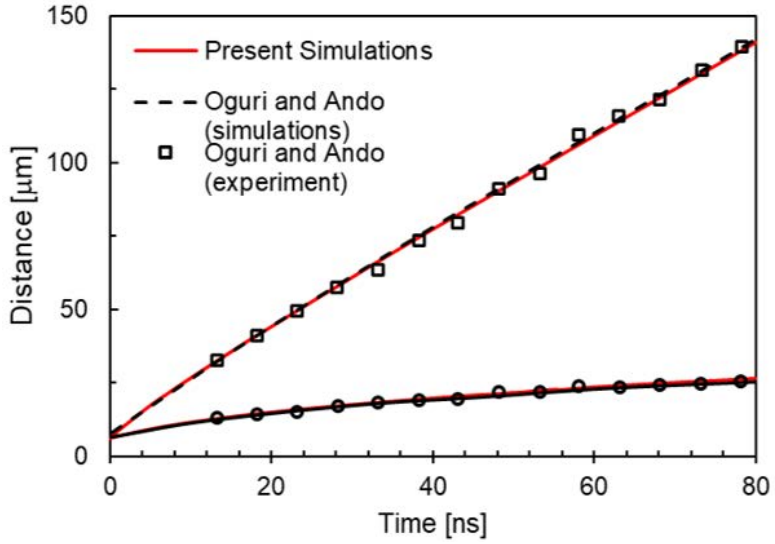

Figure 2.7: The evolution of laser-induced bubble phenomena inside 10%wt gelatin gel.

2.4.2 Shock-Induced Single Bubble Collapse Near Lucite Wall

To further ensure the physical reliability of numerical scheme of handling shockwave and bubble interaction, comparisons with the experimental results by Shima et al. [2.15] are carried out. A spherical shockwave emerged from electrical discharge interacts with pre-existed gas bubble located near a Lucite wall. The gas bubble was kept under various value of stand-off distance γ from the wall with an 80 µm thin iron wire, which the effect was deemed to be negligible. The shockwave was kept at a constant strength and a pressure sensor was installed at the wall to measure impulsive pressure from the gas bubble collapse.

Johnsen and Colonius [2.18] conducted a similar process to validate their own numerical solver for shock-bubble interaction cases. The simulations were set up as to match the experiment. However, there is no coupling of fluid and solid domain in the simulation. Therefore, a finite acoustic impedance value based on Lucite material's characteristic was employed to the rigid wall. The results of averaged pressure on the wall were shown to have the same trends with the experiments.

Considering above matters, a coupled fluid and solid simulations with the same numerical scheme and settings as described in Section 2.2 was conducted in this validation process. Similar properties for water and air as described in Table 2.1 were used. Similar mesh to bubble ratio as in the final grid verification result, which in this case become 136 nodes for 1 mm bubble radius, is used. The Lucite wall was mentioned to be rigid enough with no specific thickness value mentioned, therefore it was arbitrary selected. After several attempts, it was found that the thickness value of 24 mm with elastic constitutive model can represent the phenomena well. The material properties of Lucite are described in Table 2.4.

Table 2.4: Material properties for Lucite wall.

ρ [kg m^{-3}]	E [GPa]	z [$10^5\times$ N s m^{-3}]	c_0 [m s^{-1}]
1180	6.03	26.67	2260

In an underwater electrical discharge phenomenon, a spherical shockwave was emerged from imploding bubble in the form of vapor. Johnsen and Colonius [2.18] used an assumption that the incoming shock from electrical discharged has an amplitude of 2.5 MPa, with an exponential decay of 15 µm for 1 mm bubble radius. To re-create similar profile, vapor with Ideal Gas EOS properties obtained from Oguri and Ando [2.4], as described in Table 2.3 was used. The geometry of the vapor is ellipsoidal, with R_a = 0.6 mm and R_b=0.8 mm, placed within 18.8 mm from the bubble center. Non-reflective boundary condition was used on left and upper fluid's

edge while the boundaries of Lucite wall were both fixed. The numerical model is shown in Figure 2.8.

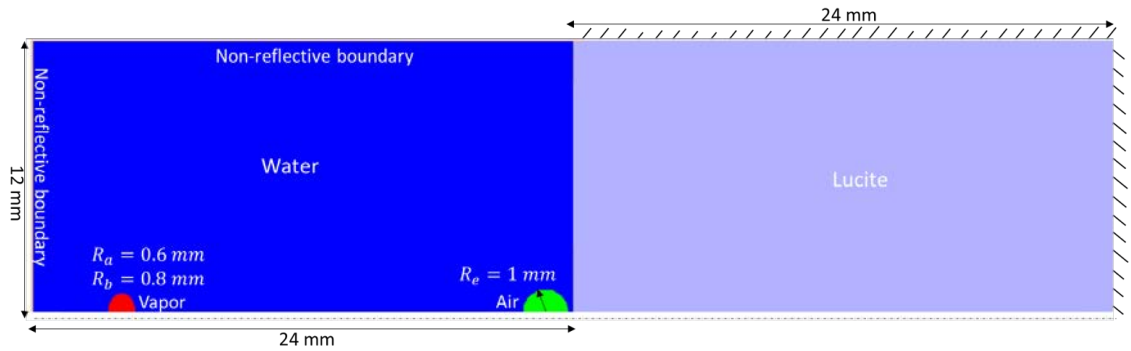

Figure 2.8: Simulation model for validation of spark-discharged and air bubble interaction near Lucite wall. R_a and R_b are the size of elliptical-shaped vapor (red) to generate spark-discharged shockwave.

A separate case without an air bubble were simulated to check the generated shock pressure profile from the emerging vapor. A shockwave with spherical shape was formed, and the pressure profile at 17.8 mm from vapor center is shown in Figure 2.9. It is shown to match with the incoming shock profile characteristic described by Johnson and Colonius [2.18], which is shown in figure 8 as a dashed line. Therefore, the distance between vapor and air bubble is kept constant regardless of various stand-off distance ($\gamma = H_0/R_0$) values will be used in the validation process.

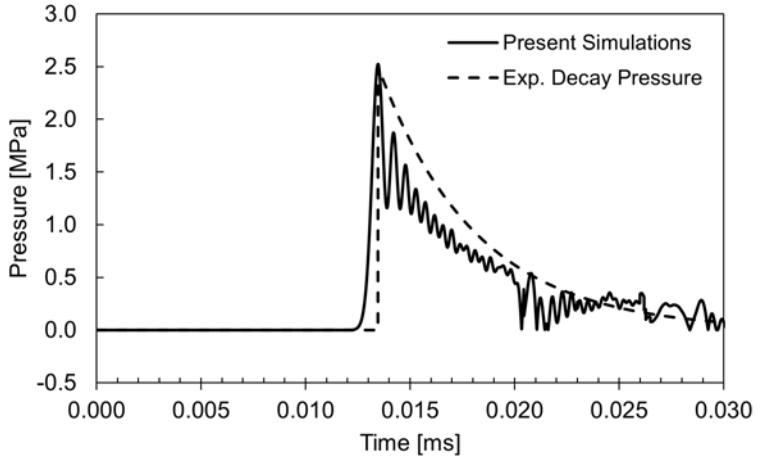

Figure 2.9: The incoming shock profile measured at 17.8 mm from vapor center on the axisymmetric line. The dashed line is the targeted shock profile, with maximum pressure 2.5 MPa exponentially decay for 15 µm.

A comparison between the present simulations, shock-induced collapse simulations by Johnson and Colonius [2.18], and the experiments of Shima et al [2.15] are shown in Figure 2.10. The results of maximum wall pressure averaged across pres-

sure sensor used in the experiment and the distance between bubble collapse and the wall are presented. The wall pressure was extracted at the timing where maximum pressure was reached at the axisymmetric center ($y = 0$), then it is averaged over the area of pressure sensor used in the experiment. The distance between bubble collapse and the wall H_c was extracted when toroidal bubble shape firstly occurred.

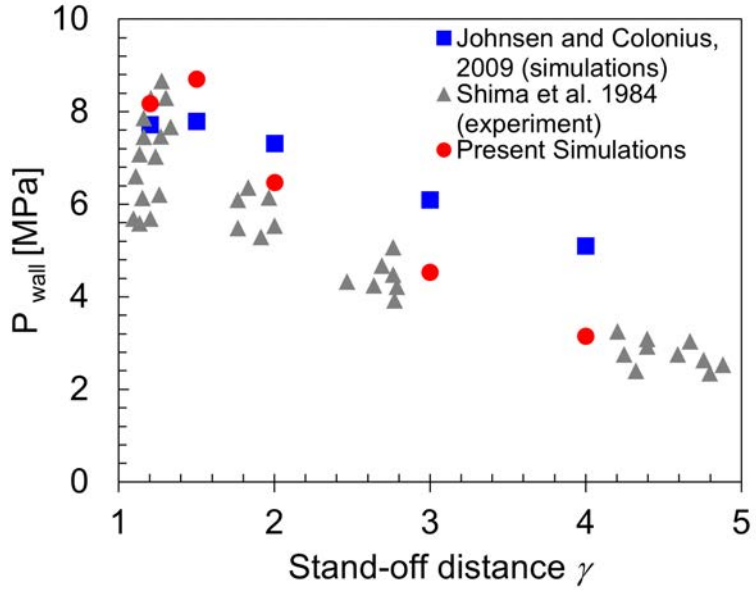

(a)

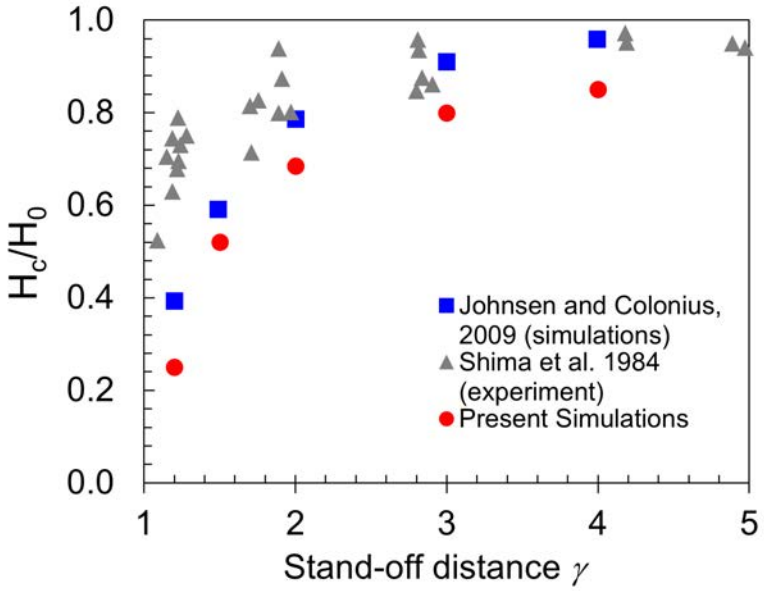

(b)

Figure 2.10: Comparison between present simulation, experiment by Shima et al. (1984) and simulation from Johnsen and Colonius (2009) for (a) averaged wall pressure and (b) collapse distance to the wall.

The overall trend of wall pressure is decreasing as stand-off distance increases. The results from present simulations show closer estimation to the experiment, com-

pared with numerical simulations form Johnsen and Colonius [2.18]. This shows that a coupled fluid and solid simulation with constitutive material model employed provides better estimation of bubble collapse impact pressure than a finite acoustic impedance value applied to a rigid wall. However, the collapse distance from the wall from present simulations results are shown to be under-predicted compared with [2.18]. This might be because the SLIC algorithm to determine multi-material transport incorporated in ANSYS Autodyn is not as sophisticated as the high-order accurate weighted essentially non-oscillatory (WENO) algorithm to capture bubble interface employed by Johnsen and Colonius [2.18]. Nevertheless, because the focus of this study is to predict cavitation damage by analyzing BCILs on the solid surface, this validation results is deemed to be enough for ensuring the physical reliability of the numerical scheme used in this study.

2.5 Summary

In this chapter, we described in detail the numerical technique of the coupled fluid-solid solver intended of use, ANSYS Autodyn, that involved in solving shock-induced bubble collapse and its interaction with solid material. Several parameters were deemed to be important: the type of EOS for the multi-material definition, C_Q and C_L which treat non-linearity of equations and shock discontinuities, and the FSI technique. The explicit time integration that is used to solve the governing equation relies heavily on the grid size, which affecting the consistency of the solution. Therefore, validations with several experimental results were done to evaluate the important parameters and grid verification process was done to achieve the solution consistency.

In the grid verification, the process was analyzed separately between fluid and solid domain. The problem used for this analysis is a long and narrow water-filled channel with air bubble placed on the edge. For the fluid domain, rigid wall boundary condition was used. Hence, coupled fluid-solid solver was not involved in this case. The default value of C_Q and C_L were used. The grid size was rectangular and uniform for all the domain. Four grid sizes were analyzed: 0.025 mm, 0.02 mm, 0.015 mm and 0.0125 mm. Results reached consistency on 0.015 mm grid size, which is specifically 34 nodes per 0.5 mm bubble radius. This grid size will be used as a base for every simulation in the fluid domain analyzed in this study. Next, for the solid domain, rigid wall was replaced with elastic perfectly plastic Titanium wall with 5 mm thickness. In this case, the FSI technique was also used. Results show that the solution reached consistency when the grid size is 0.015 mm.

The first validation process was against laser-induced bubble inside gelatin gel by Oguri and Ando [2.4]. Vapor bubble was created from a focusing Nd:YAG laser

inside the gelatin gel. Hence, for this case the FSI technique was not incorporated. Ideal gas EOS was used for model the vapor, with parameters adapted from the stiffened gas EOS used on the study. Shock EOS Linear was used to model 10% gelatin, with Γ coefficient adapted from [2.17]. The default value of C_Q and C_L were used. Similar grid size obtained from the final results of verification process was used. The comparison of bubble and shock-front between present simulations, experiment results and in-house numerical solver of [2.4] shows good agreement.

The second validation process was against shock-induced air bubble collapse near Lucite wall conducted by Shima et al. [2.15]. Similar grid size as verification and default value of C_Q and C_L were used. The EOS type employed for water and air were Shock EOS Linear and Ideal Gas, respectively. The shockwave was generated from spark-discharged and modeled as vapor in Ideal Gas EOS with properties adapted from [2.4]. The material properties for water, air, and purely elastic Lucite wall were obtained from Autodyn's material database. The averaged pressure at wall from present simulations shows closer results to the experiment than numerical simulations developed by [2.18] which used rigid wall. This shows that the present simulations provides better estimation because it incorporated FSI to represent the Lucite wall.

References

[2.1] ANSYS. ANSYS Explicit Dynamics Analysis Guide. (July):394, 2020.

[2.2] Sergei Godunov. Finite difference method for numerical computation of discontinuous solutions of the equations of fluid dynamics. *Matematicheskii Sbornik*, 47(89)(3):271–306, 1959.

[2.3] Richard Courant, Kurt Friedrichs, and Hans Lewy. Über die partiellen Differenzengleichungen der mathematischen Physik. *Mathematische annalen*, 100(1):32–74, 1928.

[2.4] Ryota Oguri and Keita Ando. Cavitation bubble nucleation induced by shock-bubble interaction in a gelatin gel. *Physics of Fluids*, 30(5), 2018.

[2.5] Eric Johnsen and Tim Colonius. Numerical simulations of non-spherical bubble collapse. *Journal of Fluid Mechanics*, 629:231–262, 2009.

[2.6] N. A. Hawker and Y. Ventikos. Interaction of a strong shockwave with a gas bubble in a liquid medium: A numerical study. *Journal of Fluid Mechanics*, 701:59–97, 2012.

[2.7] Tomohisa Kojima and Kazuaki Inaba. Numerical analysis of wave propagation across Solid–Fluid interface with Fluid–Structure interaction in circular tube. *International Journal of Pressure Vessels and Piping*, 183(April):104099, 2020.

[2.8] Naury K. Birnbaum, Nigel J. Francis, and Bence I. Gerber. Coupled techniques for the simulation of fluid-structure and impact problems. *Computer Assisted Mechanics and Engineering Sciences*, 6(3):295–311, 1999.

[2.9] L. E. Schwer. An overview of the PTC 60/V&V 10: guide for verification and validation in computational solid mechanics. *Engineering with Computers*, 23(4):245–252, 2007.

[2.10] Norman Robertson, Colin Hayhurst, and Greg Fairlie. Numerical simulation of impact and fast transient phenomena using AUTODYN™-2D and 3D. *Nuclear Engineering and Design*, 150(2-3):235–241, 1994.

[2.11] A. A.Akbari Mousavi and S. T.S. Al-Hassani. Numerical and experimental studies of the mechanism of the wavy interface formations in explosive/impact welding. *Journal of the Mechanics and Physics of Solids*, 53(11):2501–2528, 2005.

[2.12] A. Abe, M. Katayama, K. Murata, Y. Kato, and K. Tanaka. Numerical study of underwater explosions and following bubble pulses. *AIP Conference Proceedings*, 955(2007):1355–1358, 2007.

[2.13] Hao Huang, Qing Jie Jiao, Jian Xin Nie, and Jian Feng Qin. Numerical modeling of underwater explosion by one-dimensional ANSYS-AUTODYN. *Journal of Energetic Materials*, 29(4):292–325, 2011.

[2.14] Hans Mair. Hydrocode methodologies for underwater explosion structure medium/interaction. *Shock and Vibration*, 2:227–248, 1995.

[2.15] A. Shima, Y. Tomita, D. C. Gibson, and J. R. Blake. The Growth and Collapse of Cavitation Bubbles Near Composite Surfaces. *Journal of Fluid Mechanics*, 203(199):199–214, 1989.

[2.16] Eric Johnsen and Tim Colonius. Implementation of WENO schemes in compressible multicomponent flow problems. *Journal of Computational Physics*, 219(2):715–732, 2006.

[2.17] Gil Ho Yoon, Jun Su Mo, Ki Hyun Kim, Chung Hee Yoon, and Nam Hun Lim. Investigation of bullet penetration in ballistic gelatin via finite element simulation and experiment. *Journal of Mechanical Science and Technology*, 29(9):3747–3759, 2015.

[2.18] Eric Johnsen and Tim Colonius. Shock-induced collapse of a gas bubble in shockwave lithotripsy. *The Journal of the Acoustical Society of America*, 124(4):2011–2020, 2008.

Chapter 3

Plasticity Effects on Bubble Collapse Impact Loads of Metals and Polymers

3.1 Introduction

The role of plasticity in determining damage due to cavitation bubble collapse in solid material has been an interest for experimental studies that employed cavitation erosion test in the method. Several early studies [3.1, 2] have confirmed that the erosion rate of Aluminum and Steels are directly proportional to yield strength, hardness, and ultimate strength. Later, Hattori and Itoh [3.3] found a correlation between bubble collapse impact loads and impact energy to material's elastic properties, acoustic impedance. The materials that being tested were Aluminum, Steel, PA66, HDPE, Epoxy, and Polypropylene. These contradicting findings lead to uncertainty that caused the main deciding parameter of cavitation damage inside solid material properties remains unknown.

The convenient part of utilizing numerical simulation is the ability to control parameters that is useful to analyze the causality of a problem. Hence, in order to analyze whether it is elasticity or plasticity in solid material properties that affect cavitation damage performance, three material constitutive models–purely elastic, elastic perfectly plastic, and strain-hardening–will be used. Three types of metals: SS304, Titanium, and Al2024, and three types of polymers: Adiprene, Epoxy, and Polyethylene (PE) will be analyzed. Bubble collapse impact loads (BCIL) and impact energy analogous to ΣF_i^2 from Hattori and Itoh [3.3] will be estimated from the numerical simulation results. Moreover, the maximum BCIL will also be compared with [3.3].

3.2 Methods

3.2.1 Problem Description

In this chapter, similar case of a spherical bubble filled with atmospheric pressure air inside water-filled channel as described in Section 2.3.1 is analyzed (Figure 2.2). The solid material thickness is 5 mm. The grid size is rectangular and uniform in all domain with size 0.015 mm. The material properties and EOS of air and water can be seen in Table 2.1.

In shock-induced collapse, the incoming shockwave reflected as a rarefaction wave that occurred due to the impedance mismatch between air and liquid. Quinto-Su and Ando [3.4] studied cavitation bubble clouds phenomena by introducing a pair of nucleation bubbles in water generated by laser. They observed multiple reflected rarefaction wave dues occurred due to the collapse and interaction between a pair of nucleation bubbles in water. In order to approach similar phenomena, in this study, a 2D axial symmetric model is used within a numerical simulation case of an air-filled bubble is placed at the end of a narrow and long channel with a rigid side wall, as depicted in Figure 2.2.

The explanation of shockwave propagation from high-energy source at the left-side of the channel is as follows: the rectangular red region in from Figure 2.2 depicts an area of water with 3.75 GJ/kg of internal energy which then creates an incoming planar shockwave that travels to both ends. A non-reflective boundary is applied to the left-end, therefore shockwave will goes through the and the left-end will not be the area of interest. On the right-end, the incoming shock will be reflected as rarefaction wave upon in contact with air bubble and rigid side wall. The reflection from rigid side wall is an approximation of cavitation bubble clouds phenomena, where the single bubble is surrounded by nearby multiple bubbles collapsing which producing shockwaves that reflects at one another, as depicts in the illustration in Figure 3.1.

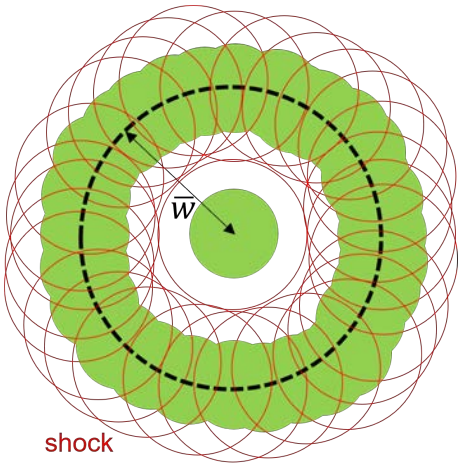

Figure 3.1: Cavitation bubble clouds illustration. The red line depicts shockwave that emerges from surrounding bubble collapse, reflecting with one another. The notation of $\bar{w}$ shows the distance between two bubbles, where also represents the radius of rigid side wall channel.

To investigate the inference of material's mechanical properties to BCILs, three different material constitutive models: elastic which only consists of consisting of only Young's Modulus E, elasto-plastic, which added the yield strength limit, and strain-hardening, will be investigated in the solid material case. The explanation will follows in the next section.

3.2.2 Solid Material Constitutive Model

There are three types of material constitutive models used for metals and polymers in coated surface case: elastic, elasto-plastic, and strain hardening. Elastic is where the strength of materials is only defined by Young's Modulus thus obeying Hooke's law, but without any yield limit included. Elasto-plastic is also defined by Young's Modulus, with a constant yield limit included. In the strain hardening model, the yielding phase is defined as non-linear. The stress-strain behavior of these models is visualized in Figure 3.2.

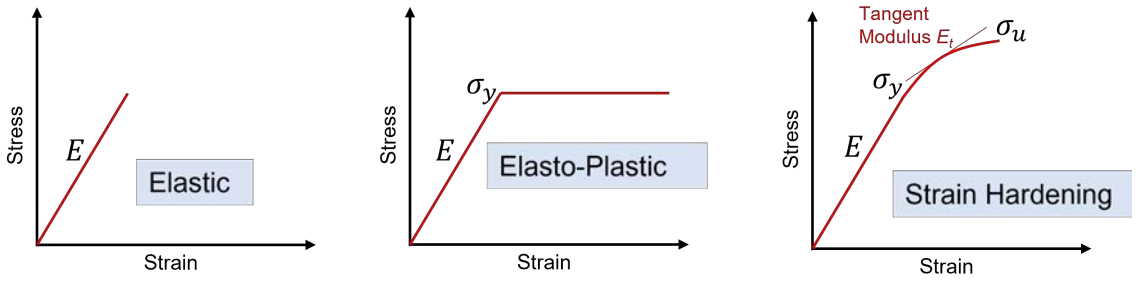

Figure 3.2: Typical stress-strain behavior for three material constitutive models.

The strain-hardening model for metal stress–strain materials was based on the

Steinberg–Guinan model, which was obtained directly from the Autodyn Material Database. For polymer materials, owing to data limitations, strain-stiffening phenomena were depicted using the bilinear hardening model. The tangent modulus E_t is expressed as a linear phase when the polymer has reached the yield strength σ_y until the ultimate strength σ_u, as follows:

$$E_t = \frac{\sigma_u - \sigma_y}{\epsilon_u - \epsilon_y} \tag{3.1}$$

where ϵ_u and ϵ_y are elongation at ultimate and yield strength, respectively. The yield and ultimate strength properties of the polymer materials were obtained from the ANSYS CES Granta EduPack 2019 software. The strength properties of all the materials used are listed in Table 3.1.

Table 3.1: Material properties of metals and polymers.

Property	SS304	Titanium	Al2024	Adiprene	Epoxy	Polyethylene
E [GPa]	196	120	69	4.17	1.03	0.8
$z_2[10^5 Ns.m^3]$	14.3	13.9	13.4	8.45	6.33	5.96
σ_y [MPa]	340	850	260	60.6	42	20
σ_u [MPa]	Steinberg-Guinan Strain-Hardening model.			75.8	69	33
ϵ_y [%]				3	20	15
ϵ_u [%]				6	85	800
$E_t[MPa]$				506.67	41.54	1.65

3.2.3 Impact Energy Analysis

The impact load $F(y,t)$ was measured by integrating the pressure obtained from the gauges installed along the y coordinates on the rigid wall and the coated surface of the material. A total of 41 gauges were installed from the axisymmetric axis ($y = 0$) to the edge of the wall ($y = 1\,\text{mm}$). The impact energy obtained was based on the energy flux across a unit area of a fixed surface normal to the pressure wave propagation direction [3.5]. The energy flux E_f, radiated by pressure and can be expressed as:

$$E_f = \frac{1}{\rho_L c_L} \int_0^\infty P^2(t)\, dt \tag{3.2}$$

where ρ_L is the water density and c_L is the speed of sound in water (taken as 1483 m/s). The pressure P_n used to calculate the energy flux was obtained from each n node at the solid's surface. The time difference dt was interpreted as the time interval Δt between each data taken, which was 0.01 µs. Therefore, to apply

Equation 3.2 in the simulation, the impact energy from one gauge E_n can be stated as:

$$E_n = \sum_{0}^{t} \frac{P_n^w \Delta t}{\rho_L c_L} \tag{3.3}$$

The total impact energy measured by summing all the gauges installed along the y-axis can be expressed as ΣE_n. This term is analogous to the cumulative impact load employed by Hattori and Hammit [3.6], ΣF_i^2 to predict cavitation damage. The impact load distribution obtained from the cavitation erosion test by Hattori et al. [3.7] for nine types of metals showed that the maximum impact load occurred at the lowest number of counts. This shows that the impact loads from bubble collapse reached a maximum value only at one time and then gradually decreased. Therefore, a new parameter called the impact energy rate of change $d(\Sigma E_n)/dt$ was calculated to select ΣE_n at the appropriate timing:

$$\frac{d(\Sigma E_n)}{dt} = \frac{\Delta E_n}{\Delta t} = \frac{E_{n2} - E_{n1}}{t_2 - t_1} \tag{3.4}$$

The time where largest value of $d(\Sigma E_n)/dt$ occurred will be selected to extract the impact energy ΣE_n. These two parameters will be used to evaluate cavitation damage in metals and polymers in the upcoming sections.

3.3 Results and Discussion

3.3.1 Bubble Collapse Mechanism Induced by Planar Shockwave

A high internal energy from water (3.57 GJ/kg), which was placed 5 mm from the end of the tube, produced a 194 MPa planar shockwave, which then propagated and interacted with a single air bubble. Figure 3.3 shows the mechanism of bubble–shockwave interaction in the rigid wall case. When the planar shock first interacts with the air bubble, it starts to shrink and forms a reflected rarefaction wave (Figure 3.3a and 3.3b). This phenomenon occurs because the acoustic impedance of air is less than that of water [3.8]. As the interaction progresses and the planar shock arrives at the rigid wall (Figure 3.3c), the bubble continues to shrink.

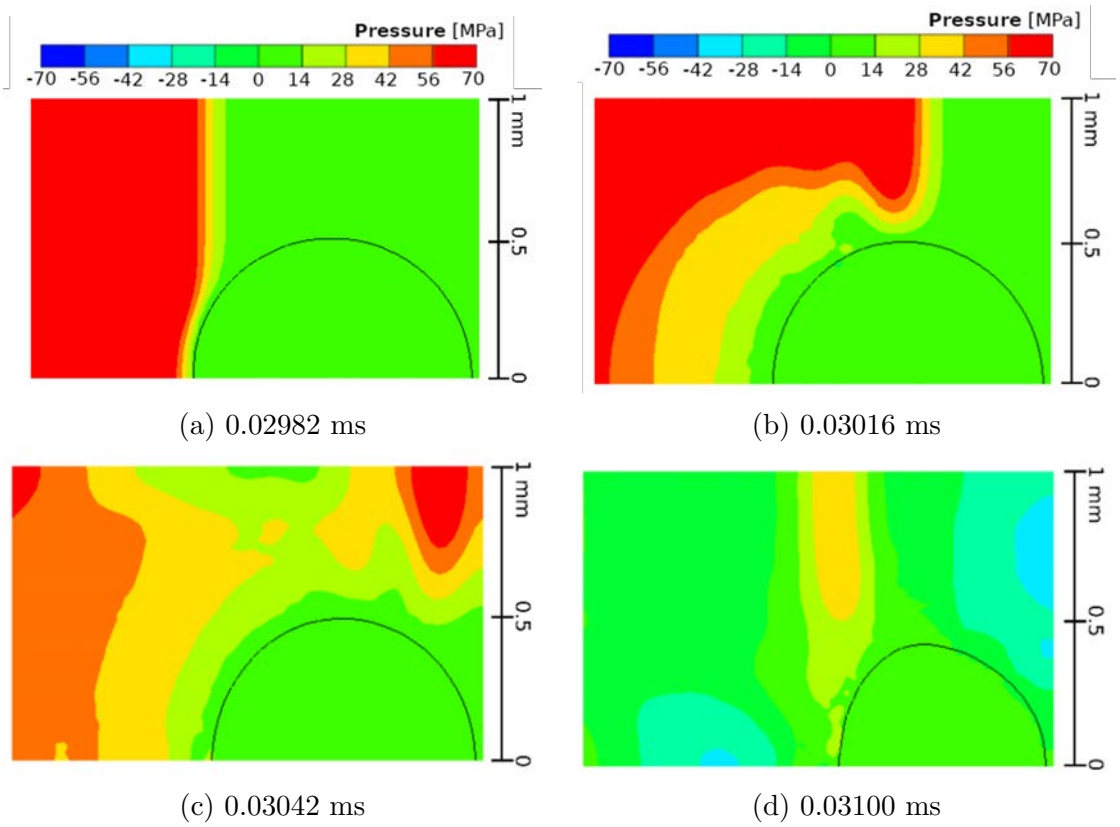

(a) 0.02982 ms

(b) 0.03016 ms

(c) 0.03042 ms

(d) 0.03100 ms

Figure 3.3: Pressure contour at several timings where planar shockwave starts to interact with single air bubble. The rigid wall is located on the upper side of the bubble.

As the shrinking progresses, a high-pressure region and curved shape form at the bottom part. The pressure and velocity profiles of several timings were selected (Figure 3.4). The high-pressure region is shown at the bottom of the curved part, while the high-velocity region occurs inside and closer to the bubble. A similar mechanism was reported by Hawker and Ventikos [3.9], where the front-tracking technique revealed that this occurs because of the reflected rarefaction wave, which causes the pressure to relax, thereby accelerating the flow. The curved shape causes this acceleration to focus the flow to a point on the upstream bubble wall, causing it to involute and form the main transverse jet. The BEM and FLM methods of pressure pulse–bubble interaction in a water medium developed by Klaseboer et al. [3.8] also reported a similar mechanism where a high-velocity region appeared at the curved part of the bubble, indicating the main transverse jet.

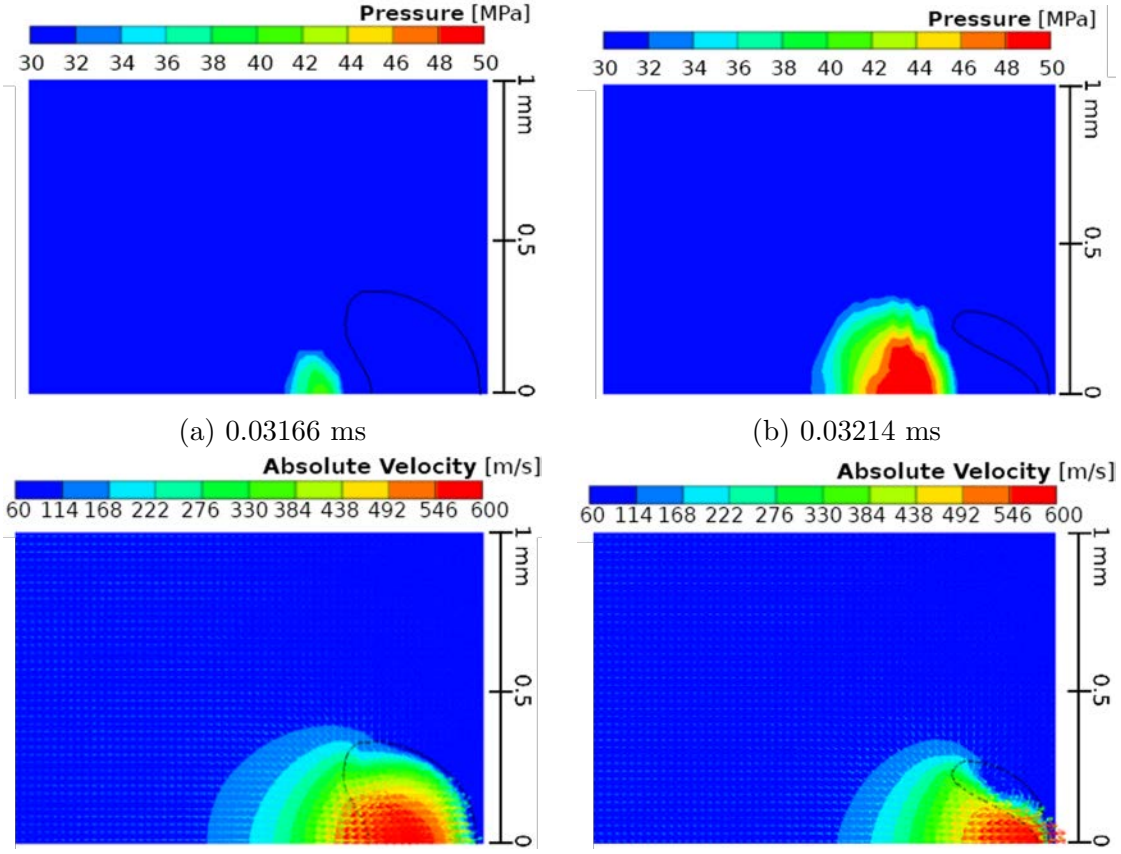

(a) 0.03166 ms (b) 0.03214 ms

(c) 0.03166 ms (d) 0.03214 ms

Figure 3.4: Jet formation shown for pressure contour (a) and (b), absolute velocity (c) and (d).

As the flow acceleration becomes more focused on the upstream bubble wall, a toroidal bubble shape occurs, and the high-pressure region impacts the rigid wall (Figure 3.5a). The absolute velocity shown in Figure 3.5c was still considerably high, but gradually decreased until the maximum impact load timing, as shown in Figure 3.5d. Conversely, the pressure at the rigid wall reached its maximum value; thus, the maximum impact load was reached (Figure 3.5b).

A similar toroidal bubble shape was also reported in a numerical model of a low-voltage spark bubble near a rigid wall in a water medium developed by Li et al. [3.10]. The toroidal bubble is followed by a highly concentrated pressure region at the rigid wall, which is due to the restriction of the rigid wall, then changes the upward vertical jet into a sideways jet. A similar sideways jet can be seen in Figure 3.5d, where a high absolute velocity emerges in the horizontal arrow direction at the maximum impact load timing.

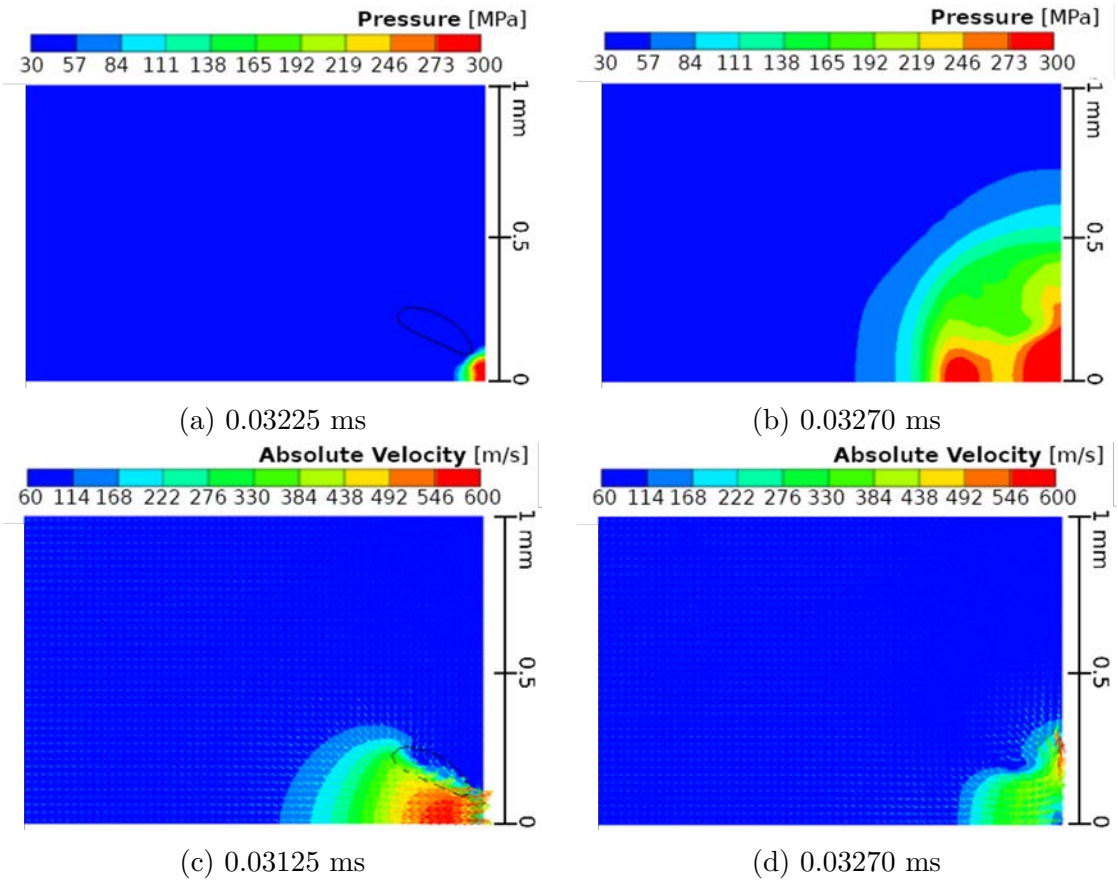

(a) 0.03225 ms

(b) 0.03270 ms

(c) 0.03125 ms

(d) 0.03270 ms

Figure 3.5: Toroidal bubble formation shown for pressure contour for (a) and (b), absolute velocity for (c) and (d).

Another important aspect that must be considered is the impact force, which is calculated based on the integral of the pressure value obtained from the gauges installed. This integration is a function of the y coordinates ranging from 0 to 1 mm. A planar shockwave of 194 MPa has a main role in inducing the collapse of air bubbles. However, this planar shockwave also arrives at a rigid wall, which affects the impact force measurement on the rigid wall. Therefore, a separate simulation with similar settings without air bubbles (shock-only case; Figure 2.2c) was conducted to analyze the effect of this planar shock on the impact force at the rigid wall measurement.

Figure 3.6 shows impact force integration from pressure on each gauge installed at y mm from axisymmetric axis, for the rigid wall case and shock-only case. For the shock-only case, maximum impact loads for all y mm reach maximum at 0.03049 ms, which indicates the timing when planar shock arrives at rigid wall. At similar timing, for the rigid wall case, a small peak that is significantly lower than that of the shock-only case occurs at $y = 1$ mm and 0.5 mm. This result indicates that impact by planar shock is significantly reduced by bubble presence. On the other hand, negative impact force value occurs around 0.031 – 0.0315 ms, which occurs

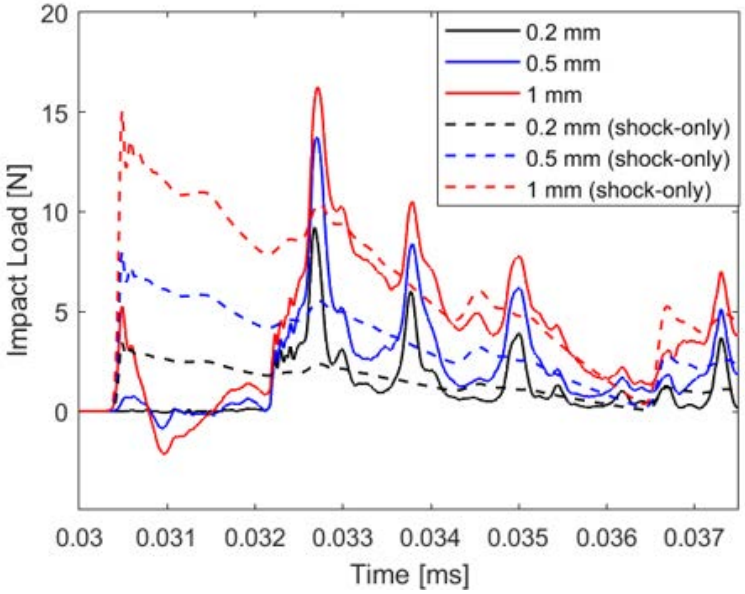

Figure 3.6: Impact load for the rigid wall case and shock-only case with several integrations of y mm.

because of reflected rarefaction wave as discussed previously. However, at $y = 0.2$ mm, neither a peak nor a reflected rarefaction wave is visible at least after 0.032 ms. This indicates that the planar shock has no significant effect on the rigid wall if the impact force is integrated until $y = 0.2$ mm. Therefore, integration until $y = 0.2$ mm will be used for further simulation with another type of solid surfaces.

Previous discussions involving several studies, both from numerical techniques and experiments, have demonstrated that the bubble collapse mechanism developed in this study is typical. Moreover, within numerical simulations, the physical quantity of the phenomena such as pressure, stress, and strain can be arbitrary extracted, hence offers a more detailed analysis that might be difficult to achieve through experiment. Therefore, the numerical scheme will be utilized and explored to predict cavitation damage by single bubbles on several types of solid surfaces with various material constitutive models.

3.3.2 Bubble Shock-Induced Collapse Near Al2024

In the results of Al2024 coated surface case, the reflected rarefaction wave, as in the rigid wall case, appeared as well. However, the reflected wave seems weaker, with similar timing, than in the rigid wall case as shown in Figure 3.3. Similar phenomena of weaker rarefaction wave on Aluminum boundary wall was is found in the numerical study of shock-induced single bubble collapse attached to Aluminum wall [3.11]. This is due to the difference of acoustic impedance in the material, whereas rigid is assumed to possess infinite value. Moreover, a lower pressure region

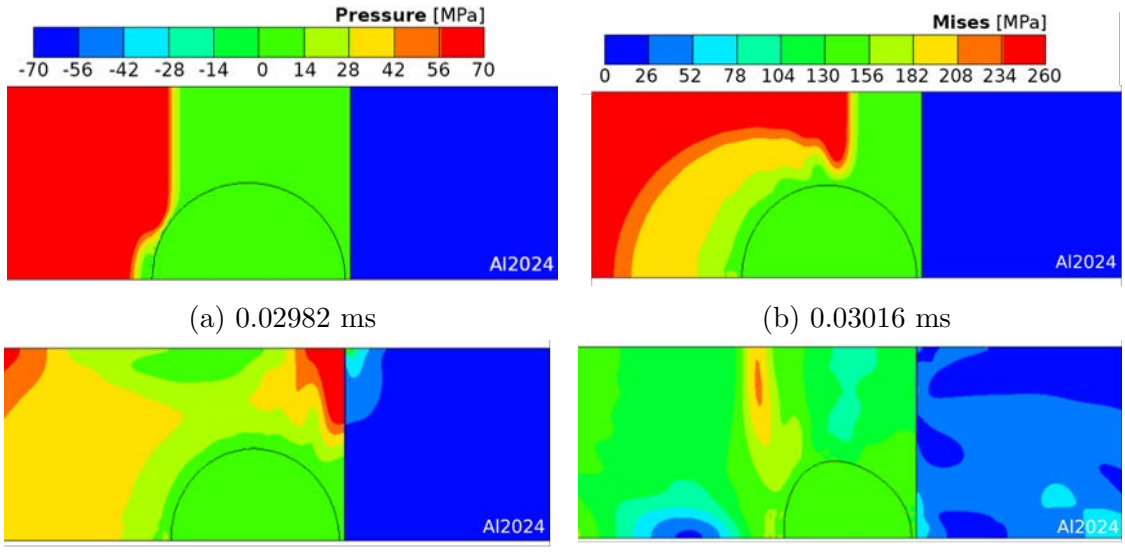

(a) 0.02982 ms

(b) 0.03016 ms

(c) 0.03042 ms

(d) 0.03100 ms

Figure 3.7: Single air bubble with planar shockwave interaction near Al2024 with elasto-plastic constitutive model. Fluid area is shown in Pressure contour and Al2024 area is shown in von Mises stress contour.

(Figure 3.7d) is seen in the area around the bubble. The von Mises stress profile mapped on the Al2024 material part shows that in this bubble–shock interaction phase, Al2024 has not reached its yield limit. Bubble shrinking and jet formation mechanisms also occurred in the Al2024 wall case. Figure 3.8 shows the mechanism steps in comparison with the rigid wall case shown in Figure 3.3. The high-pressure region formed at the curved part in Figure 3.8a and 3.8c is larger than that in the rigid wall case. Conversely, a negative pressure region occurred because of the heavy reflection of the planar shock on the edge of the tube at the earlier phase, causing the water to move slightly downward, as shown in Figure 3.8c and 3.8d. However, this slight water movement appeared to exist at $y > 0.4$ mm; thus, it will not affect further impact load and energy analysis because the integration will be taken at $y = 0.2$ mm.

The high absolute velocity region facing upward (Figure 3.8d) indicates the main transverse jet. The bubble deformation shape in this jet formation stage appeared to be smaller and more skewed than that in the rigid wall case. On the Al2024 side, the von Mises stress response can be seen on the Al2024 profile contour; however, it is still far from the yield limit, because the jet has not reached the wall surface.

Analogous to the rigid wall case, the following jet formation phase is a toroidal bubble shape (Figure 3.9a). This phase indicates that the main transverse jet reaches the Al2024 wall, and the von Mises stress profile contour shows a concentrated rise above the yield limit on the area around the axisymmetric axis ($y = 0$ mm). However, the previous concentrated area exceeding the yield limit appears to grow

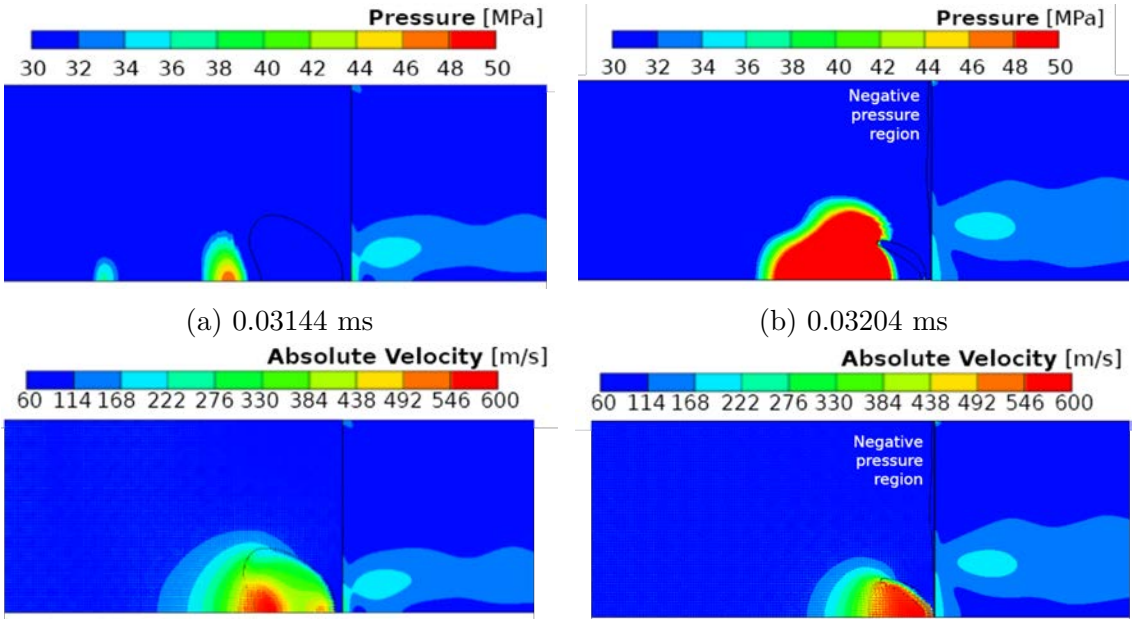

(a) 0.03144 ms (b) 0.03204 ms

(c) 0.03144 ms (d) 0.03204 ms

Figure 3.8: Jet formation shown for pressure (a) and (b), absolute velocity for (c) and (d). Von Mises Stress contour is similar to that in Figure 3.3.

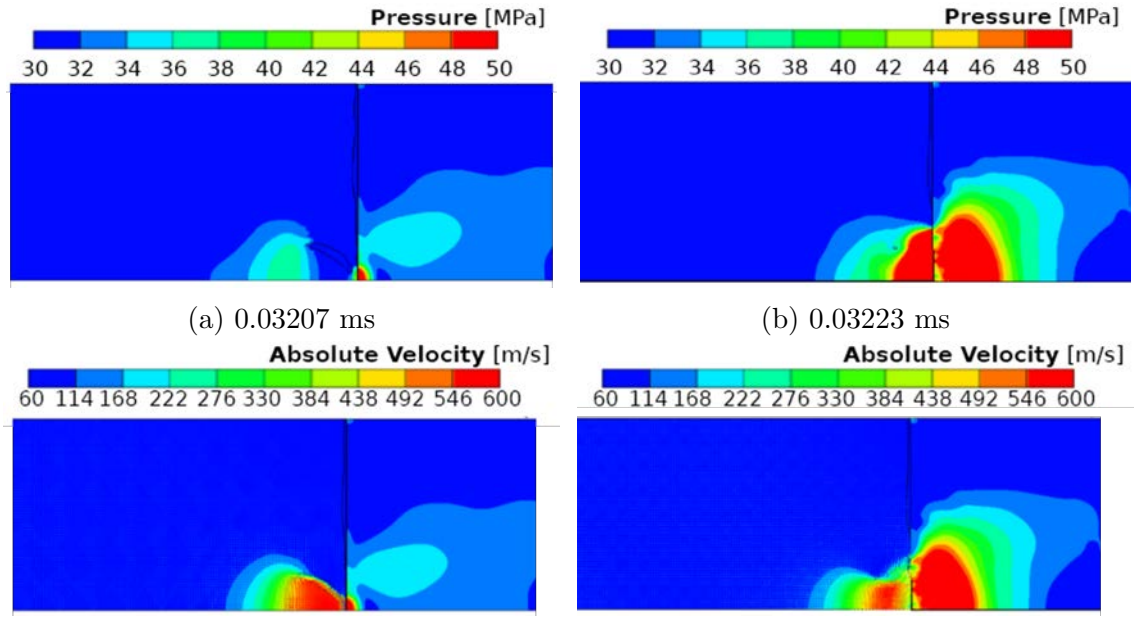

(a) 0.03207 ms (b) 0.03223 ms

(c) 0.03207 ms (d) 0.03223 ms

Figure 3.9: The profile contour (a) and (b), and abosulte velocity (c) and (d) at toroidal bubble formation timing. Profile contour on Al2024 is von Mises stress with a similar scale as that in 3.3.

larger as shown at maximum impact load timing, following the formation of the high-pressure region (Figure 3.9c). Conversely, the absolute velocity gradually (Figure 3.9d) becomes slower as the jet starts to develop in the sideways direction. Compared to the rigid case, the toroidal bubble phase formed 0.18 µs earlier. The maximum

impact load timing also occurred 0.47 µs earlier. The difference in bubble collapse and jet impact timing between rigid and aluminum walls was also found in [3.11]. For attached bubble case with $\gamma = 0.95$, jet impact for rigid wall case occurred 0.02 µs earlier than in aluminum wall. However, there is no direct comparison of bubble collapse timing between rigid and aluminum for the detached bubble case, which would be more beneficial for this discussion. Such a discussion that analyzes bubble frequencies near various solid materials must be conducted to explore the reason behind these collapse-timing differences. For the time being, the numerical simulation conducted in this research found that wall properties affect the bubble collapse mechanism in terms of timing, shape, pressure on the fluid area, and stresses at the wall. Further discussion will be focused on how to utilize this numerical model to predict cavitation damage on several types of materials.

3.3.3 Damage of Single Bubble Shock-Induced Collapse near Al2024

In this study, a parameter analogous to the cumulative impact energy ΣF_i^2 was derived directly from the original principle, as introduced in Section 3.2.3. Based on the previous discussion on the planar shock effect on a rigid wall, the impact energy ΣE_n was integrated until $y = 0.2$ mm. Therefore, the value of Impact Energy ΣE_n its rate of change $d(\Sigma E_n)/dt$ for Al2024 are analyzed.

Figure 3.10 shows values of ΣE_n and its rate of change from 0.03 to 0.0375 ms. Note that from 0 to 0.03 ms, planar shock is still propagating from tube's open end and has not arrived at single air bubble; thus, no signal is shown on the wall. The highest peak of $d(\Sigma E_n)/dt$ at 0.03223 ms coincides with the maximum impact load timing shown in Figure 3.5c and 3.5d. This shows that the energy changes drastically at that timing. It is a common conception in fracture mechanics that drastic energy jumps in a short time plays significant role in material failure. Therefore, the highest peak of $d(\Sigma E_n)/dt$ will be used to determine the timing at which ΣE_n value is to be selected. The effect of this impact energy on several material types is discussed in Section 3.3.4.

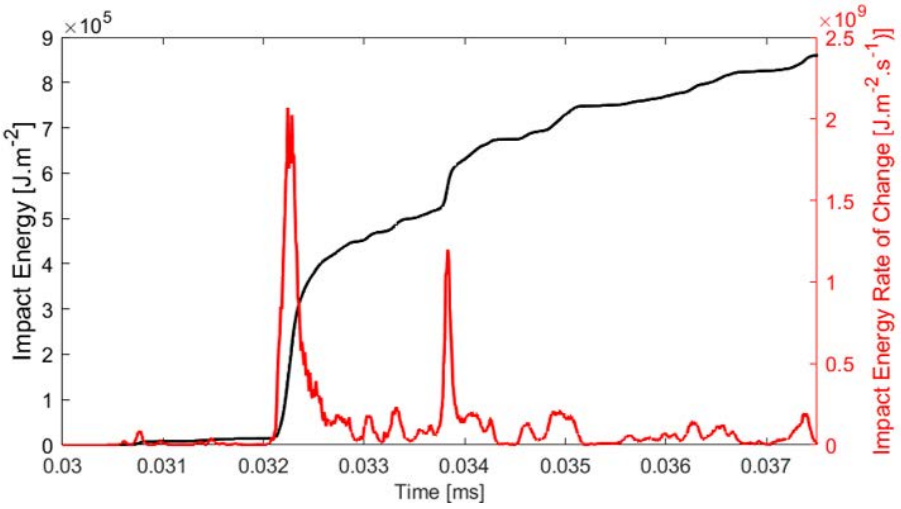

Figure 3.10: Impact energy ΣE_n and impact energy rate of change $d(\Sigma E_n)/dt$ of elasto-plastic Al2024 at $y = 0.2$ mm integration.

The linear cumulative damage rule uses a double logarithmic scale of the S-N curve to predict the fatigue life. However, owing to difficulties in estimating the impacted area in the cavitation erosion test, Hattori et al. [3.12] analyzed the F-N curve instead. On the other hand, a recent study by Joshi et al. [3.13] on the numerical analysis of shock-induced collapse bubbles near the aluminum wall concluded that the magnitude of plastic strain on the aluminum wall is over-predicted when compared with another elasto-plastic model shown by other studies [3.11, 14]. A similar tendency was observed in the effective plastic strain results of the elastic, elasto-plastic, and strain-hardening models of Al2024 (Figure 3.11). The plastic strain of the elasto-plastic model is over-predicted compared to the strain-hardening model, while the elastic model shows zero plastic strain owing to the absence of the yield stress limit. Consequently, the von Mises stress results of the elastic model are over-predicted, whereas the elasto-plastic model does not surpass its 260 MPa yield stress limit.

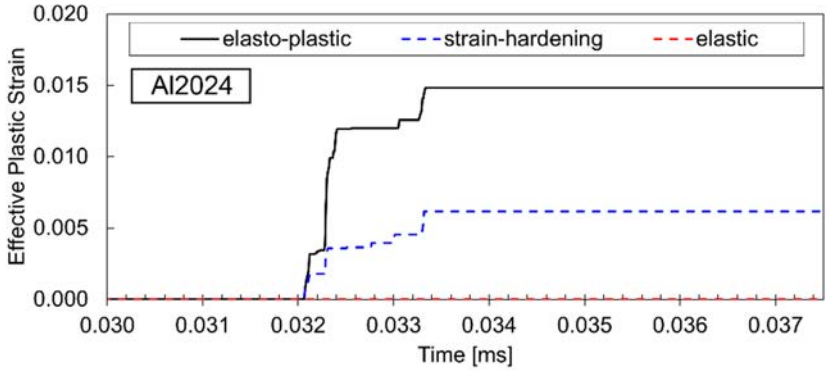

(a) Effective plastic strain of Al2024.

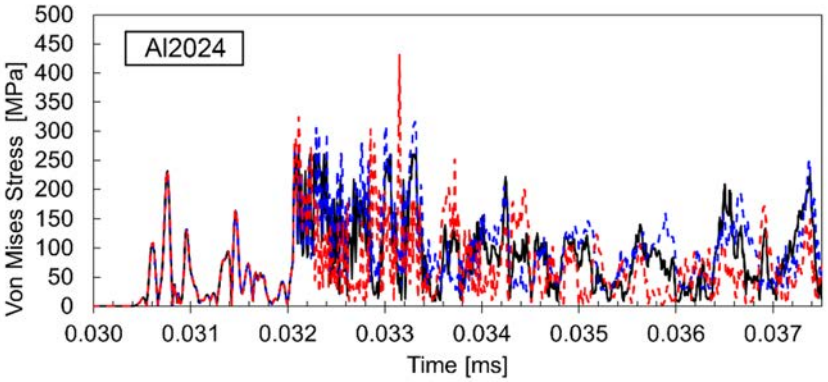

(b) Von Mises stress of Al2024

Figure 3.11: Effective plastic strain and von Mises stress for several material constitutive models of Al2024 at $y = 0$ mm. Yield stress limit for Al2024 is 260 MPa.

Another type of metal material, titanium and stainless steel 304 (SS304), were evaluated under simulation conditions similar to those of Al2024. The plastic strain and von Mises stress history are shown in Figure 3.12. For SS304, a similar mechanism was observed for Al2024. The plastic strain for the elasto-plastic model was over-predicted compared with the strain-hardening model. The von Mises stress result for the elasto-plastic model never exceeds its yield stress limit, which is 340 MPa. However, for titanium, the BCIL did not exceed its yield limit of 850 MPa. Thus, no plastic deformation occurs, and the von Mises stress for all the constitutive models is coincidental.

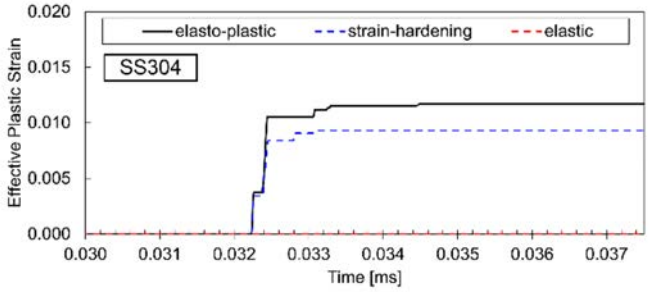

(a) Effective plastic strain of SS304.

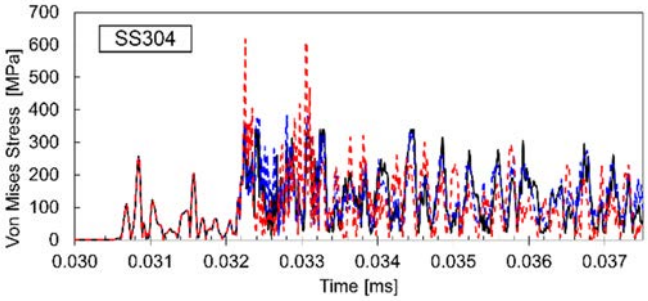

(b) Von Mises stress of SS304.

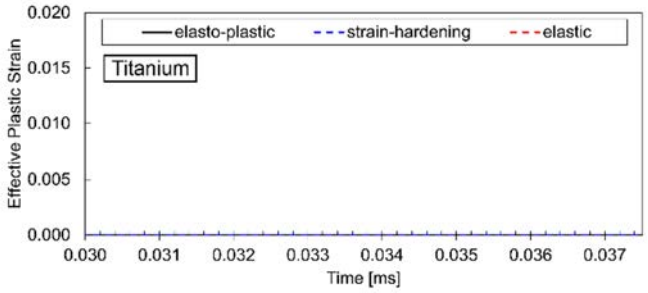

(c) Effective plastic strain of Ti.

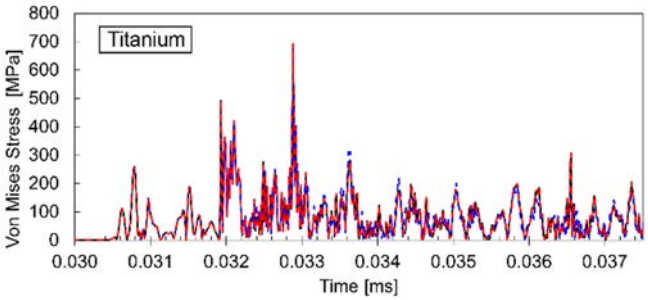

(d) Von Mises stress of Ti.

Figure 3.12: Effective plastic strain and von Mises stress for several material constitutive models of SS304 and titanium at $y = 0$ mm. Yield stress limit is 340 MPa for SS304 and 850 MPa for titanium.

The above discussion indicates that the material constitutive model developed in this study works well and behaves as expected. Furthermore, it indicates that the strain rate effects and yield stress limit on the material constitutive model play important roles in the stress distribution on the wall owing to the BCIL. On that account, further analysis will be carried out on impact loads and impact energy

variations for metals as well as polymer materials.

3.3.4 Plasticity Effects on Metals and Polymers

To investigate the plasticity effects which is shown by changing material constitutive model on solid surface deformation due to single bubble collapse, the plastic strain of Al2024 and epoxy material during three different timings is described in detail. As shown in Figure 3.8, in the toroidal bubble formation phase, there is no significant difference in terms of fluid pressure. Plastic deformation does not occur in the elastic, elasto-plastic, and strain-hardening models of Al2024. However, different phenomena were observed at the first peak of the impact energy rate of change, $d(\Sigma E_n)/dt$. The highest plastic deformation at this phase occurred in the elasto-plastic model; plastic deformation still occurred in the strain-hardening model, but the value was lower. Because no yield stress limit is incorporated in the elastic model, plastic deformation did not occur in this model. Similar phenomena were also observed at the last time, t = 0.03750 ms, where the most severe deformation occurred in the elasto-plastic model.

Another phenomenon observed from this simulation is that the timing of the first peak of $d(\Sigma E_n)/dt$ differs depending on the material constitutive model. As described in the previous section, this timing indicates the highest jump in the impact energy calculation, which contributes to the failure mechanism of the material. Figure 3.13 shows that the first peak timing for the elasto-plastic model occurred earlier, at 0.03224 ms. In the strain-hardening model, it occurred at 0.03226 ms and in the elastic model at t = 0.03227 ms. This result indicates that the material constitutive model affects not only the plastic strain or deformation of the solid surface, but also the bubble collapse mechanism. The stiffer the boundary, the longer it takes to reach the highest impact energy jump, which may likely contribute to failure.

Figure 3.14 shows the bubble collapse mechanism and solid surface deformation of the epoxy material. Similar phenomena as in the Al2024 case regarding the first peak of $d(\Sigma E_n)/dt$ timing is observed, whereas in the elasto-plastic model, it occurs at the earliest time compared to another constitutive model. However, different phenomena are observed for the plastic deformation. In the elastic model, deformation occurred at the first peak of $d(\Sigma E_n)/dt$ (t = 0.03252 ms). However, it went back later at t = 0.03750 ms, as the plastic strain remained zero; thus, no permanent deformation occurred. In the elasto-plastic and strain-hardening models, plastic strain occurred at the first peak of $d(\Sigma E_n)/dt$ timing and formed a spherical shape deformation known as the cavitation pit.

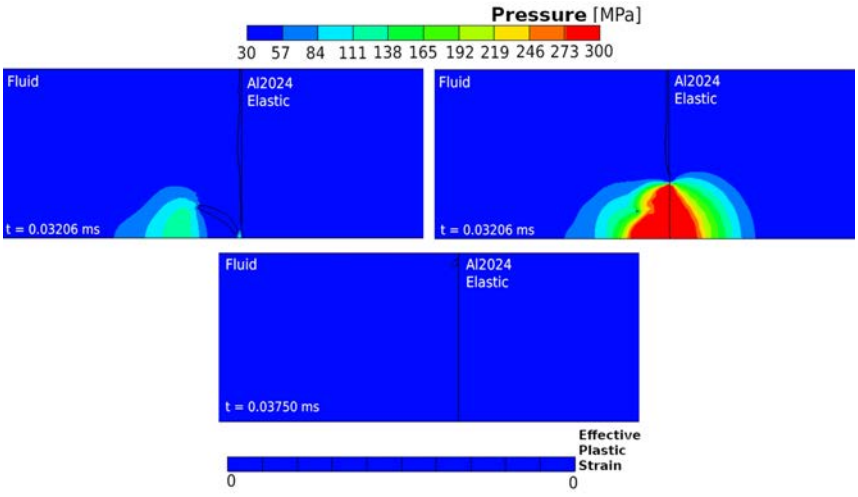

(a) Al2024 elastic.

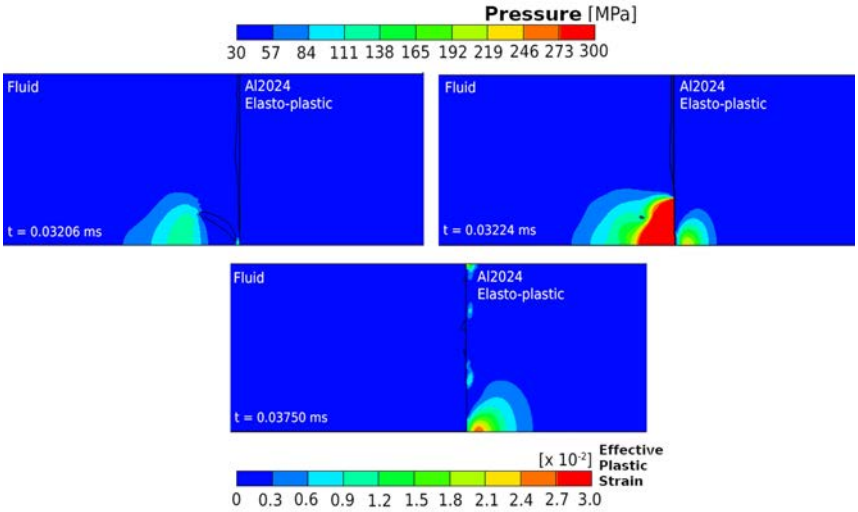

(b) Al2024 elasto-perfectly plastic.

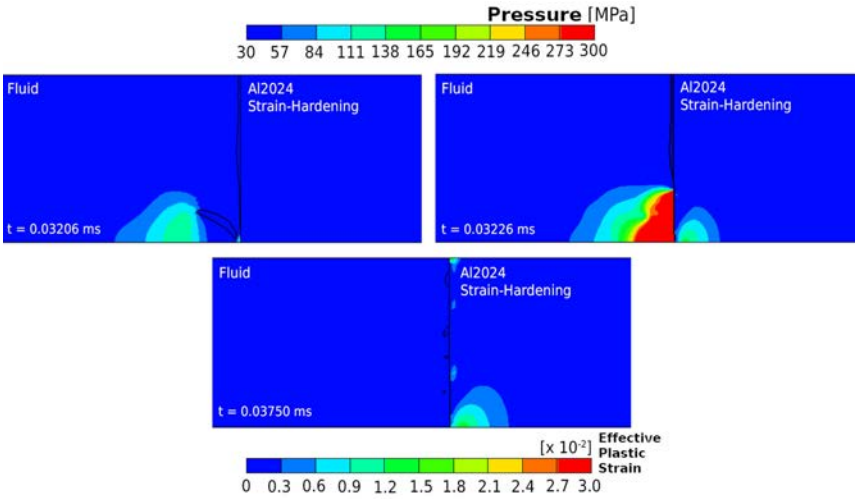

(c) Al2024 strain-hardening.

Figure 3.13: Deformation and plastic strain of Al2024 on three different timings: toroidal bubble formation (upper left) and the first peak of $d(\Sigma E_n)/dt$ (upper right) and at the end of simulation time (bottom).

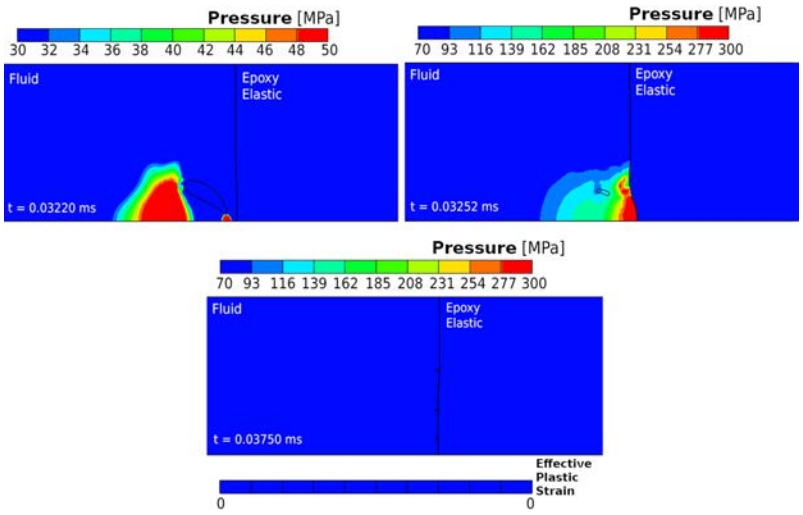

(a) Epoxy elastic.

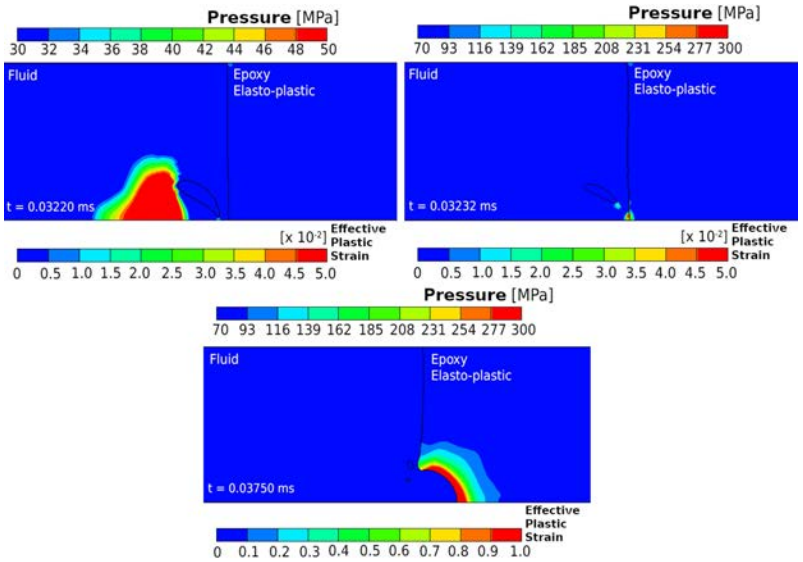

(b) Epoxy elasto-perfectly plastic.

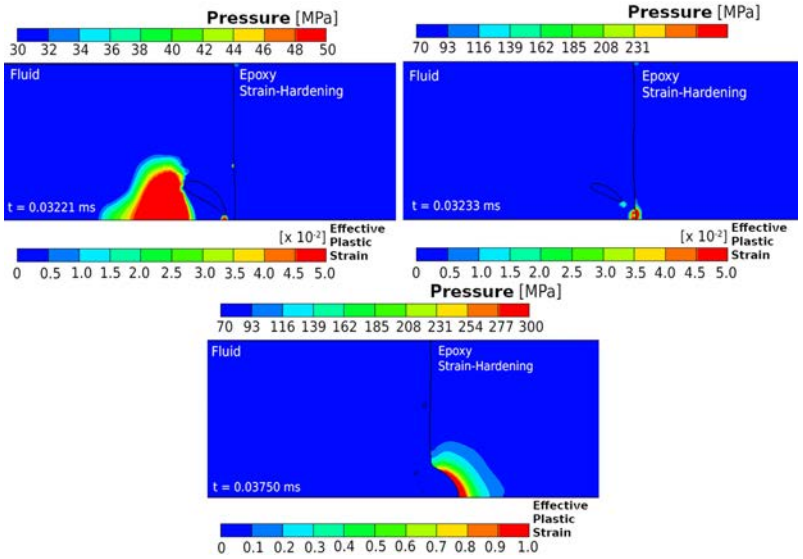

(c) Epoxy strain-hardening.

Figure 3.14: Deformation and plastic strain of Epoxy on three different timings: toroidal bubble formation (upper left) and the first peak of $d(\Sigma E_n)/dt$ (upper right) and at the end of simulation time (bottom).

The above simulation results show that material constitutive models affect the bubble collapse mechanism and deformation on the solid surface. The deformation behavior also varies between metal and polymer materials. This indicates that there are different failure mechanisms between metal and polymer materials when subjected to cavitation bubble collapse loads. Therefore, to confirm this phenomenon, the maximum impact load integrated from y = 0 mm (axisymmetric line) to $y = 2$ mm on the solid surface was compared with the maximum impact load obtained from the cavitation erosion test by [3.3]. Figure 22 shows the relationship between the maximum impact load and acoustic impedance z, which is calculated from

$$z = \frac{1}{(1/z_1) + (1/z_2)} \tag{3.5}$$

z_1: acoustic impedance of water ($c_L \rho_L$).
c_L: sound velocity in water (1483 m/s).
ρ_L: liquid density ($1000\,\mathrm{kg\,m^{-3}}$).
z_2: acoustic impedance of solid material ($c\rho$).
c: sound velocity inside material.
ρ: solid material density.

When viewed in detail, the maximum impact load value shows different behaviors depending on the material constitutive model. For example, there is no plastic strain on the titanium material surface; therefore, the maximum impact load values for all the constitutive models were similar. For adiprene, the difference between elasto-plastic or strain hardening and the elastic model did not increase as much as in epoxy and PE. However, when viewed roughly, a linear trend line can be used to estimate the relationship between the maximum impact load and acoustic impedance z. In Figure 3.15, these lines are shown in black for elasto-plastic, blue for strain-hardening, and red for elastic models. There is an approximately two-fold increase in the maximum impact load from the polymer to metal materials. A similar trend was observed in the maximum impact load results from the cavitation erosion test conducted by Hattori and Itoh [3.3], shown as a purple line based on four types of polymer materials (epoxy, polypropylene, high-density polyethylene, and polyamide 66) and two types of metal materials (pure aluminum and low-carbon steel). Moreover, the maximum impact load results between epoxy and PE for elasto-plastic and strain-hardening from this simulation coincide with those from the cavitation erosion test.

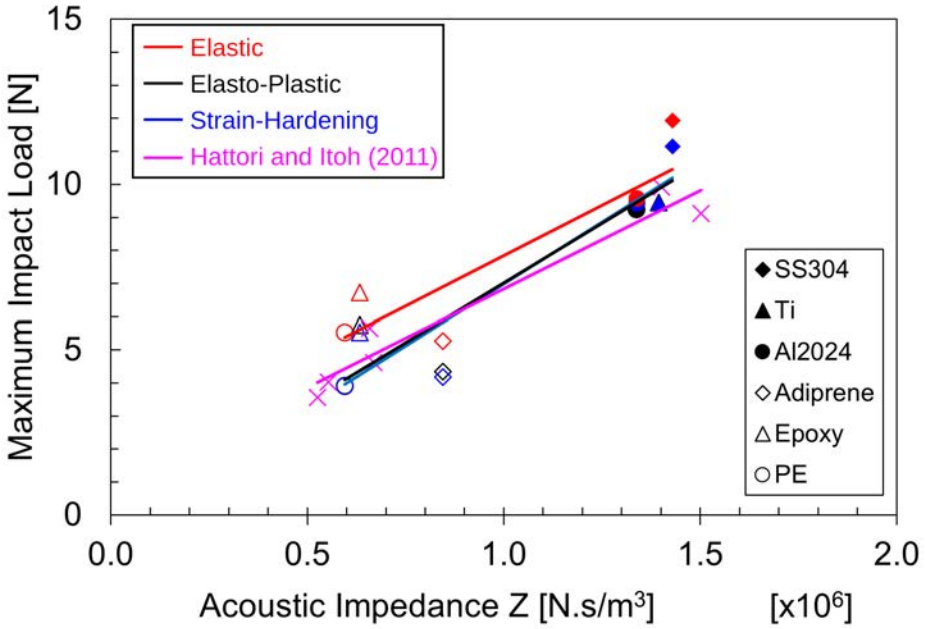

Figure 3.15: Maximum impact loads measured by integration from center to $y = 0.2$ mm for three material constitutive models shows good agreement with cavitation erosion test results by Hattori and Itoh [3.3].

Although the material types considered by Hattori and Itoh [3.3] are not identical to those in our simulation, the results for the elasto-plastic and strain-hardening models shown in Figure 3.15 show that our numerical model comprising single bubble shock-induced collapse is highly comparable with the cavitation erosion test results. This is because the cavitation erosion test used a microsecond order-sampling interval on the pressure sensor. This detailed calibration made the probability of measuring several impact loads from multiple bubbles very small [3.7]. Therefore, the maximum impact loads originated from a single cavitation bubble collapse.

Another insight that is found by analyzing the maximum impact load and acoustic impedance z is that, for the elastic model, the trend is generally increasing compared with elasto-plastic and strain-hardening. This indicates that the yield stress limit σ_y on the material properties contributes to the failure mechanism due to cavitation bubble collapse. Therefore, the relationship between the impact energy ΣE_n and acoustic impedance z within three different material constitutive models will be further analyzed.

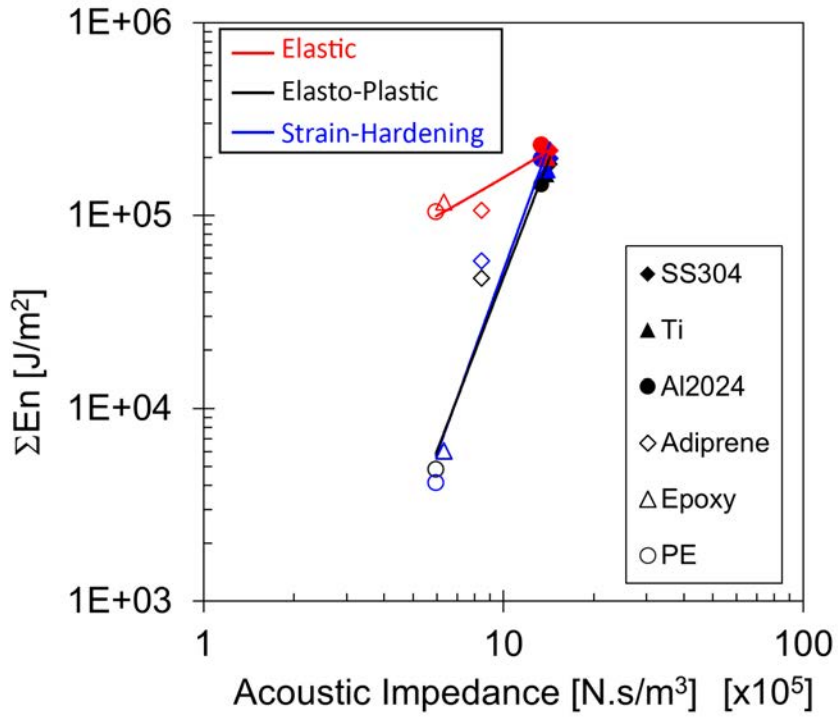

Figure 3.16: Impact energy ΣE_n to acoustic impedance for elastic, elasto-plastic, and strain-hardening model. Impact energy integration was done until $y = 0.2$ mm and timing selection was at the highest peak of impact energy rate of change $d(\Sigma E_n)/dt$.

Figure 3.16 shows that the impact energy of metal and polymer materials calculated from numerical simulation is gradually increasing based on acoustic impedance z for all material constitutive models. The trend line shows that there is no significant difference between elasto-plastic and strain-hardening model. However, there is a discrepancy on gradient of the trend line for elastic model. There is around 20 to 25 times increase in impact energy of elastic model for PE and epoxy, while for Ti, Al2024, and SS304, no significant difference was found if material properties were changed. This indicates that our simulation can reveal distinct cavitation damage mechanism between metals and polymers, which could not be distinguished earlier through experimental test results.

Impact energy analysis on metal materials (Ti, Al2024, and SS304) from Figure 3.16 showed that there was no significant difference if the material constitutive models were changed. This mechanism might be expected if the impact load originating from a single bubble collapse did not exceed the yield limit for all the constitutive models. However, the plastic strain history shows that for the elasto-plastic and strain hardening models of SS304 (Figure 3.12a) and Al2024 (Figure 3.11), the impact load reached the yield phase; thus, plastic deformation occurred. On the other hand, for titanium (Figure 3.12c), plastic strain is non-existent for all constitutive models because the impact load does not surpass its yield limit. This indicates

that for metal materials, elastic energy is the only parameter that drives cavitation damage. Consequently, cavitation pits are formed only after multiple loadings occur from bubble collapse. Therefore, the cavitation damage of metal materials is influenced by fatigue.

The interpretation that cavitation damage on metals is driven by fatigue has been proven by other findings through experimental methods. An earlier study by Richman and McNaughton [3.15] found good correlations between the material removal rates and cyclic deformation parameters, including the fatigue strength coefficient and cyclic strain resistance. The prediction method was based on the incubation time, from the cavitation erosion test results of 23 types of pure metals and alloys. Moreover, scanning electron microscopy (SEM) results of Hattori et al. [3.7] from eroded specimens of Al, Cu, and steel alloys also indicate fatigue fractures.

In order to explore more in the possibility of predicting cavitation damage due to single BCIL, a parameter called apparent acoustic impedance Z' is introduced. From the impact energy and acoustic impedance relationship shown in Figure 3.16, the main significance is the decrease of ΣE_n between elastic models with elasto-plastic and strain-hardening models only on polymers. The Z' were extracted by extending the elastic line to the point of ΣE_n values of the polymers on each elasto-plastic and strain-hardening model. The Z' values are shown as cross sign in Figure 3.17.

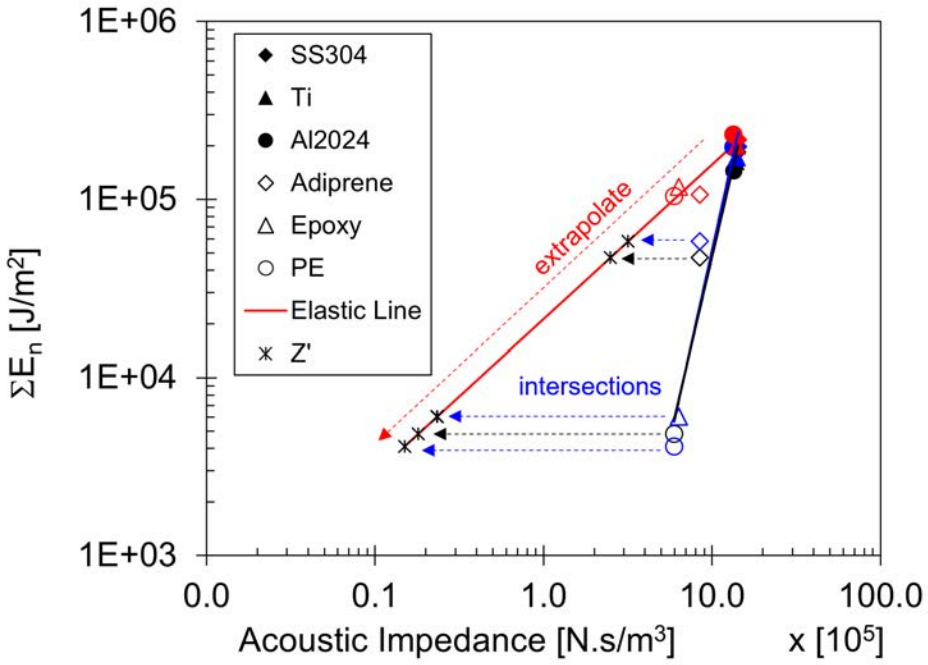

Figure 3.17: Extension of elastic line (red) to obtain apparent acoustic impedance Z' of adiprene, epoxy, and PE for elasto-plastic and strain-hardening model.

Note the the Z' values in here still have an influence of acoustic impedance of water z_1. Therefore, to obtain material's apparent acoustic impedance z_2', an

Table 3.2: Discrepancy constant a between apparent Young's Modulus E' and original material data Young's Modulus E and discrepancy constant b between E and tangent modulus E_t from material data.

Material	$\boldsymbol{a} = E'/E$		$\boldsymbol{b} = E_t/E$
	Elasto-plastic	Strain-hardening	
Adiprene	0.0232	0.0422	0.1215
Epoxy	0.0005	0.0005	0.0403
Polyethylene	0.0003	0.0002	0.0021

inversion of Equation 3.6 was used in the form of

$$z_2' = \frac{1}{(1/Z') - (1/z_1)} \tag{3.6}$$

Then, by simply relating to material's density, the apparent Young's Modulus E' can be obtained by:

$$E' = z_2'^2/\rho \tag{3.7}$$

From physical standpoint, the apparent Young's Modulus E' is an estimation of how much decreased in elasticity due to the presence of yielding, extrapolated from the elastic line of numerical simulation results. Therefore, a comparison was done between the original elasticity values, which is the Young's Modulus E for each polymer. The ratio between E' and E is stated as constant a. Another comparison is also done to compare this "decreased elasticity" to the plastic phase, which represented by original tangent modulus E_t for each polymer. The ratio between E' and E_t is shown as constant b. All parameters obtained are stated in Table 3.2.

From Table 3.2, the discrepancy of Young's modulus E due to yield and strain-hardening is larger for epoxy and polyethylene than for adiprene. For adiprene, the yield effects decrease the Young's modulus E by approximately 40 times for the elasto-plastic model and 20 times for strain-hardening. For epoxy, both elasto-plastic and strain-hardening decreased by a factor of 2000. In the polyethylene case, the decrease is approximately 3000 times for the elasto-plastic model, while for the strain-hardening model it is almost 4000 times. However, the general trend of constant a for all materal models is decreasing. This indicates that failure due to single BCIL of polymers is most likely to be influenced by yielding. Therefore, plastic deformation must be taken into consideration when utilizing polymers for the cavitation coating material.

In Table 3.2, the constant b shows discrepancy in Young's modulus E of the polymer after it reaches the yield phase and goes into the strain-hardening effect represented by the tangent modulus E_t. It is shown that for all polymers in both

constitutive models, constant a is lower than constant b. This discrepancy is most likely caused by the approximation of E_t given by equation 3.1. Moreover, the strain obtained from numerical simulation is larger than ultimate elongation, which made the value to be over-estimated. Additional data of materials in the middle area to the lower area of acoustic impedance is needed to find a noticeable pattern which can be used to develop a phenomenological model that can be used to predict cavitation damage. If that has been established, a more sophisticated simulation with fluid viscosity incorporated inside the numerical solver can be conducted to analyze the effect of wall shear stress in cavitation erosion.

3.4 Summary

In this chapter, a numerical model of an air bubble placed near metals and polymers with standoff distance $\gamma = 1.06$ inside long and narrow channels with width $\bar{w} = 1\,\text{mm}$ are analyzed. The bubble was induced to collapse by planar shockwave that emerged from an area of water with internal energy e of 3.75 GJ/kg. Similar grid size obtained from Section 2.3 was used to ensure solution's consistency. The solid material thickness is 5 mm. To analyze the effect of plasticity, three different material constitutive models were employed: purely elastic, elasto-plastic, and strain-hardening. Bubble collapse impact load (BCIL) acting on the solid's surface and impact energy ΣE_n analogous to cumulative impact energy ΣF_i^2 estimated by Hattori and Itoh [3.3] were compared for all cases.

The collapse mechanism of shock-induced bubble near rigid wall was found to be qualitatively comparable with results found in another numerical studies [3.8, 9, 16]. The comparison of BCIL between with bubble case and planar shockwave only case was done. It is shown that the planar shockwave has no significant effect on the rigid wall when the integration of impact load was until $y = 0.2$ mm. Therefore, integration of impact loads until $y = 0.2$ mm was selected. The maximum BCIL obtained from the integration of pressure at the solid surface for the elasto-plastic and strain-hardening models were shown to be highly comparable with the experimental results of Hattori and Itoh [3.3]. This indicates that the numerical model of long channel with rigid side-edge wall can represent the collapse of bubble clouds, which often observed in cavitation test results.

The effect of different material constitutive models to bubble collapse mechanism was discussed. It is found that the acoustic impedance of the boundary wall affects bubble collapse mechanism. This is shown in the discussion of the rigid and elastic wall cases. In the elastic wall case, the acoustic impedance is lower than rigid, thus affecting the wave reflection mechanism, which results in different collapse timings, toroidal bubble shapes, and pressure distributions on both the fluid area and at the

wall.

The impact energy ΣE_n analysis for metals and polymers with different material constitutive models shows interesting results. For metals, it is shown to have no significant difference if the material constitutive models are changed into elastic, elasto-plastic, or strain-hardening. This indicates that failure due to a single bubble collapse load for metals is driven only by elastic energy. However, more evidence needed to support this argument. For polymer materials, large discrepancies were found in the impact energy values for the elastic model. Further analysis of discrepancies between apparent Young's Modulus E' and tangent Modulus E_t from material data indicated that failure due to single bubble collapse load for polymers is most likely influenced by yield. More data of polymers and another method is needed that can be quantified and examined by its relationship with yield strength.

References

[3.1] N. S. Govinda Rao and A. Thiruvengadam. Prediction of Cavitation Damage. *Transactions of the American Society of Civil Engineers*, 127(1):309–334, jan 1962.

[3.2] Frederick G. Hammitt. Cavitation Erosion: the State of the Art and Predicting Capability., 1979.

[3.3] Shuji Hattori and Takamoto Itoh. Cavitation erosion resistance of plastics. *Wear*, 271(7-8):1103–1108, 2011.

[3.4] Pedro A. Quinto-Su and Keita Ando. Nucleating bubble clouds with a pair of laser-induced shocks and bubbles. *Journal of Fluid Mechanics*, 733:1–12, 2013.

[3.5] Robert H. Cole, Royal Weller, Robert H. Cole, and Royal Weller. Underwater Explosions. *PhT*, 1(6):35, oct 1948.

[3.6] Shuji Hattori, Bong Hwa Sun, Frederick G. Hammitt, and Tsunenori Okada. An application of bubble collapse pulse height spectra to venturi cavitation erosion of 1100-o aluminum. *Wear*, 103(2):119–131, 1985.

[3.7] Shuji Hattori, Hiroyuki Mori, and Tsunenori Okada. Quantitative evaluation of cavitation erosion. *Journal of Fluids Engineering, Transactions of the ASME*, 120(1):179–185, 1998.

[3.8] Evert Klaseboer, Cary Turangan, Siew Wan Fong, Tie Gang Liu, Kin Chew Hung, and Boo Cheong Khoo. Simulations of pressure pulse-bubble interaction using boundary element method. *Computer Methods in Applied Mechanics and Engineering*, 195(33-36):4287–4302, 2006.

[3.9] N. A. Hawker and Y. Ventikos. Interaction of a strong shockwave with a gas bubble in a liquid medium: A numerical study. *Journal of Fluid Mechanics*, 701:59–97, 2012.

[3.10] S. Li, R. Han, A. M. Zhang, and Q. X. Wang. Analysis of pressure field generated by a collapsing bubble. *Ocean Engineering*, 117:22–38, 2016.

[3.11] C. K. Turangan, G. J. Ball, A. R. Jamaluddin, and T. G. Leighton. Numerical studies of cavitation erosion on an elastic–plastic material caused by shock-induced bubble collapse. *Proceedings of the Royal Society A: Mathematical, Physical and Engineering Sciences*, 473(2205):20170315, 2017.

[3.12] Shuji Hattori, Takuya Hirose, and Kenichi Sugiyama. Prediction method for cavitation erosion based on measurement of bubble collapse impact loads. *Wear*, 269(7-8):507–514, 2010.

[3.13] Shrey Joshi, Jean Pierre Franc, Giovanni Ghigliotti, and Marc Fivel. Bubble collapse induced cavitation erosion: Plastic strain and energy dissipation investigations. *Journal of the Mechanics and Physics of Solids*, 134, 2020.

[3.14] Chao Tsung Hsiao, A. Jayaprakash, A. Kapahi, J. K. Choi, and Georges L. Chahine. Modelling of material pitting from cavitation bubble collapse. *Journal of Fluid Mechanics*, 755(September):142–175, 2014.

[3.15] R. H. Richman and W. P. McNaughton. Correlation of cavitation erosion behavior with mechanical properties of metals. *Wear*, 140(1):63–82, 1990.

[3.16] Zheng Li, Shuman Xia, Jun Wang, and Xianyue Su. Damage detection of cracked beams based on wavelet transform. *International Journal of Impact Engineering*, 32(7):1190–1200, 2006.

Chapter 4

Wave Propagation and Plastic Deformation of Metals and Polymers

4.1 Introduction

From the elastic perspective, a recent numerical study by Wang et al. [4.1] extensively evaluated the effect of a single shock-induced bubble collapse on material acoustic impedance. A parametric study of the ratio between the solid material and water acoustic impedance Z/Z_0 clarified that the impact pressure is defined by the reflection of the shockwave from the bubble collapse to the solid surface. A higher value of Z/Z_0 indicates a "harder" material, which leads to a stronger reflection of shockwaves emitted from the bubble collapse that can accelerate the liquid jet, which in turn leads to a higher impact pressure. Conversely, a lower impact pressure was emitted from the slower liquid jet for lower values of Z/Z_0 owing to weaker shockwave reflection. Hence, it can be deduced that cavitation bubble collapse is essentially a wave-transfer phenomenon.

The analysis from previous chapter shows the relationship between bubble collapse impact load (BCIL) and impact energy ΣE_n and acoustic impedance z. For metals, it shows direct proportionality with z. Correlating with the recent findings from Wang et al. [4.1], it can be concluded that the measured BCIL on a solid material's surface only explains the reflected wave from the bubble collapse. However, no study has been conducted on the absorbed or transmitted waves inside solid materials to clearly reveal the whole wave propagation of BCIL inside solid materials, particularly metals. Therefore, it will be carried out in this chapter. One of the way to analyze how much the elastic properties affect measured value of BCIL is by changing the solid material thickness. By changing the value of thickness, the time

required of BCIL wave to transmit and reflect inside the materials will be varied, resulting in a unique wave propagation frequency for each case. Further explanation about these frequencies will be carried out in Section 4.2.2.

The analysis from previous chapter about plasticity effect in impact energy ΣE_n indicates that for polymers, the value was heavily affected by yield strength. However, the defining parameters that can define the relationship between cavitation damage and σ_y in polymers has not yet been found. From the simulation results of polymers with elasto-plastic and strain-hardening model, plastic deformation was quickly created upon collapsing bubble. The plastic deformation grows over time, forming a hole as known as cavitation pit. The initial stage of plastic deformation represents the incubation period which continue with erosion that is commonly observed in cavitation erosion test of metals. Therefore, for polymers, the relationship between plastic deformation and σ_y will be observed in this chapter.

Other than wave propagation behavior and plastic deformation, the material properties data range is also another thing to be concerned about. The range of z on the materials used from previous chapter were not wide enough. For polymers, it was heavily concentrated on the range 0.5 - 0.6 $\times 10^6\,\mathrm{N\,s\,m^{-3}}$ while for metals it was 1.4 - 1.5 $\times 10^6\,\mathrm{N\,s\,m^{-3}}$. Therefore, in order to explore cavitation damage mechanism in broader range of material properties, materials consisting of metals and polymers with z value in the range of 0.7 - 1.3 $\times 10^6\,\mathrm{N\,s\,m^{-3}}$ will be analyzed in this chapter.

4.2 Methods

4.2.1 Problem Description

The numerical problem analyzed in this study is similar with the previous chapter, which is 2D axial symmetric model of an air-filled bubble placed at the end of a narrow and long channel with a rigid side wall, as depicted in Figure 4.1. The side boundary of solid material was changed into roll boundary. This was performed to reproduce the impact force generated by a cloud-like bubble collapse compressing the entire coating material.

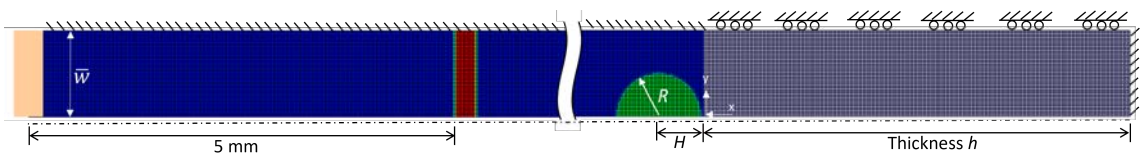

Figure 4.1: Simulation Model.

The red region in Figure 4.1 depicts an area of water with 3.75 GJ/kg of internal energy, which then creates an incoming planar shockwave that travels to both ends.

A non-reflective boundary is applied to the left end; therefore, the shockwave passes through, and the left end will not be the area of interest. On the right end, the incoming shock is reflected as a rarefaction wave upon contact with the air bubble and rigid sidewall. The reflection from the rigid side wall is an approximation of the cavitation bubble cloud phenomena, where a single bubble is surrounded by multiple nearby bubbles collapsing, producing shockwaves that reflect one another, as depicted in the illustration in Figure 3.1.

The air-filled bubble was placed at a distance $H = 1.03$ mm from the material, with radius $R = 0.5$ mm, giving a standoff distance $\gamma = 1.06$. Experimental studies of shock-induced bubbles [4.2] and single bubble collapses [4.3] near solid boundaries have shown that in the range of $1 \leq \gamma \leq 1.2$, nonspherical collapse occurs, which creates a high impact pressure on the solid. Moreover, $\gamma = 1.06$ was simulated in the Chapter 3 and it provides highly comparable maximum impact load results compared with the cavitation erosion test conducted by Hattori and Itoh [4.4].

The boundary wall is defined as a material with an elastic–perfectly plastic model and a thickness parameter h. There are additional materials incorporated in this study, which are magnesium, nylon, and Teflon. The material properties is depicted in Table

Table 4.1: Additional solid material properties.

Material	ρ	E (GPa)	z (10^5N s m^3)	σ_y (MPa)
Magnesium	1780	33	12.40	190
Teflon	2160	6.90	10.70	50
Nylon	1140	10.23	10.30	50

The thicknesses of the metals were 5, 3, 1, and 0.5 mm, whereas for polymers they were 5, 3, and 1 mm. The inference of the BCIL thickness is shown in Figure 4.2. Cavitation bubble collapse is essentially a wave propagation transfer phenomenon from a fluid to a solid. When a jet is emitted from the toroidal collapse phase, it penetrates the solid material as reflected and transmitted waves. The transmitted wave propagates inside the material either as compression (P-wave) or shear (S-wave) waves in the longitudinal and transverse directions, each with different wave speeds. The reduction in thickness reduces the travel time required for one wave transmitted from the surface to travel to the fixed boundary and then back to the surface. Hence, the same material with different thicknesses will show different tendencies in the BCIL history. To help us dissect the complex wave-transfer phenomena of bubble collapse, a continuous wavelet transform analysis of the BCIL signal was performed to determine the dominant frequency modes. Then, the obtained modes were compared to several wave propagation frequencies from the solid

material properties.

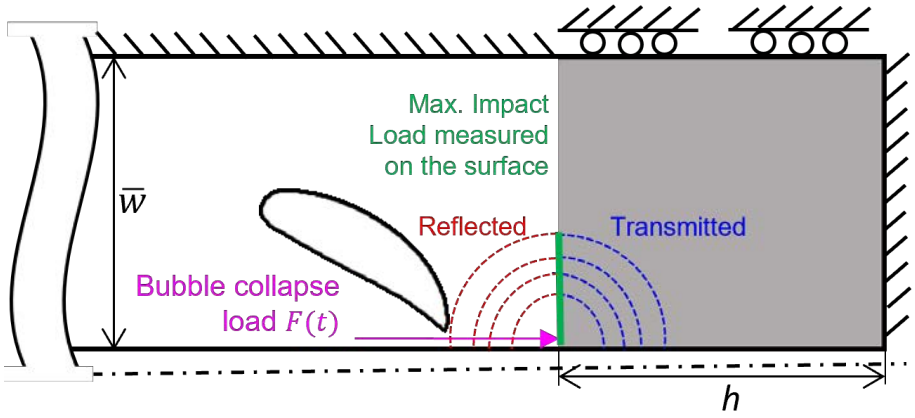

Figure 4.2: Schematic of wave transfer phenomena from fluid to solid side when the toroidal bubble collapse occurred. When the jet touches solid's surface, the BCIL propagates as reflected and transmitted wave.

4.2.2 Wave Propagation Frequency Inside Solid Materials

When a ductile material is subjected to an external force, internal stresses are transmitted from atoms to atoms at a certain specific velocity. Stresses generally propagate in the form of elastic waves. However, when it reaches its elastic limit, plastic deformation sets in, and plastic waves occur. The speed of a plastic wave is defined by its strain rate $\mathrm{d}\sigma/\mathrm{d}\epsilon$ [4.5]. However, in this study, the constitutive model was elastic and perfectly plastic, which defines $\mathrm{d}\sigma/\mathrm{d}\epsilon$=0. Therefore, the wave propagation due to BCIL is mainly focused on elastic waves.

Cao et al. [4.6] introduced a spherical pressure wave generated from a monopole source into a three-dimensional cylindrical domain in a coupled fluid and solid solver. The spherical pressure wave was set to a parameter that resembled the shockwave emitted from a single bubble collapse. It was found that the transmitted wave in the solid propagates in the form of a compressional wave (or P-wave) and a distortional wave (or S-wave) with a spherical shape, which indicates that it propagates in both the longitudinal and transversal directions.

In this study, a wave propagation frequency parameter was introduced. The compressional wave speed c_p is defined in Equation 4.1, where E is the Young's modulus and ρ is the density of the solid material. The dilatational wave speed cs is defined in Equation 4.1, where G is the shear modulus of the solid material. The values of c_p and c_s are listed in Table 4.2.

$$c_p = \sqrt{\frac{E}{\rho}}; \quad c_s = \sqrt{\frac{G}{\rho}} \tag{4.1}$$

Table 4.2: Elastic wave speed of solid materials.

Material	c_p (m/s)	c_s (m/s)
SS304	4985	3122
Titanium	5097	3102
Al2024	5129	3145
Magnesium	4871	3045
Teflon	1787	1039
Nylon	2996	1797
Adiprene	2121	1272
Epoxy	923	552
PE	803	426

Based on the bubble collapse wave-transfer phenomena illustrated in Figure 4.2 and findings from [4.6], the transmitted wave, which consists of compressional and dilatational waves (P and S waves), propagates from the solid surface in both the longitudinal (h direction (thickness)) and transversal ($\bar{w}$ direction (channel radius)) directions. The frequencies f_{PL} and f_{SL} shown in Equation 4.2 depict the time required for P and S waves to propagate from the solid surface into the fixed edge and then reflect back to the surface in the longitudinal direction.

$$f_{PL} = \frac{c_p}{2 \times h}; \quad f_{SL} = \frac{c_s}{2 \times h} \tag{4.2}$$

Conversely, the frequency of P and S wave that propagates in transversal or channel radius $\bar{w}$ direction, are calculated by using Equation 4.3.

$$f_{PT} = \frac{c_p}{2 \times \bar{w}}; \quad f_{ST} = \frac{c_s}{2 \times \bar{w}} \tag{4.3}$$

In addition to the elastic wave that propagates inside solid materials, there is an interfacial wave between the fluid and solid areas that propagates in the transverse direction. For simplicity, the propagation speed is assumed to be equal to the sound speed of water, c_0, with the propagation frequency f_{WT} defined in Equation 4.4.

$$f_{WT} = \frac{c_0}{2 \times \bar{w}} \tag{4.4}$$

All of these frequencies are used to analyze the continuous wavelet transform results of the BCIL history for each solid material with a certain thickness.

4.3 Results and Discussion

4.3.1 Thickness Reduction Effect on Bubble Deformation Behavior

The response in the solid material domain is clearly the main focus of this study, as it is directly related to the damage mechanism. However, because there is evidence that collapse characteristics such as the jet and shockwave of a bubble can change when a certain parameter of the solid material is changed [4.7–9], this section discusses how a reduction in the thickness of the solid material can affect the bubble collapse characteristics.

Ohl et al. [4.10] observed an aspherical single bubble collapse generated from a laser pulse and observed its distinct jet and shockwave formation. The first is called the jet torus shockwave, which occurs when a bubble loses its spherical symmetry. As the shape becomes concave and with decreasing volume, the upward and downward bubble boundaries will finally penetrate themselves, and the second shockwave, called the tip bubble shockwave, forms and hits the boundary wall. Lindau and Lauterborn [4.11] considered the velocity between the upward and downward boundary movement from when the bubble starts to lose its spherical symmetry until self-penetration occurs, generating a noteworthy shockwave pressure. Therefore, the distance between the upward and downward boundaries of the bubble for solid materials with various thicknesses was examined.

Figure 4.3 shows the evolution of bubble aspherical deformation of Ti for various thicknesses. The horizontal coordinate depicts the distance from the solid surface, with $x = 0\,\mathrm{mm}$ representing the fluid and solid interface. The vertical coordinate represents the channel radius with $y = \bar{w} = 1\,\mathrm{ms}$. At first glance, thickness reduction has no significant effect on bubble deformation from the initial spherical shape to the jet self-penetration phase.

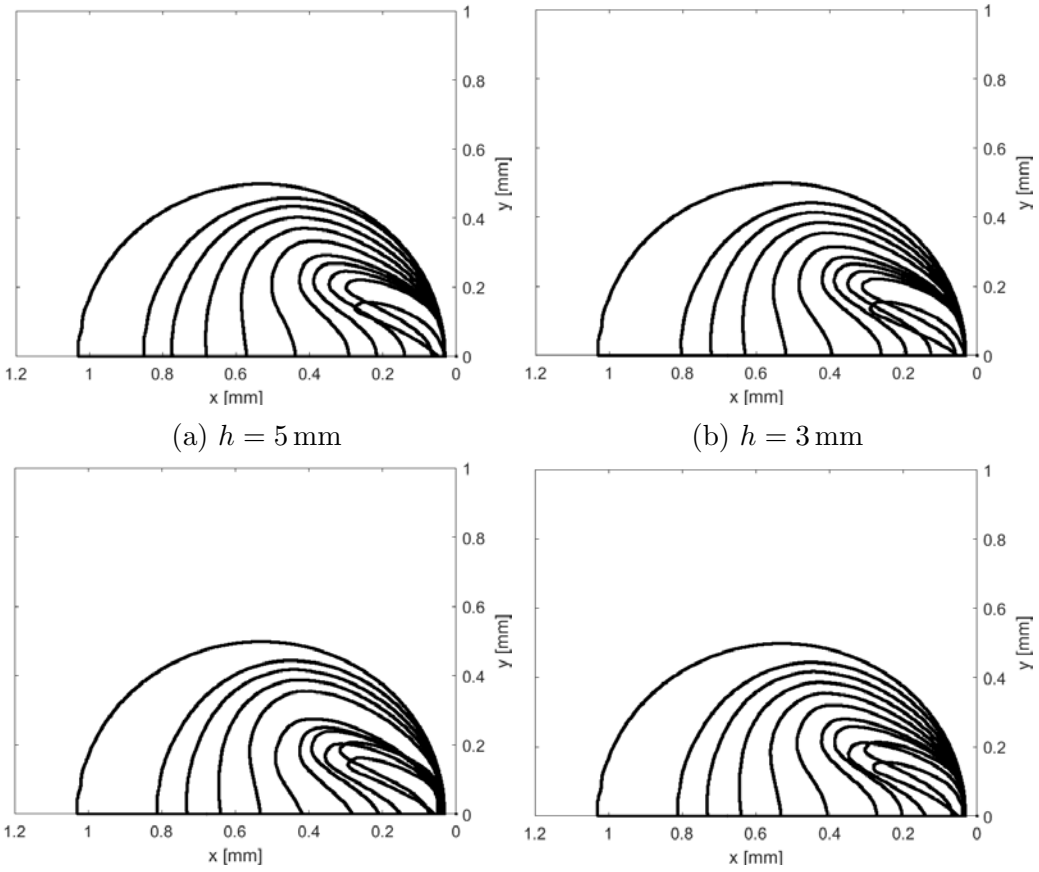

(a) $h = 5\,\text{mm}$ (b) $h = 3\,\text{mm}$

(c) $h = 1\,\text{mm}$ (d) $h = 0.5\,\text{mm}$

Figure 4.3: The evolution of nonpherical bubble deformation extracted at the same time for Titanium case.

A more detailed analysis of the upward and downward boundary movements is performed based on the deformation shape shown in Figure 4.3. At $t = 0\,\text{ms}$, the bubble shape was fully spherical. Therefore, the upward boundary coordinate is $x_+(0) = 0.3\,\text{mm}$, while the downward boundary coordinate is $x_\pm(0) = 1\,\text{mm}$. This results in the difference between the upward and downward boundaries being $x_\pm(0) = 1\,\text{mm}$, which is equal to the initial bubble diameter, $2R$. The evolution of $x_\pm$ from the initial spherical phase ($x_\pm(0) = 1\,\text{mm}$) to the jet self-penetration or toroidal phase ($x_\pm(t) = 0\,\text{mm}$) for all solid materials with various thicknesses is depicted in Figure 4.4.

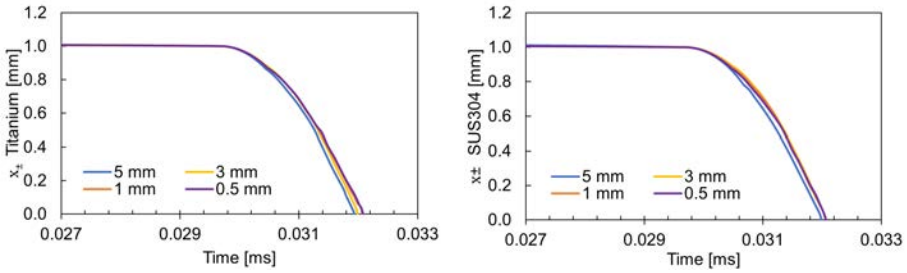

(a) Titanium

(b) SUS304

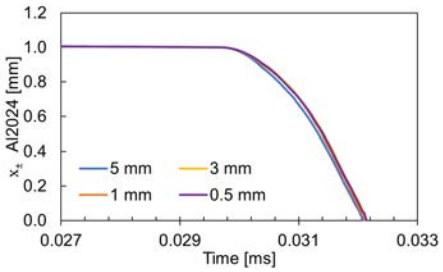

(c) Al2024

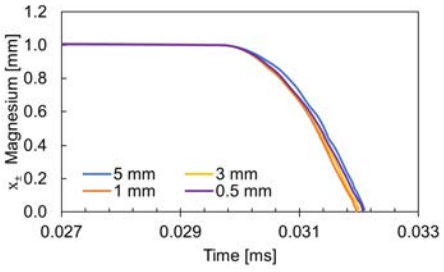

(d) Magnesium

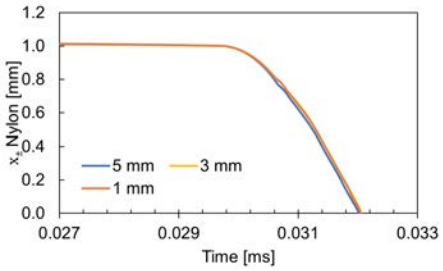

(e) Nylon

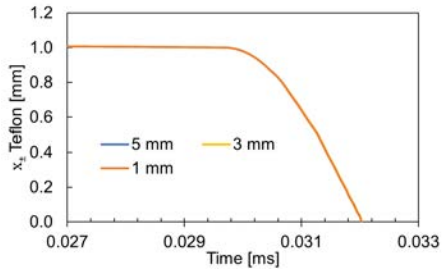

(f) Teflon

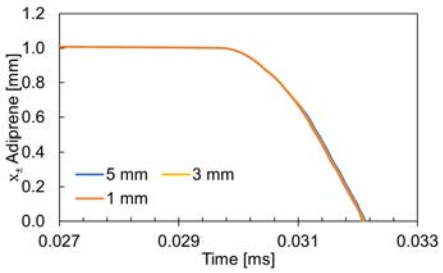

(g) Adiprene

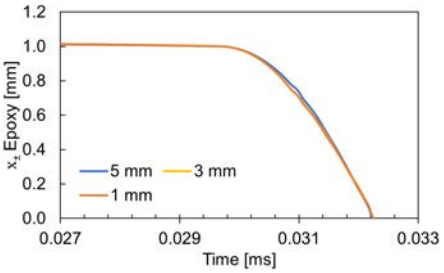

(h) Epoxy

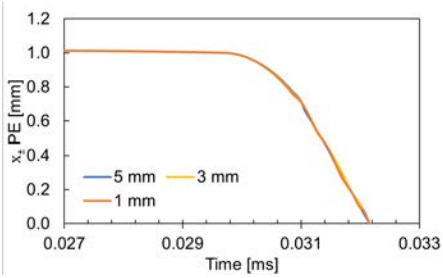

(i) PE

Figure 4.4: The difference of upward and downward bubble boundary movement $x_{\pm}$ for all solid materials in various thicknesses. There is no significant change due to thickness reduction as mostly bubble starts to lose its spherical symmetry at 0.299 ms, and became toroidal ($x_{\pm} = 0$ mm) at 0.032 ms.

As shown in Figure 4.4, the bubble starts to lose its spherical symmetry (the value of $x_{\pm}$ starts to decay from 1 mm) from $t = 0.297$ ms. Then, it reaches the jet torus shockwave phase marked by self-penetration ($x_{\pm} = 0$ mm), which leads the bubble shape to toroidal t_0. After the self-penetration, shockwave and jet start to emerge. Lindau and Lauterborn [4.11] developed an estimation of the velocity of impinging jet at time t as

$$v_{\pm}(t) = \frac{\pm c_L t}{\sqrt{t^2 - t_0^2}} \tag{4.5}$$

The value of t_0 can be obtained from Figure 4.4, where the value of $x_{\pm} = 0$. The value of t_0 is slightly differs especially between metals and polymers. In metals, the downward bubble boundary touches the upward boundary (self-penetration) faster than polymers. Therefore, the calculation of jet velocity is made with the assumption that t occurs at the same Δt after t_0. Table 4.3 below shows the estimated jet velocity occurs after 50 µs of self penetration phase.

Table 4.3: Estimated jet velocity $v_{\pm}(t)$ (m/s) when $t = t_0 + 50$ µs .

Material	Thickness			
	5 mm	3 mm	1 mm	0.5 mm
SS304	26531	26556	26589	26593
Titanium	26556	26589	26589	26585
Al2024	26589	26618	26605	26618
Magnesium	26605	26564	26543	26589
Teflon	26572	26572	26568	-
Nylon	26568	26580	26568	-
Adiprene	26609	26597	26589	-
Epoxy	26642	26642	26642	-
PE	26634	26634	26634	-

From Table 4.3, it is shown that there is no significant variation in terms of jet velocity $v_{\pm}(t)$. Even though the self-penetration timing t_0 on metals are slightly faster than polymers, the jet velocity estimated after 50 µs are shown to be the same. This indicates that the mechanical input from fluid domain only slightly differs in timing, however, for the intensity, it is deemed to be constant for all cases.

4.3.2 Thickness Reduction Effect on Maximum Impact Loads

To obtain the BCIL history, this study applied a process that is similar to one used in a previous study. The maximum impact load from the bubble collapse for certain solid material thicknesses is plotted against the acoustic impedance z (Figure 4.5). For polymers, the relative standard deviation between the thicknesses of each material is approximately 2–8%. For metals, it is approximately 12%–20%. This shows that the BCIL in metals is heavily affected by thickness reduction, while in polymers it is not.

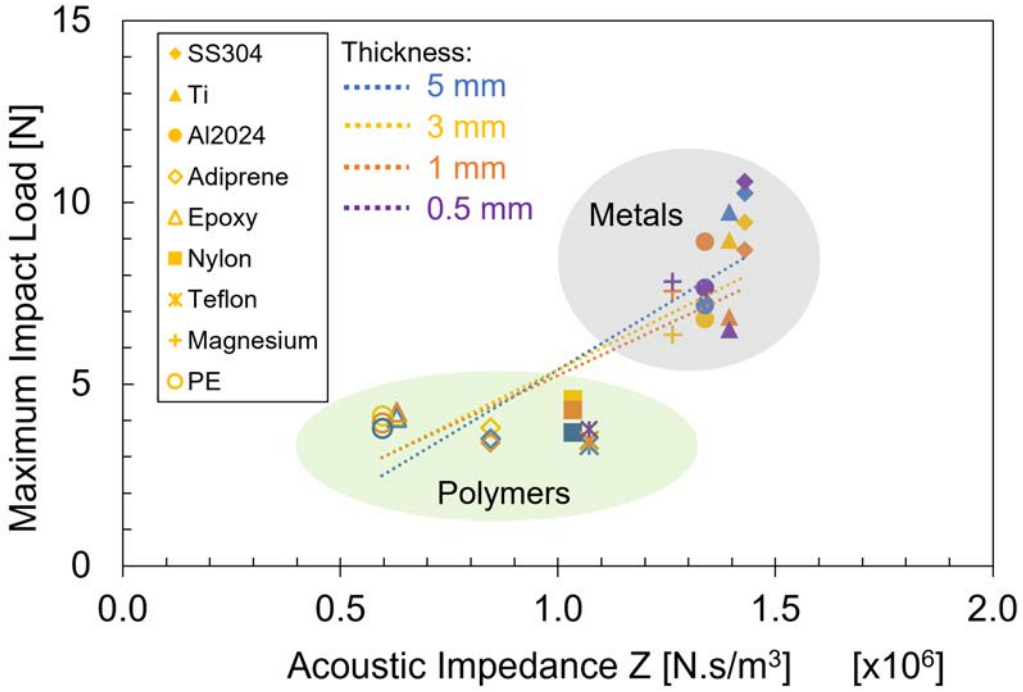

Figure 4.5: The maximum impact load of bubble collapse of metals and polymers for certain thicknesses.

When observed in more detail, the maximum impact load value for Ti decreased as the thickness decreased. For SUS304, the maximum impact load decreased between thicknesses of 5 mm to 1 mm. However, for a thickness of 0.5 mm, the maximum impact load increases significantly, becoming greater than that for 5 mm. For Al2024, the maximum impact load decreased between thicknesses of 5 mm to 3 mm. Between 1 mm and 0.5 mm, there is a significant increase. For Mg, a similar phenomenon to that of Al2024 appeared. The main cause of the increased maximum impact load in thinner metals should be analyzed further, because damage caused by cavitation bubble collapse mainly occurs because of fatigue fracture from repeated BCIL [4.4]. Therefore, the force input from the fluid domain, which is the jet and shockwaves from bubble collapse, is discussed in this section.

The discussion in the previous section indicates that there is no inference of the

jet torus shockwave with a solid thickness. However, the value of the impact loads for metals shows noteworthy variance, which indicates that there is an inference to solid thicknesses. This raises the question of how the maximum impact load changes significantly when the external input force from the fluid domain is almost constant within the individual cases. In any case, it indicates another underlying phenomenon behind the maximum impact load timing. Evidence from the experiment involving vapor bubble collapse generated from a focusing laser inside water [4.12] shows that for $1 < \gamma < 3$, another phenomenon called counterjet shockwave emerges rapidly and remains for a longer period of time than the initial collapse time, which is the jet torus shockwave. The standoff distance γ analyzed in this study was 1.06. Therefore, there is a high possibility that the counterjet shockwave dominates the maximum impact load received on the solid surface.

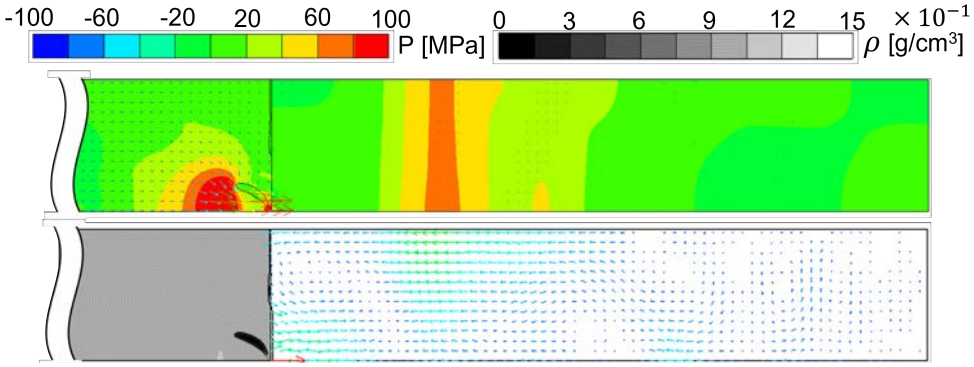

(a) Jet torus shockwave at $t = 0.031\,95\,\text{ms}$.

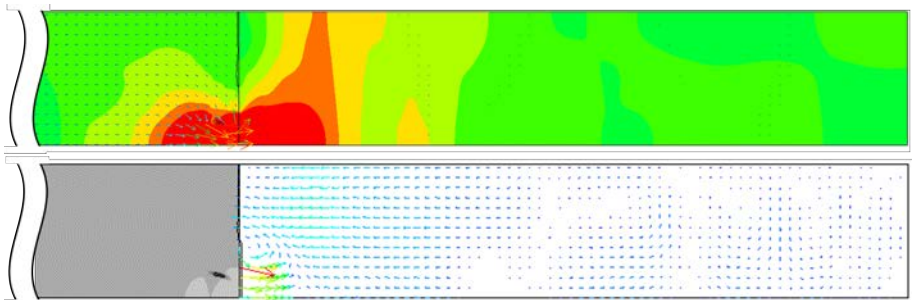

(b) Counterjet shockwave starts to emerge at $t = 0.032\,05\,\text{ms}$.

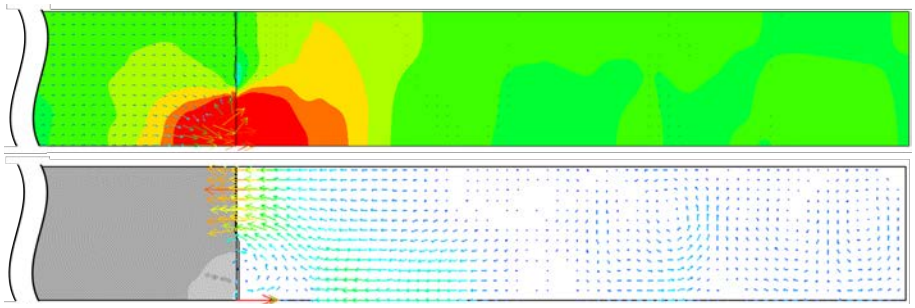

(c) Maximum impact load at $t = 0.032\,13\,\text{ms}$.

Figure 4.6: The jet and shockwaves of shock-induced bubble collapse near Titanium with thickness $h = 5\,\text{mm}$. The arrow depicts velocity vectors.

Figure 4.6 shows the jet and shockwaves that emerged from the bubble collapse for Ti with 5 mm thickness. Figure 4.6a shows the jet torus shockwave that emerged at $t = 0.03195$ms, as discussed in the previous section. Subsequently, the toroidal-shaped bubble volume continued to decrease until it reached its minimum volume and a compression shockwave emerged. Owing to the short distance between the bubble upward boundary and the solid surface ($\gamma = 1.06$), a vortex ring-like flow was formed at $t = 0.032\,05$ ms with the circulating form of velocity vectors near the solid surface (Figure 4.6b). This phenomenon, known as a counterjet shockwave, appears only when the standoff between the bubble center and the wall is greater than the maximum radius of the bubble [4.11]. This counterjet shockwave has a duration of visibility that is noteworthy when the standoff distance is $1 < \gamma < 2$ [4.12]. Figure 4.6c shows the timing of the maximum impact load. Judging from the appearance of the ring-type velocity vectors, this timing depicts a counterjet shockwave that is still circulating within its duration of visibility.

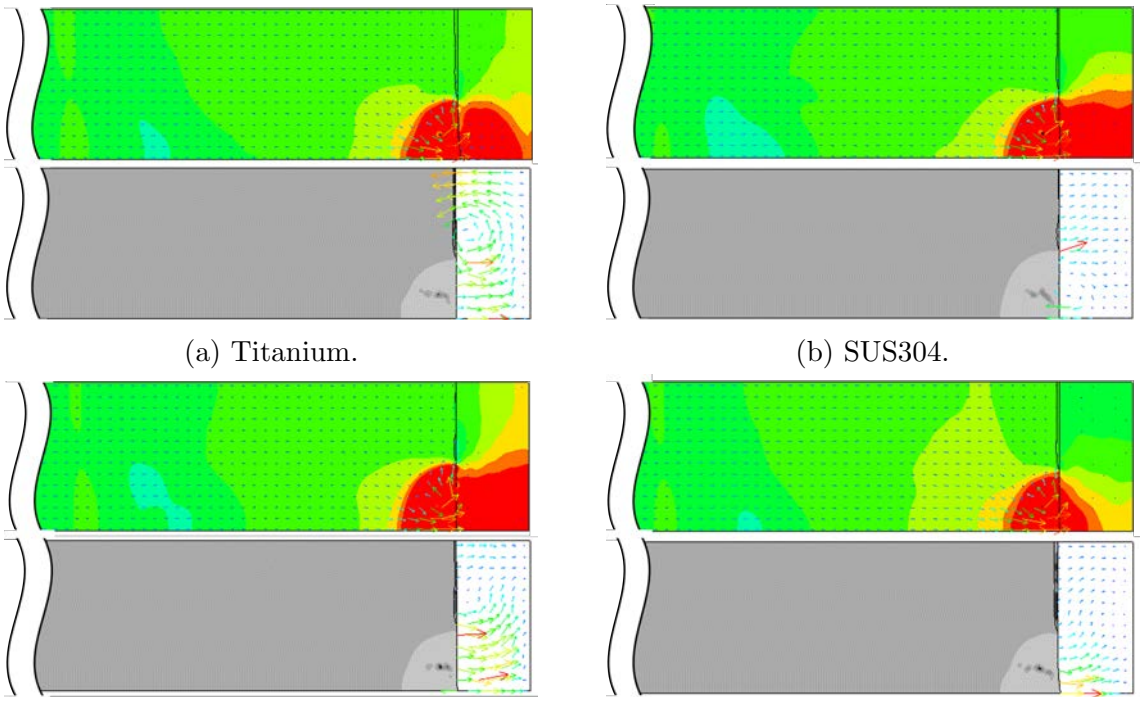

(a) Titanium. (b) SUS304.

(c) Al2024. (d) Magnesium.

Figure 4.7: Counterjet on maximum impact load timing of shock-induced bubble collapse near metals with thickness $h = 0.5$ mm. The pressure scale is similar with Figure 4.6.

The occurrence of the counterjet shockwave in the maximum impact load timing was analyzed for the thinnest metals (0.5 mm). The pressure contour at maximum impact load timing for Ti, SUS304, Al2024, and Mg is shown in Figure 10. The ring-shaped velocity vectors in the high-pressure region indicate that the counterjet caused the maximum impact loads. The main cause of the significant increase in

the maximum impact load value for SUS304, Al2024, and Mg can also be analyzed, as shown in Figures 4.7b, 4.7c, 4.7d. When the thickness is sufficiently thin, the transmitted wave that propagates inside the solid reaches the fixed right-side edge faster, causing reflection on the surface. This reflected wave that originates from the transmitted wave can amplify the BCIL measurement on the solid surface because the counterjet is still in its duration of visibility. The superposition mechanism is illustrated in Figure 4.8.

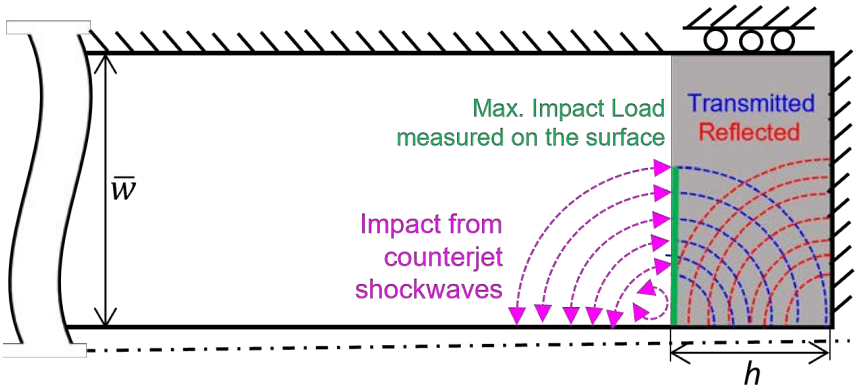

Figure 4.8: The main cause of significant increase in maximum impact load for thin metals (0.5 mm). Due to the short distance between surface and right-side fixed boundary, the transmitted wave can reflect and double the measurement of BCIL.

However, superposition did not occur in Ti (Figure 4.7a). The pressure value of the right-side fixed edge did not appear to be as high as that of the other metals. This indicates that there is a correlation between the superposition of the wave propagation frequency and the counterjet duration of visibility. To investigate this further, a continuous wavelet analysis of the thinnest metals will be provided later.

4.3.3 Frequency Modes of Bubble Collapse Impact Loads in Metals

A continuous wavelet transform was performed to analyze the BCIL signals within several materials of various thicknesses. The wavelet was based on generalized Morse wavelets in MATLAB [4.13]. The Morse wavelet has two parameters: the gamma parameter, which defines the symmetry, and P^2, which defines its time-bandwidth product. Default values of 3 and 60 were used. The results of the wavelet analysis, along with the BCIL profile for the thinnest metals ($h = 0.5$ mm), are shown in Figure 4.9. Several wave propagation frequencies were calculated to evaluate the modes from the BCIL and were mapped over the spectrum results as a dashed line. In general, three modes were found to be dominant in the wavelet energy spectrum. The lower mode, which is found for all the solid material cases with values less than

1 MHz, represents f_{WT}, and the interfacial wave propagation between the fluid and solid is calculated based on Equation 13. The energy spectrum for this mode spreads out as BCIL increases and decreases with time. Because the BCIL was measured at the solid surface, it makes sense that the fluid and solid interfacial wave propagation frequency f_{WT} becomes apparent with the spread-out energy spectrum in the wavelet results.

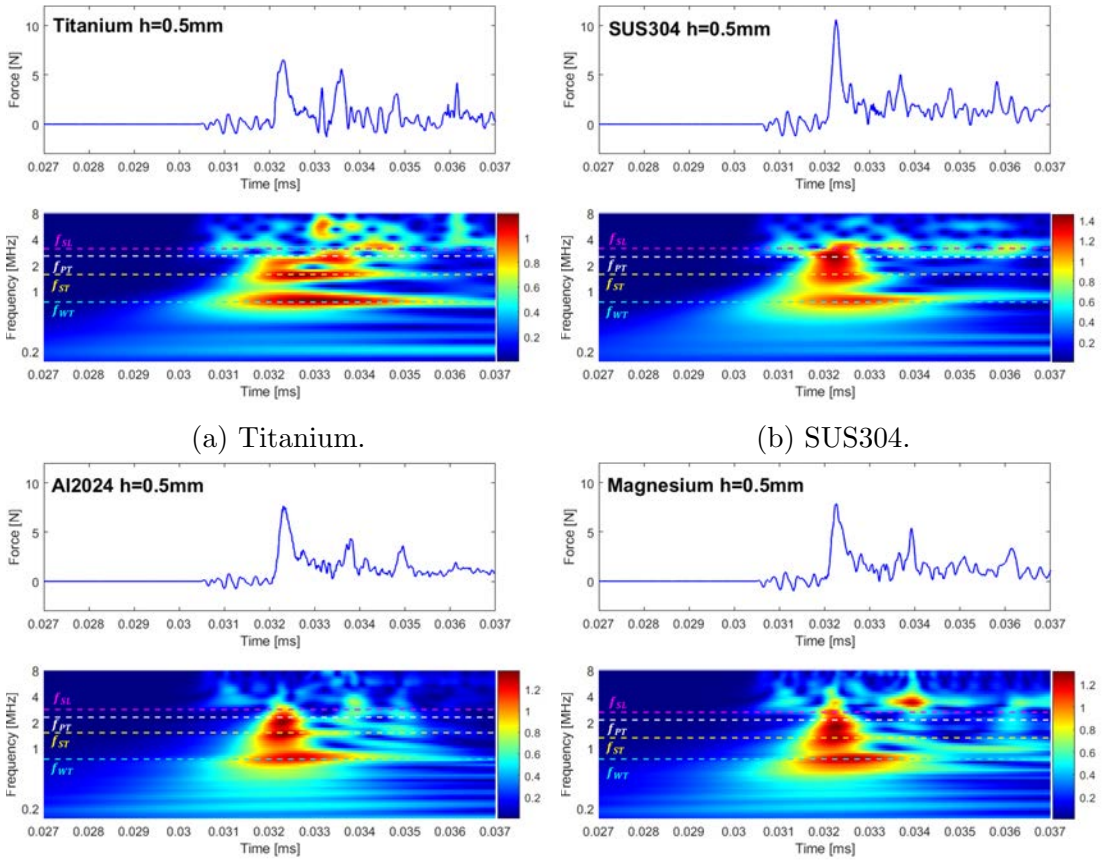

(a) Titanium.

(b) SUS304.

(c) Al2024.

(d) Magnesium.

Figure 4.9: Wavelet analysis results along with BCIL profile history for metals with thickness $h = 0.5\,\text{mm}$. The dashed line that is plotted over the wavelet spectrum shows wave propagation frequencies: f_{WT} (cyan), f_{ST} (yellow), f_{PT} (white), f_{SL} (magenta).

For the middle mode (approximately 1–2 MHz), the energy spectrum is centralized in the maximum impact load region for SUS304, Al2024, and Mg (Figure 4.9b, 4.9c, and 4.9d). However, for Ti (Figure 4.9a), the energy spectrum was more spread out after the maximum impact load timing and appeared to be less dominant. The frequency was found to correspond to f_{ST}, which is the shear or S-wave speed that propagates in the transverse direction obtained from Equation 4.3.

For the upper mode (approximately 2–4 MHz), the energy spectrum spreading pattern was the same as that of the middle mode. However, it is more concentrated in the maximum impact load timing for SUS304, Al2024, and Mg. The corresponding

wave propagation frequencies are f_{SL}, the shear or S-wave speed that propagates in the longitudinal direction obtained from Equation 4.2, and f_{PT}, the compression or P-wave speed that propagates in the transverse direction.

From the analysis discussed in Section 3.2, it was found that the significant increase in the maximum impact load for SUS304, Al2024, and Mg with $h = 0.5\,\mathrm{mm}$ was because of the superposition phenomena between the counterjet duration of visibility and the internal wave propagation speed of the solid material, as explained in Figure 4.8. The wavelet analysis results for the upper mode revealed that the superposition was with f_{SL} and f_{PT}, which caused the energy spectrum to be highly concentrated in the maximum impact load region. In the case of Ti, the energy spectrum was more spread out and less dominant because there was no superposition between its counterjet duration of visibility and either f_{SL} and f_{PT}. Hence, there was no significant increase in the maximum impact load value for $h = 0.5\,\mathrm{mm}$.

From this discussion, it can be concluded that the BCIL of metals is highly dependent on their elastic wave propagation properties. Hence, the cavitation damage mechanism of metals mostly occurs because of high-cycle fatigue phenomena, as can be explained by its elastic properties, or as evidence shows from previous studies [4.4, 6, 14]; in particular, it can be predicted with acoustic impedance. However, the thickness selection should be performed with caution. Generally, if the thickness is too thin (in this case, less than 1 mm), superposition phenomena can occur, and the maximum BCIL will increase. This increase can shorten fatigue life.

4.3.4 Frequency Modes of Bubble Collapse Impact Loads in Polymers

In this section, the damage mechanism of polymers as solid materials is explored in the same manner as that of metals. First, the phenomena causing the maximum impact load were analyzed. Figure 4.10 shows the pressure contour at the maximum impact load timing for nylon. The bubble achieved its minimum volume, with circle-shaped velocity vectors dominating the high-pressure area, indicating that it is a counterjet phenomenon. Plastic deformation in the form of a cavitation pit is more apparent in polymers, indicating that elastic wave propagation might be less important in explaining the damage mechanism.

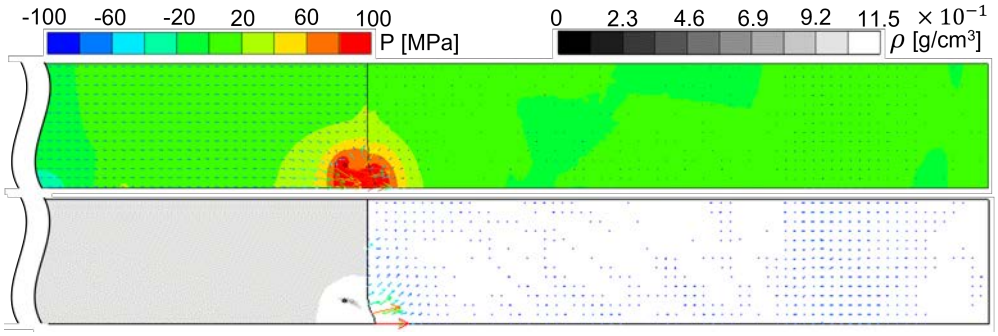

(a) Nylon $h = 5\,\text{mm}$.

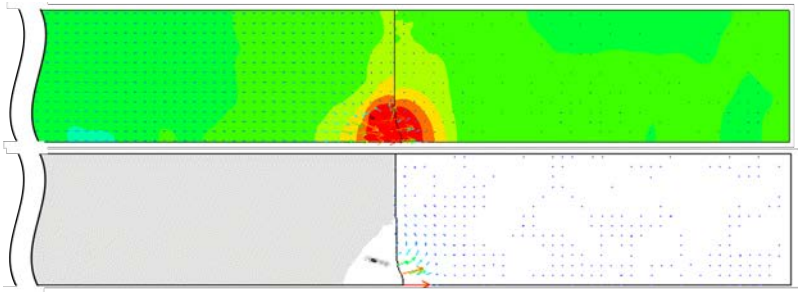

(b) Nylon $h = 3\,\text{mm}$.

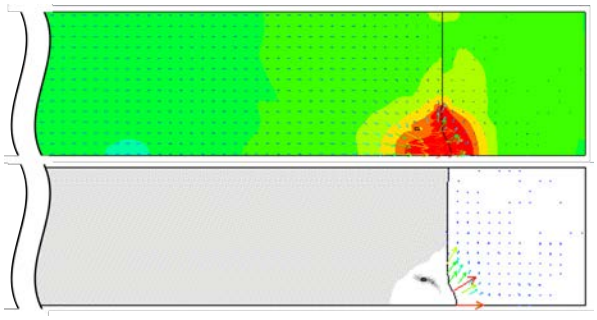

(c) Nylon $h = 1\,\text{mm}$.

Figure 4.10: Counterjet on maximum impact load timing of shock-induced bubble collapse near Nylon. The pressure scale is similar with Figure 4.6.

Continuous wavelet transform analysis results for nylon are shown in Figure 4.11. For $h = 5\,\text{mm}$ (Figure 4.11a), only one mode is shown to be dominant, which is below 1 MHz and corresponds to the interfacial wave propagation speed between fluid and solid f_{WT}. For $h = 3\,\text{mm}$ and $h = 1\,\text{mm}$ (Figure 4.11b and 4.11c), higher frequency modes appeared (around 1-2 MHz); these correspond to the compression or P-wave that propagates in tangential direction f_{PT} .

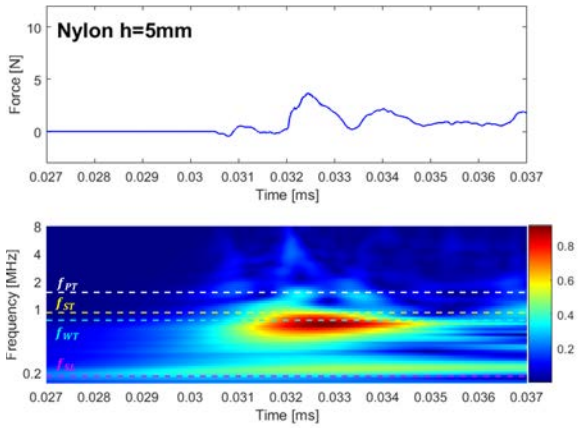

(a) Nylon $h = 5$mm.

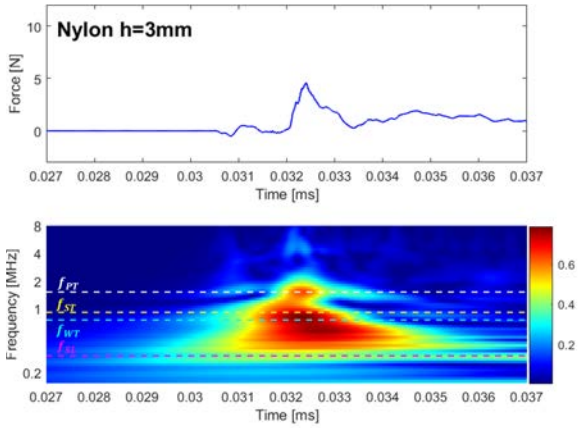

(b) Nylon $h = 3$mm.

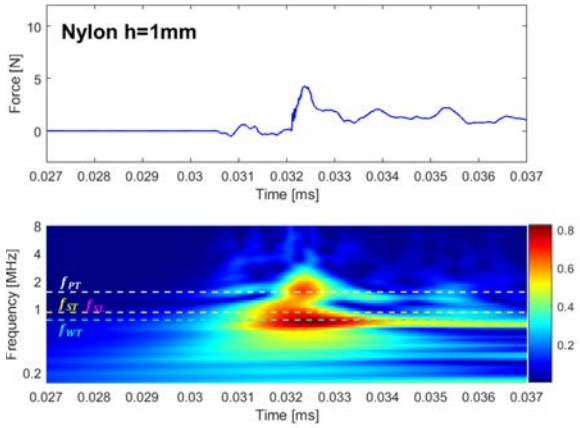

(c) Nylon $h = 1$mm.

Figure 4.11: Wavelet analysis results along with BCIL profile history for Nylon with various thickness. The dashed line that is plotted over the wavelet spectrum shows wave propagation frequencies: f_{WT} (cyan), f_{ST} (yellow), f_{PT} (white), f_{SL} (magenta).

Wavelet analysis results from the BCIL profile of polymers cannot provide any useful insight into the damage mechanism due to cavitation bubble collapse in polymers. Judging from the apparent plastic deformation, the transmitted wave that

propagates inside the polymers has surpassed its σ_y, making the elastic wave propagation speed, which was explained in Section 2.3, less dominant. Therefore, it is better to analyze the damage mechanism of polymers through the plastic deformation phase.

4.3.5 Pit Depth and Radius in Polymers

The apparent plastic deformation that occurred in nylon also appeared in every other polymer case with a lower yield strength σ_y. Plastic deformation occurred instantly when the self-penetrating jet from the bubble collapse hit the solid surface. This deformation progressed and formed a cavitation pit. By incorporating a simple image-edge detection technique, parameters such as pit depth, pit radius, and pit volume can be obtained for each output. A schematic of the cavitation pit on the polymers is shown in Figure 4.12.

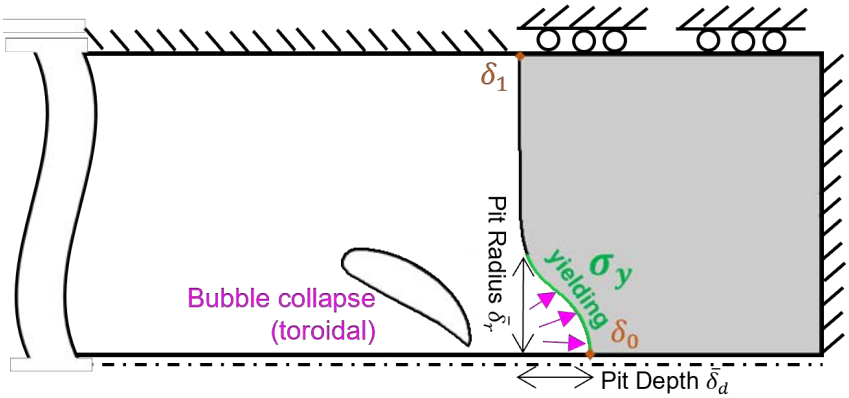

Figure 4.12: Schematic of pit formation in polymers. The edge tracking method detects the pit contour (showed in green line) which is integrated along axial symmetric axis to form pit volume.

Using the image detection, the pit radius $\bar{\delta}_r$ was measured as the farthest point of the pit curvature. The pit depth $\bar{\delta}_d$ represents the difference between the displacement at the center δ_0 and at the edge of surface δ_1 because elastic compression due to the incident shock wave also occurs at the center and edge. The pit depth and pit radius progression over time are shown in Figure 4.13. It is shown that the pit depth values vary depending on the polymer, and the largest one is PE with the lowest σ_y. However, there is minimal variation in the pit radius, particularly after 0.036 ms, when the plastic deformation has settled. The average pit depth and radius are shown in Figure 4.14. It is shown that the averaged pit radius value for all polymers is 0.25 mm, while the pit depth varies significantly from 0.1 mm to 0.6 mm

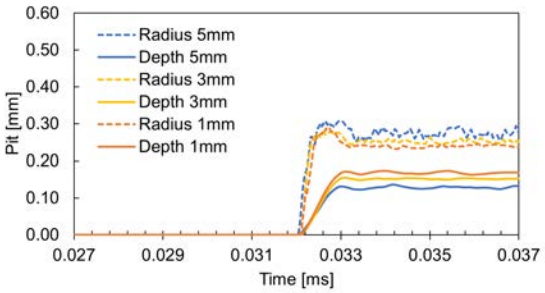

(a) Nylon $\sigma_y = 50\,\text{MPa}$.

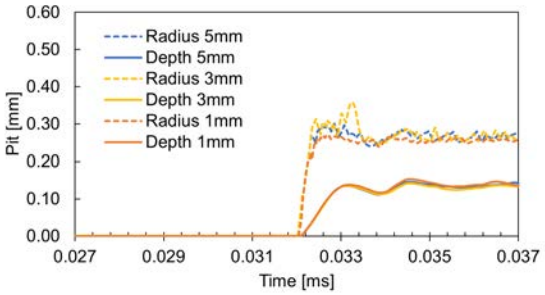

(b) Teflon $\sigma_y = 50\,\text{MPa}$.

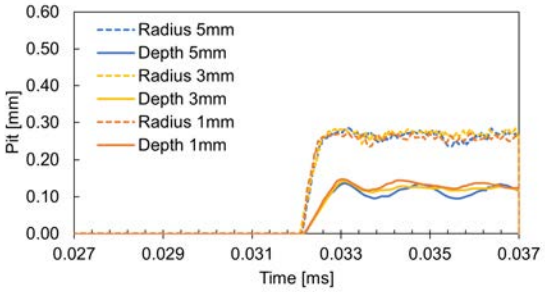

(c) Adiprene $\sigma_y = 60.6\,\text{MPa}$.

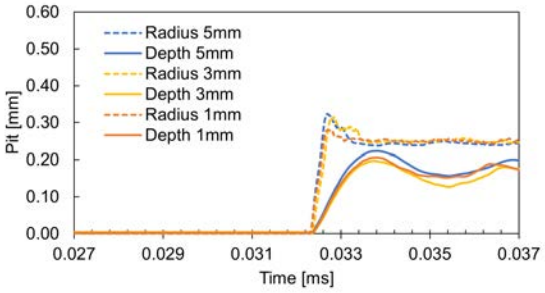

(d) Epoxy $\sigma_y = 42\,\text{MPa}$.

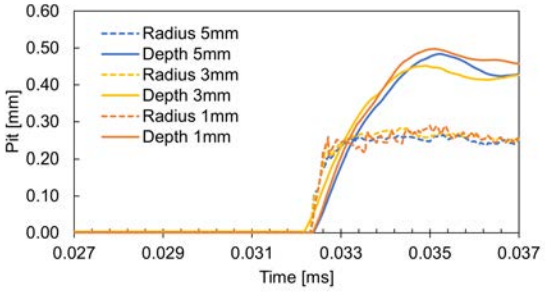

(e) PE $\sigma_y = 20\,\text{MPa}$.

Figure 4.13: Cavitation pit radius (dashed line) and pit depth for polymers.

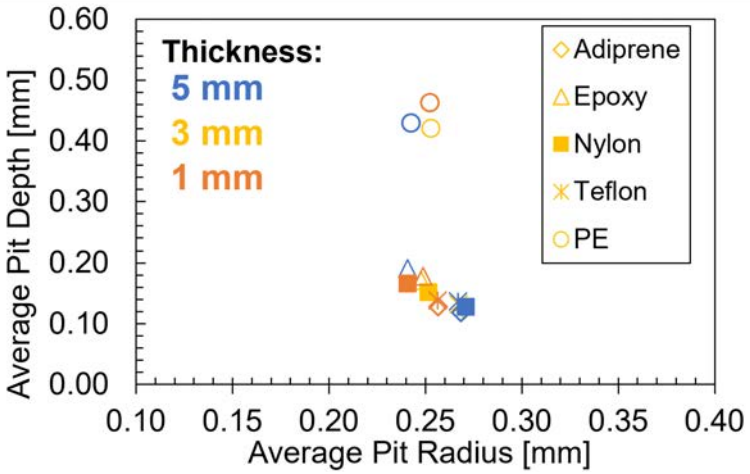

Figure 4.14: Average pit radius and pit depth.

From the discussion in Section 4.3.1, it was confirmed that there is little to no change in the bubble deformation behavior of metals and polymers. This indicates that there was no significant difference in the bubble collapse timing. The pit depth and radius shown in Figure 4.13 start to develop at approximately 0.032 ms for all polymers, indicating that the self-penetrating jet that occurred at bubble collapse instantly caused plastic deformation. The velocity that causes solid particles to skid, thus creating damage, is called the critical impact velocity [4.15]. The intensity of the damage caused by the critical impact velocity is determined not only by the value, but also by its angle. The average pit radius is almost constant, while the pit depth varies significantly, indicating that the pit grows in the depth direction. This also implies that the impact velocity of the bubble collapse in this study is damaged at an angle parallel to the depth direction.

4.3.6 Impact Energy and Plastic Work in Polymers

The previous analysis shows that the bubble deformation behavior and maximum BCIL have an influence on the material properties of polymers. An analysis of impact energy per unit area emitted from bubble collapse ΣE_n from our previous study [4.14] showed that the energy decreases significantly for polymers when yielding is introduced to the constitutive model. This indicates a strong inference of the cavitation damage of polymers to the yield strength. Hence, all the parameters analyzed in this study are plotted with reference to σ_y.

The impact energy per unit area calculated in a previous study measures the acoustic energy emitted from bubble collapse Hammitt [4.16]; thus, it can be considered as the mechanical energy input from the fluid domain. The analysis in the previous section shows that the pit radius reaches a constant average value of 0.25 mm. Figure 4.15 shows the total impact energy times for a circular area with

radius 0.25 mm at the end of the simulation time (0.037 ms) plotted against σ_y. The dashed line shows the linear trend line for all the data. A very low value of R^2 indicates that there is no inference of σ_y and that the value is considered to be constant. This means that the mechanical energy input from a bubble collapse is independent of the material properties.

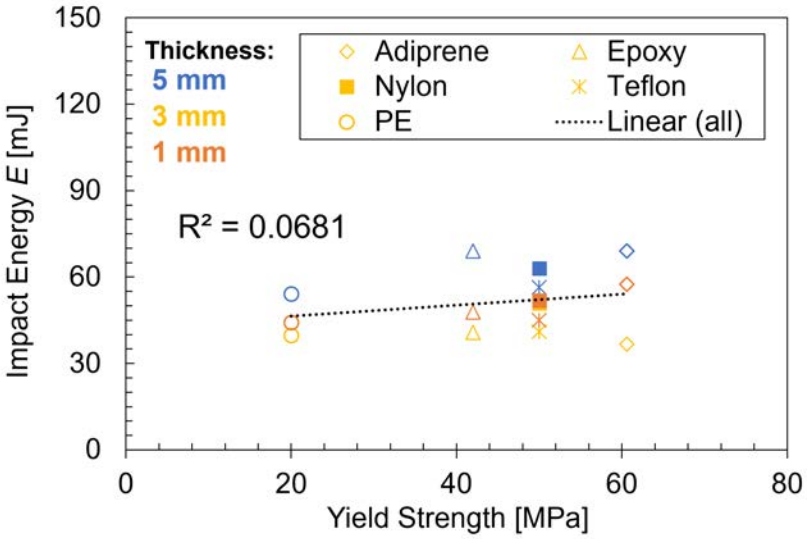

Figure 4.15: Total impact energy due to bubble collapse at 0.0370 ms for polymers.

The pit radius and pit depth analysis from the previous section showed that plastic deformation occurred quickly as the self-penetrating jet emerged from the bubble collapse. Although the pressure measured on the solid surface can exceed σ_y, the true stress along the pit curvature inside the material is equal to σ_y because of the plastic material used in the constitutive model. Therefore, the force elastic–perfectly can be modeled as σ_y times the circular area, which is defined by the pit radius $\bar{\delta_r}$ that progresses over time, whereas the displacement is the pit depth $\bar{\delta_d}$. The plastic work W_p can be calculated as

$$W_p = \sigma_y \times \pi \times \bar{\delta_r}^2 \times \bar{\delta_d} \tag{4.6}$$

The total plastic work W_p at 0.0370 ms was plotted against σ_y as shown in Figure 4.16. The dashed line shows the trend line of all the data. A low value of R_2 indicates that there is a low inference of the estimated W_p to σ_y. A more detailed methodology is required to evaluate other plastic deformation parameters that can be used to explain cavitation damage in polymers.

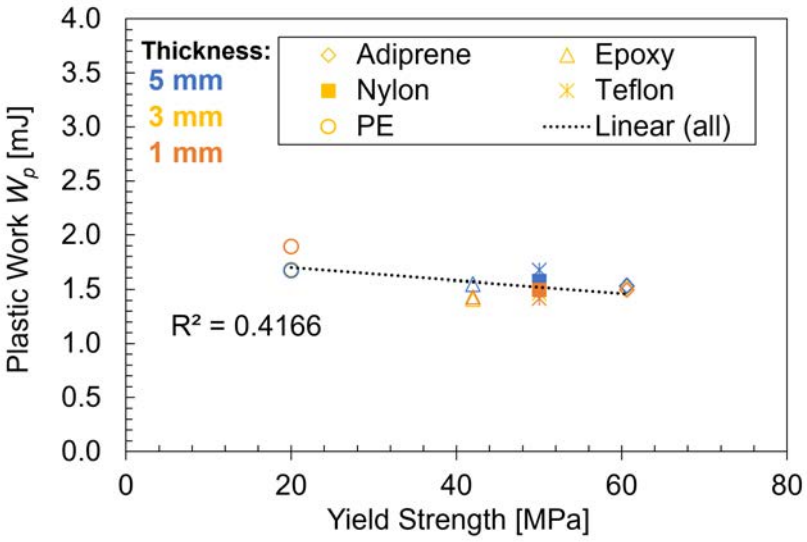

Figure 4.16: The plastic work at 0.0370 ms for polymers.

4.3.7 Pit Volume Analysis in Polymers

The cavitation pit that occurs in polymers is defined not only by the pit depth and radius but also by the surface, which is marked as a green-colored curve in Figure 4.12. In this section, a more detailed analysis is performed using the image-edge detection technique to carefully detect the edges on the pit curvature. Subsequently, a cumulative integral was performed to calculate the pit curvature, which was calculated by integrating the pit curvature along the axial symmetric axis. Figure 4.17 shows that the cavitation pit volume progresses over time for all polymers. It can be observed that plastic deformation begins at 0.0320 ms.

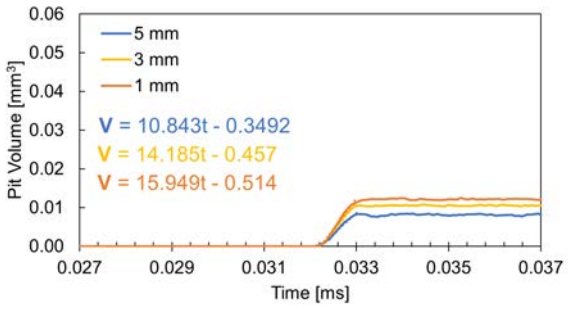

(a) Nylon $\sigma_y = 50\,\text{MPa}$.

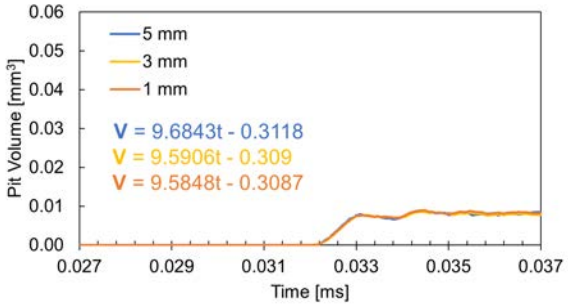

(b) Teflon $\sigma_y = 50\,\text{MPa}$.

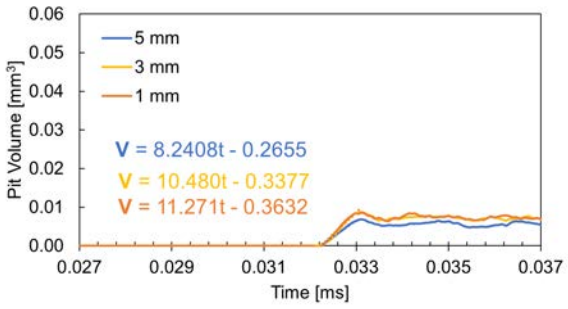

(c) Adiprene $\sigma_y = 60.6\,\text{MPa}$.

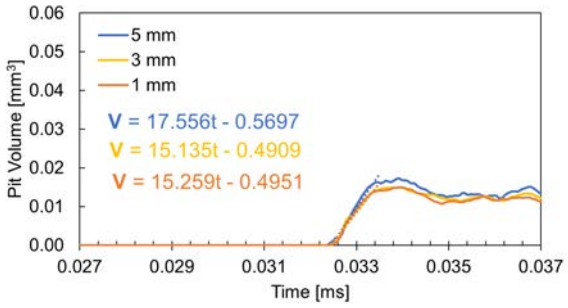

(d) Epoxy $\sigma_y = 42\,\text{MPa}$.

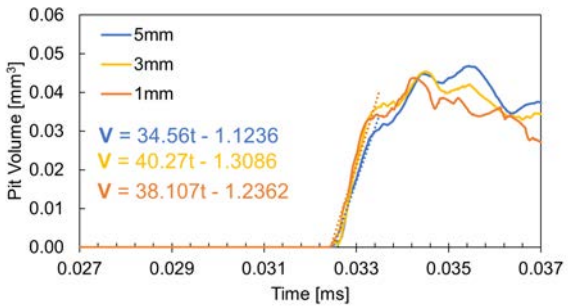

(e) PE $\sigma_y = 20\,\text{MPa}$.

Figure 4.17: Cavitation pit volume for polymers.

The equation written along the graph is a linear regression of the slope of the cavitation pit formation to represent the pit growth rate of each polymer from 0.0320 - 0.0330 ms, which can be expressed as

$$\mathbf{V} = \dot{V}t + b \tag{4.7}$$

with $\mathbf{V}$ as pit volume, $\dot{V}$ as pit volume growth rate, t as time, and b as the constant product from linear regression. The pit growth rate depicts how the pit form at the beginning of jet from bubble collapse.

The pit volume and growth rate for PE, which had the lowest σ_y, were shown to be the highest. Conversely, Adiprene, which had the highest σ_y, had the lowest cavitation pit volume and growth rate, although by a relatively small margin. The value of $\dot{V}$ is mapped against σ_y as shown in Figure 4.18a. The dashed line in each figure represents the nonlinear regression with a third-degree polynomial. The value of R^2 is greater than 0.9, indicating that there is a strong inference of the initial plastic deformation phase of polymers owing to cavitation bubble collapse and σ_y.

When a self-penetrating jet from a bubble collapse hits the solid surface, plastic deformation occurs instantly until it reaches its maximum value and then settles over time, generating a residual permanent deformation upon the material known as cavitation damage. To represent this phenomenon, two parameters—averaged pit depth and pit volume taken from 0.0360 ms to 0.0370 ms—are plotted against σ_y (Figure 4.18b, 4.18c). These two parameters represent the incubation-like period in polymers, which occurred before particle removal in the cavitation erosion test. The values of R^2 are all greater than 0.9, showing that both averaged pit volume and pit depth are dominated by the initial plastic deformation phase. From this analysis, it can be surmised that both initial plastic deformation phase and incubation-like period in polymers are determined by σ_y.

4.3.8 Cavitation Damage Mechanism of Polymers

The maximum impact load and impact energy measurement in the cavitation erosion test conducted by Hattori and Itoh [4.4] only clarified that the impact load acting on the polymer surface was much lower than that of metals because polymers have a lower acoustic impedance. In this study, polymers with a broader range of acoustic impedances were investigated. It was found that the maximum impact load of polymers with various thicknesses had no effect on acoustic impedance. There is also no appearance of an elastic wave frequency inside the continuous wavelet transform analysis of BCIL. Consistent with the results of Hattori and Itoh [4.4], it is clear that BCIL only represents wave reflection on a solid surface. Therefore, for polymers with relatively low acoustic impedance, it is not appropriate to evaluate cavitation

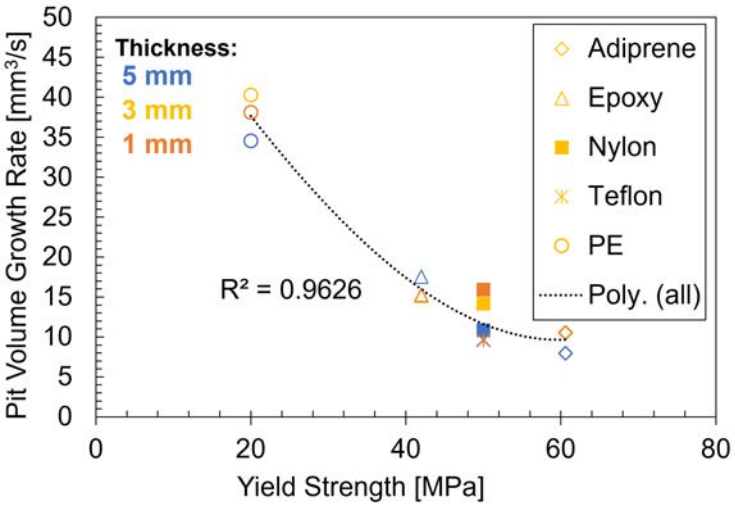

(a)

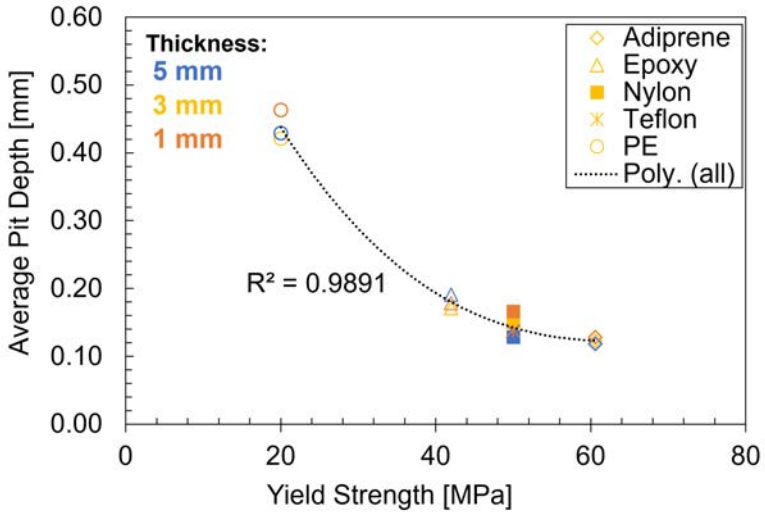

(b)

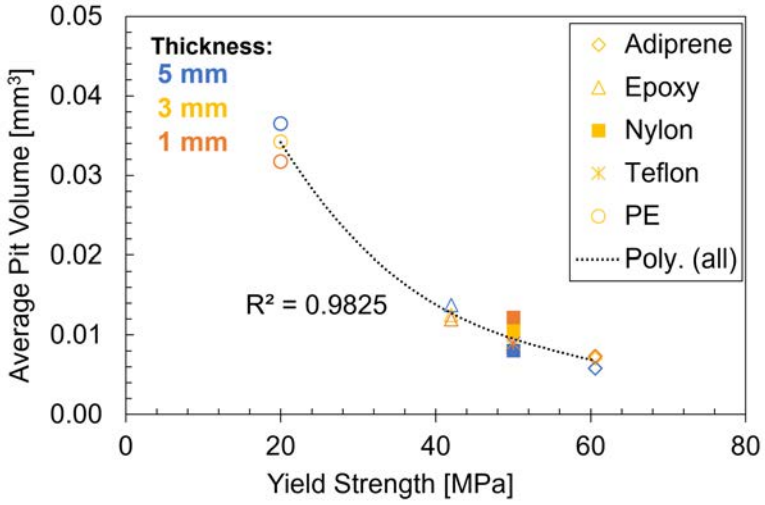

(c)

Figure 4.18: (a) Pit volume growth rate, (b) averaged pit depth, (c) average pit volume, for all polymers against yield strength σ_y. The dashed trendline shows a non-linear regression of third degree polynomial.

damage through their elastic properties.

Our previous study [4.14] found a large discrepancy in the estimated impact energy per area between fully elastic and elastic-plastic constitutive models in polymers. This indicates that the yield strength σ_y plays an important role in determining cavitation damage. In this study, by using a detailed analysis of pit formation on polymers, a nonlinear relationship with a high correlation ($R^2 > 0.9$) between cavitation pit volume and depth to σ_y was found. This finding correlates with the U-shaped relationship between the cavitation volume loss (CVL) and the Shore hardness of 27 polymers in the cavitation erosion test conducted by Barletta et al. [4.17].

Shore hardness is a typical parameter that represents the hardness in polymers, similar to Vickers hardness in metals. The main differences are the indenter shape and measurement settings. The relationship between several types of hardness is defined in the hardness conversion table provided in ASTM. An early study by Cahoon et al. [4.18] established an empirical relationship between Vickers hardness, which is approximately three times that of σ_y. From this, it can be deduced that the high correlation of cavitation pit volume and depth with σ_y also represents a high correlation with the Shore hardness in polymers.

The damage mechanism behind the left-side portion of the U-shaped relationship between CVL and Shore hardness from [4.17] (lower hardness and σ_y) can be explained from the results obtained in this study. Evidence from real-time video of cavitation erosion test of epoxy resin conducted by Hibi et al. [4.19] shows several micro-holes (pits) and micro-cracks that interconnected with each other which then initiates a larger crack. The initiation of holes relates to cavitation pit volume that is observed in this study. The larger the size of initial holes, the more severe the erosion that can occur in the material. Therefore, it can be deduced that cavitation damage for polymers with relatively low hardness and σ_y values is considered to occur mainly because of yielding or low-cycle fatigue from several repeated loads of bubble cloud collapse. However, further analysis with damage parameters incorporated into the constitutive models is needed for confirmation in this regard.

The damage mechanism behind the right-side portion of the U-shaped relationship between CVL and Shore hardness from [4.17] (higher hardness and σ_y) cannot be explained owing to limitations in the material properties of the polymers used in this study. However, a deduction can be made as follows: high σ_y causes the jet emitted from bubble collapse to not reach the critical impact velocity of the materials; thus, the solid particle does not skid and no instant plastic deformation occurs. This resembles the cavitation damage mechanism of metals found in this study. A higher σ_y is typically correlated with a higher Young's modulus E, which results in a higher acoustic impedance. Hence, the impact load from bubble collapse at the

surface becomes stronger as the material becomes "harder." Our findings represent the first stage in which plastic deformation occurs during the incubation period. Therefore, the damage mechanism for polymers with relatively high σ_y or hardness is the same as that found in metals, which occurs because of repeated load and high-cycle fatigue.

4.3.9 Fatigue Estimation for Metals

From previous section, a deduction has been made that the right hand side of U-shaped graph from [4.17] represents high-cycle fatigue phenomena in metals. In this section, a simple estimation of fatigue life for metal cases only will be conducted. From the analysis of pit depth and radius in polymers carried out in Section 4.3.5, it is clear that the jet from bubble collapse dominates within 0° or in the x axis. Similar behavior is expected to occurred in metals. Therefore, it can be assumed that the loading from bubble collapse behaves as uni-axial.

In uniaxial loading, fatigue analysis is commonly viewed from principal stress. In this case, it is σ_{11}. The most severe σ_{11} location for all cases occurred at the center, which is $y = 0$ mm. Figure 4.19 shows an example of plotted principal stress σ_{11} for Titanium 5 mm case. The maximum stress σ_{max} and minimum stress σ_{min} were then selected to calculate the mean stress σ_m and stress amplitude σ_a by using this formula:

$$\sigma_a = \frac{\sigma_{max} - \sigma_{min}}{2} \tag{4.8}$$

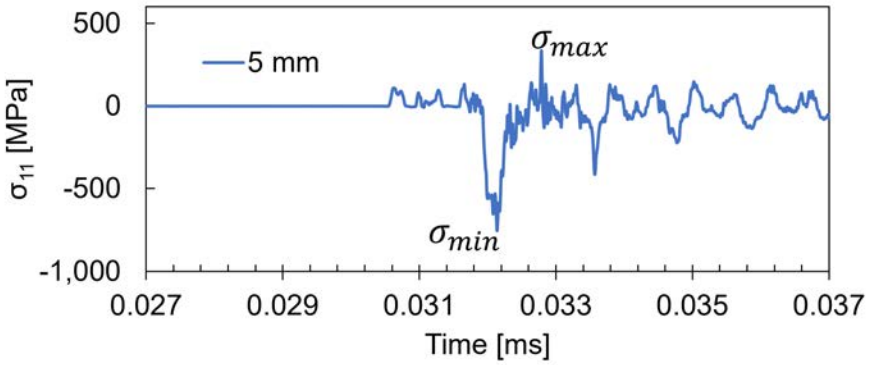

Figure 4.19: Principal stress σ_{11} in x direction at the center ($y = 0$ mm)for Titanium 5 mm.

The data of maximum and minimum stress for each metals cases were used to determine another fatigue parameters such as stress range ($\Delta\sigma = \sigma_{max} - \sigma_{min}$) and its ratio. The results is described in Table 4.4.

Table 4.4: Fatigue parameters from all metals cases. Stresses are in MPa units.

Material	h [mm]	σ_m	σ_a	$\Delta\sigma$	$\frac{\sigma_m}{\sigma_a}$	$\frac{\sigma_{min}}{\sigma_{max}}$
Ti	5	210.45	543.17	1086.33	2.58	-2.27
	3	146.72	467.90	935.81	3.19	-1.91
	1	52.65	521.43	1042.86	9.9	-1.22
	0.5	126.19	518.17	1036.34	4.11	-1.64
SUS304	5	258.97	563.62	1127.25	2.18	-2.7
	3	310.52	452.48	904.97	1.46	-5.37
	1	244.53	487.12	974.24	1.99	-3.02
	0.5	302.7	566.36	1132.72	1.87	-3.3
Al2024	5	203.35	385.06	770.12	1.89	-3.24
	3	267.98	393.27	786.53	1.47	-5.28
	1	275.48	477.53	955.06	1.73	-3.73
	0.5	244.31	451.85	903.7	1.85	-3.35
Mg	5	252.81	347.4	694.81	1.37	-6.35
	3	211.23	357.81	715.62	1.69	-3.88
	1	242.37	429.67	859.34	1.77	-3.59
	0.5	261.68	382.6	765.2	1.46	-5.33

An effort to combining the phenomena of yielding in polymers and high-cycle fatigue in metals was done. Arbitrary points of Cavitation Volume Loss (CVL) from U-shaped graph of [4.17] was extracted and then mapped with stress range $\Delta\sigma$ for metals (triangle-grey). The results is seemingly similar. Non-linear relationship between stress range and CVL appears in metals case. This strengthen our findings that cavitation damage in metals occurred due to high-cycle fatigue. However, further analysis including real cavitation volume loss of metals should be conducted to better represent the phenomena.

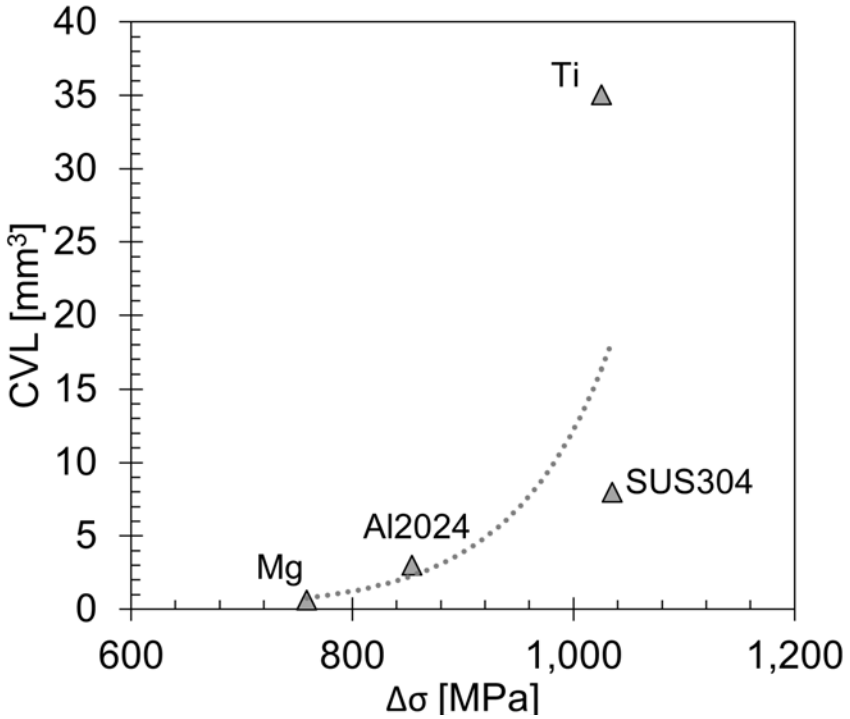

Figure 4.20: Approach to estimate similar graph as [4.17].

One of the conservative way to estimate fatigue life is by evaluating the mean stress and its amplitude through Goodman diagram. The connection between ultimate strength σ_{ut} and endurance limit S_e is called Goodman line. The endurance limit was obtained by using the assumption that it is half of the ultimate strength σ_{ut}. The area below this line represents infinite life, means that the solid material will endures the load without fail. The area above this line represents finite life. Yield line is introduced inside the diagram to give a representation of where the yielding might happened. The Goodman diagram for each metals are shown in Figure 4.21.

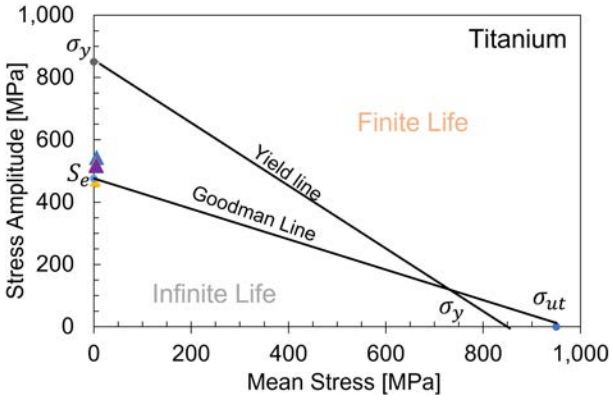

(a)

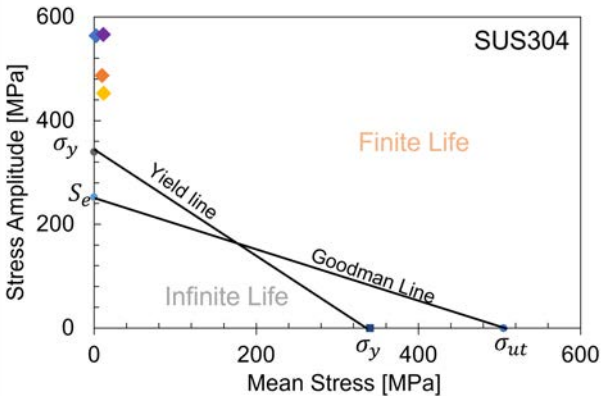

(b)

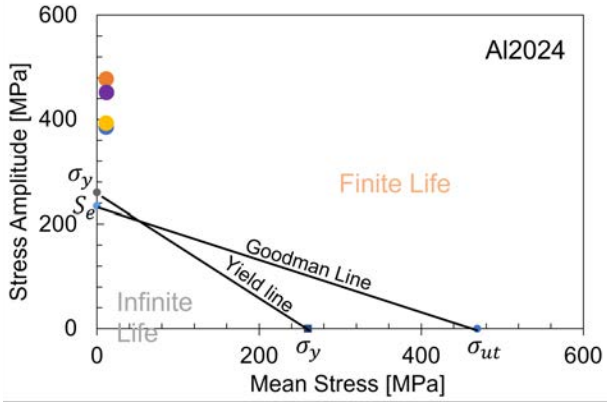

(c)

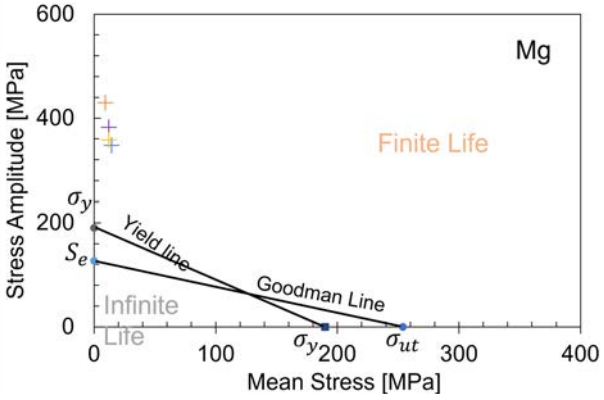

(d)

Figure 4.21: Goodman diagram for (a) Titanium, (b) SUS304, (c) Al2024, and (d) Magnesium.

From the analysis above, it is shown that there are no stress ration occurred below the Goodman line. This indicates the bubble collapse loading has finite life effect to the metals. For Titanium, the stresses lies just above the Goodman line and below Yield line, indicating that it has the highest cycle amongst all of the other cases.

4.4 Summary

In this chapter, a similar numerical model of air bubble placed inside long and narrow water-filled channel as in Chapter 3 was conducted. Only the edge boundary of solid material in the x direction was freed to represent multiple collapse in bubble clouds situation. Only elasto-plastic was analyzed in this chapter. The solid thicknesses of the metals were 5 mm, 3 mm, 1 mm and 0.5 mm while those of the polymers were 5 mm, 3 mm and 1 mm. Other than maximum BCIL analysis to acoustic impedance z, wave propagation behavior of BCIL inside solid material and plastic deformation behaviors of polymers were conducted.

Bubble deformation behavior were analyzed for all metal and polymer cases. The upward and downward bubble surface edge were tracked using image analysis in MATLAB for all metals and polymers cases. It was observed that there was negligible variation in the upward and downward movement of the bubble boundary leading to collapse. This indicates that the influence of fluid domain input is not affected by the differences in material properties and thickness.

The relationship between maximum BCIL and acoustic impedance z was plotted for all cases. The results showed that for metals, there was a direct proportionality between maximum BCIL and acoustic impedance. However, for polymers, there was little to no correlation found between maximum BCIL and acoustic impedance. The value of maximum BCIL for metals were also affected by the variation of thickness, indicating that the impacts transmitted inside the metals holds an important role. There was a significant increase of maximum BCIL value for metals with the thinnest thickness, 0.5 mm.

Wave propagation analysis through Continuous Wavelet Transform of BCIL acting on the solid surface revealed that for metals, the impact is primarily transmitted as compression and shear elastic wave. Hence, cavitation damage of metals can be defined by BCIL and acoustic impedance. Moreover, the wavelet transform results indicates that the reason for significant increase of maximum BCIL value on 0.5 mm thickness is because there was a superposition of counterjet duration of visibility and elastic wave frequency. Therefore, thickness selection of 0.5 mm in metals should be generally avoided. On the other hand, no significant correlation is found between polymers and elastic wave.

The BCIL on polymers generates an excessive plastic deformation known as pit. An image analysis of cavitation pit growth in polymers revealed a strong correlation between pit volume and depth to the yield strength of polymers. The relationship is found to be nonlinear. Furthermore, the connection between nonlinear relationship of cavitation pit to yield strength found in this study and U-shaped relationship of cavitation volume loss to Shore hardness by Barletta et al. [4.17] were discussed. It was confirmed that the damage of polymers with relatively low hardness is caused by yielding and low-cycle fatigue. For polymers with high hardness, the damage mechanism can be deduced as follows: the high level of hardness provides greater resistance to yielding, resulting in the impact being primarily transmitted as elastic waves. As a result, the damage is caused by high-cycle fatigue from repeated loads of bubble collapse, which is analogous to the behavior observed in metals.

References

[4.1] Y. Wang, X. Zeng, H. Chen, X. Yang, F. Wang, J. Ding, Hugoniot states and mie–grüneisen equation of state of iron estimated using molecular dynamics, Crystals 11 (2021). doi:10.3390/cryst11060664.

[4.2] A. Shima, Y. Tomita, D. C. Gibson, J. R. Blake, The Growth and Collapse of Cavitation Bubbles Near Composite Surfaces, Journal of Fluid Mechanics 203 (1989) 199–214. doi:10.1017/S0022112089001436.

[4.3] A. Philipp, W. Lauterborn, Cavitation erosion by single laser-produced bubbles, Journal of Fluid Mechanics (1998). doi:10.1017/S0022112098008738.

[4.4] S. Hattori, T. Itoh, Cavitation erosion resistance of plastics, Wear 271 (2011) 1103–1108. doi:10.1016/j.wear.2011.05.012.

[4.5] M. A. Meyers, Dynamic Behavior of Materials, Dynamic Behavior of Materials (1994). URL: https://onlinelibrary.wiley.com/doi/book/10.1002/9780470172278. doi:10.1002/9780470172278.

[4.6] S. Cao, G. Wang, O. Coutier-Delgosha, K. Wang, Shock-induced bubble collapse near solid materials: Effect of acoustic impedance, Journal of Fluid Mechanics 907 (2020). doi:10.1017/jfm.2020.810.

[4.7] S. Joshi, J. P. Franc, G. Ghigliotti, M. Fivel, SPH modelling of a cavitation bubble collapse near an elasto-visco-plastic material, Journal of the Mechanics and Physics of Solids 125 (2019) 420–439. doi:10.1016/j.jmps.2018.12.016.

[4.8] C. K. Turangan, G. J. Ball, A. R. Jamaluddin, T. G. Leighton, Numerical studies of cavitation erosion on an elastic–plastic material caused by shock-induced bubble collapse, Proceedings of the Royal Society A: Mathematical, Physical and Engineering Sciences 473 (2017) 20170315. doi:10.1098/rspa.2017.0315.

[4.9] C. T. Hsiao, A. Jayaprakash, A. Kapahi, J. K. Choi, G. L. Chahine, Modelling of material pitting from cavitation bubble collapse, Journal of Fluid Mechanics 755 (2014) 142–175. doi:10.1017/jfm.2014.394.

[4.10] C.-D. Ohl, T. Kurz, R. Geisler, O. Lindau, W. Lauterborn, Bubble Dynamics , Shock Waves and Sonoluminescence, Philosophical Transactions : Mathematical , Physical and Engineering Sciences , Vol . 357 , Pub 357 (2009) 269–294.

[4.11] O. Lindau, W. Lauterborn, Cinematographic observation of the collapse and rebound of a laser-produced cavitation bubble near a wall, Journal of Fluid Mechanics 479 (2003) 327–348. doi:10.1017/S0022112002003695.

[4.12] R. Timm, Optical and acoustic investigations of the dynamics of laser-produced cavitation bubbles near a solid boundary, Journal of Fluid Mechanics 206 (1989) 299–338. doi:10.1017/S0022112089002314.

[4.13] M. Misiti, Wavelet Toolbox ™ Reference How to Contact MathWorks (2015) 209.

[4.14] R. Firly, K. Inaba, F. Triawan, K. Kishimoto, K. Hayabusa, H. Nakamoto, Numerical prediction of cavitation damage based on shock-induced single bubble collapse near solid surfaces, European Journal of Mechanics - B/Fluids 98 (2023) 143–160. doi:10.1016/J.EUROMECHFLU.2022.12.002.

[4.15] A. Yabuki, K. Matsuwaki, M. Matsumura, Critical impact velocity in the solid particles impact erosion of metallic materials, Wear 233-235 (1999) 468–475. doi:10.1016/S0043-1648(99)00170-2.

[4.16] F. G. Hammitt, Cavitation Erosion: the State of the Art and Predicting Capability., 1979.

[4.17] A. D. o. M. Barletta, M. Science), A. D. o. M. Ball, M. Science), Cavitation Erosion of Polymeric Materials, 1983.

[4.18] J. R. Cahoon, W. H. Broughton, A. R. Kutzak, The determination of yield strength from hardness measurements, Metallurgical Transactions 2 (1971) 1979–1983. doi:10.1007/BF02913433.

[4.19] M. Hibi, F. Triawan, K. Inaba, K. Takahashi, K. Kishimoto, K. Hayabusa, H. Nakamoto, Cavitation damage of epoxy resin subjected to uniaxial tensile loading, Mechanical Engineering Journal 5 (2018) 17–00151–17–00151. doi:10.1299/mej.17-00151.

Chapter 5

Conclusion and Future Works

5.1 Summary of Thesis

This dissertation concentrates on analyzing the relationship between damage from cavitation bubble collapse and solid material properties through a coupled fluid-solid numerical simulation. From fluid perspective, bubble collapse impact load (BCIL) and impact energy are used to quantify the intensity of damage. From solid perspective, acoustic impedance and plasticity are used to explain the cavitation damage mechanism on metals and polymers which are commonly used as main material and coatings for hydromachinery components. The brief summaries of each chapter are:

In chapter 2, we examined the numerical scheme of ANSYS Autodyn to decide which parameters that affect the dynamics of bubble collapse and its impact to solid material. Grid verification was conducted. It was found that 34 nodes per 0.5 mm bubble radius gives a stable result. Validation against two cases: laser-induced bubble inside gelatin gel and shock-induced bubble collapse near Lucite wall were done. The shock-front and vapor bubble radius inside 10%wt gelatin from present simulations were shown to be in good agreement with experimental and numerical results of Oguri and Ando (2018). The averaged impact pressure at Lucite wall also shows good agreement with experiment results by Shima et al. (1989) and numerical results by Johnsen and Colonius (2008).

In chapter 3, we developed a numerical model of shock-induced collapse of air bubbles near metals (titanium, SUS304, Al2024) and polymers (adiprene, epoxy, and polyethylene) with standoff distance 1.06 inside long and narrow channels with width 1 mm. Three different material constitutive models–purely elastic, elastic-perfectly plastic, and strain-hardening–were investigated. The elastic-perfectly plastic model gives highly comparable results of maximum BCIL against acoustic impedance compared with cavitation erosion test of several metals and polymers of Hattori and Itoh

(2011). The impact energy analysis for metals shows no significant change between three constitutive models. However, for polymers, large discrepancies were found in the elastic model. This indicates two things: in metals, BCIL can be defined by acoustic impedance, whereas in polymers, it is heavily affected by yielding. However, further evidence is needed to explain this damage mechanism.

In chapter 4, we continued to utilize the same numerical model, with thickness varied from 5 to 0.5 mm and only elastic-perfectly plastic model was analyzed. Magnesium, Teflon, and nylon were added to the material for filling the acoustic impedance data in the middle range. Maximum BCIL acting on the solid surface was plotted against acoustic impedance. It was found that for metals, BCIL decrease as the impedance decreases. There is a significant increase in maximum BCIL value for 0.5 mm thickness, indicating that it is affected by wave propagation behavior inside material. For confirming the mechanism, Continuous Wavelet Transform analysis was conducted for BCIL acting on the surface. It was confirmed that for metals, BCIL propagates with similar frequency as the elastic wave (compression and shear). The significant increase occurred due to superposition between elastic wave frequency and the counterjet duration of visibility. Hence, it can be concluded that the damage mechanism of metals can be explained by BCIL and acoustic impedance.

For polymers, no inference has been found to elastic properties. Therefore, plastic deformation behavior was analyzed in detail. Image analysis of apparent pit growth was computed through MATLAB. The pit volume growth rate shows high correlation ($R^2 \geq 0.9$) of non-linear relationship with yield strength, meaning that the initial plastic deformation phase depends on yield. To visualize the incubation-like period in the plastic deformation, the averaged final pit depth and pit volume were estimated. High correlation ($R^2 \geq 0.9$) with non-linear relationship with yield strength was also found.

5.2 Conclusions

This study has developed a coupled fluid–solid numerical model of shock-induced air bubbles collapse near metals and polymers with standoff distance $\gamma = 1.06$ inside long and narrow channels with width $\bar{w} = 1\,\text{mm}$ that can represent multiple bubbles collapse in cavitation experiments. The impact phenomena analysis of this numerical model reveals distinct cavitation damage mechanism between metals and polymers. By understanding that in polymers, it indicates yielding whereas in metals, elastic properties thus high-cycle fatigue is more prominent, engineers can make wiser decisions during the material selection process for coatings and main components in hydro machinery, which are:

1. From the analysis of pit volume and yield strength in polymers, it is found that polymers with yield more than 60 MPa potentially gives less damage.

2. The coating thickness variation of 5, 3, and 1 mm gives small inference to pit volume. Hence, the application of 1 mm coatings is deemed to be enough.

3. From the wave propagation analysis in metals, there is an increase of maximum impact load value for 0.5 mm due to the superposition of elastic waves. Therefore, for metals coatings, thinner thickness application should be avoided.

5.3 Future Works

As explained in Chapter 3, a good agreement against maximum BCIL value in the cavitation erosion test of metals and polymers has been achieved with a shock-induced air bubble collapse inside long and narrow channel numerical model developed in this study. It clarifies that the side rigid wall in the narrow channel represents reflection waves from nearby bubbles in the bubble clouds collapse situation. However, it is still not clear exactly how much surrounding bubbles this model represents. Therefore, an axial symmetric 3D simulation with degree of revolution θ as parameters should be conducted to further validate this model. The θ can represent how much surrounding bubbles exists, with 360 deg as the maximum amount which is infinite bubbles. By quantitatively analyzing and comparing the maximum BCIL from both 2D and 3D simulations, the amount of surrounding bubbles can be validated.

From the perspective of cavitation erosion prevention, another idea is proposed to be analyzed through numerical simulations. The general results of cavitation erosion tests show that the Mean Depth Penetration Rate (MDPR) will decrease after long hours. Following deduction can be made: because the flat solid surface has been damaged, thus instead of collapsing, the cavitation bubbles now attach to

the damaged surface. This gives an impression that solid surfaces with rough or wavy profiles can give a cushioning effect. Therefore, a numerical analysis of wavy profiles with certain function parameter can be conducted to prove this hypothesis.